A Fast NIR Spectrometer for Examining Explosive Events: Emission of PETN Based Explosives and H_2O Absorption Method Feasibility

Scott Piecuch
Marquette University

A FAST NIR SPECTROMETER FOR EXAMINING EXPLOSIVE EVENTS: EMISSION OF PETN BASED EXPLOSIVES AND H_2O ABSORPTION METHOD FEASIBILITY

by

Scott R. Piecuch, B.S.M.E.

A Thesis submitted to the Faculty of the Graduate School,
Marquette University,
in Partial Fulfillment of the Requirements for
the Degree of Master of Science in Mechanical Engineering

Milwaukee, Wisconsin

December 2009

ABSTRACT
A FAST NIR SPECTROMETER FOR EXAMINING EXPLOSIVE EVENTS:
EMISSION OF PETN BASED EXPLOSIVES AND H_2O
ABSORPTION METHOD FEASIBILITY

Scott R. Piecuch, B.S.M.E.

Marquette University, 2009

The chemical dynamics and decomposition pathways of explosive materials are not entirely known. Measurements of chemical transients during explosive events can lead to enhanced knowledge of the detailed chemistry and eventually control of the end products; however, these measurements are often difficult to obtain due to fast time scales and harsh environments. Optical diagnostics present fast-response, minimally invasive methods for resolving properties in detonation environments and previous fast spectroscopic measurements have been recorded in the ultra-violet and visible regions. This work extends the range of such measurements to the near-infrared (NIR) through the development of a fiber-coupled NIR spectrometer utilizing a fast InGaAs array. The characteristics and applications of this spectrometer are investigated through temporally and spectrally resolved measurements during the detonation and post-detonation combustion in arena-type explosives experiments.

The spectrometer was used to examine the emission features and temperatures of atomic and molecular species with microsecond time resolution from pure pentaerythritol tetranitrate (PETN) charges and PETN charges doped with 10% (by mass) Ag and Al microparticles. The post-detonation spectra were observed between 750 nm and 1500 nm at rates up to 46k-spectra/sec, and key features were identified. Emission spectra from the particle doped charges followed a Planckian distribution at later times (>40μs) and spectral pyrometry temperature measurements were determined from the spectra.

The NIR spectrometer can also be used to acquire absorption spectra which can allow for the measurement of bulk gas temperature and direct species concentrations as well as provide more control over the probed volume. An investigation was conducted on the feasibility of using the newly developed NIR spectrometer in explosives experiments to measure water absorption in the 1330-1380 nm region and determine temperatures and concentrations of H_2O using a fiber coupled broad light source. The fiber size, resolution, and path-length necessary for accurate temperature mol fraction H_2O measurements were determined.

ACKNOWLEDGEMENTS

Scott R. Piecuch, B.S.M.E

I would like to thank my advisor Dr. Jon Koch for the guidance and opportunities that he has given me during my graduate studies at Marquette. His advice, enthusiasm, and insight have helped me develop my work into this thesis. I would also like to thank Dr. Joel Carney for giving me the opportunity to work at the Naval Surface Warfare Center as well as Dr. Jim Lightstone and Dr. Jon Borg for serving as my committee members. I thank my colleagues Dan Sherwin, and Liam O'Callaghan for supporting my work towards this thesis, as well as my friends in Marquette's theatre department for their camaraderie and support.

I am grateful to my parents who have always encouraged me and to whom I owe my intelligence and work ethic. Finally, I would like to thank Nicole for her enduring support and patience.

TABLE OF CONTENTS

LIST OF TABLES

LIST OF FIGURES

Chapter 1: Introduction

Motivation and Objectives

Recently, the Defense Threat Reduction Agency (DTRA) has become interested in developing more effective high explosives for use in neutralizing chemical and biological warfare agents. It is known that holding chemical and biological agents at high temperatures can neutralize such agents, and the effectiveness of common high explosives in agent defeat is thought to be limited mainly to the brief incineration effects of the fireball. It has also been shown that adding aluminum micro-particles to high explosive formulations can greatly increase the amount of energy released in the post-detonation combustion and prolong the burning of the fireball, potentially increasing its capacity for agent defeat (Goroshin, L. Frost et al. 2006).

Another method for agent defeat is chemical sterilization using bleach-based compounds, halogen gases, strong acids, or strong bases; however, these compounds produce hazardous byproducts that are caustic and/or toxic in nature (Russell 1990; Levi 2004). A less toxic material for use in agent defeat is sought, and recent research

suggests that nanoparticles of silver metal and silver halide compounds are excellent candidates. Silver nanoparticles exhibit broad antimicrobial activity at low concentrations while retaining low toxicity toward mammals (Rentz 2003; Morones, Elechiguerra et al. 2005; Sambhy, MacBride et al. 2006). Research is being done at the Naval Surface Warfare Center, Indian Head Division on tailoring high explosive formulations for agent defeat with the desired attributes and motivations that are summarized in Table 1.1.

Desired Attribute	Motivation
• Persistent high-temperature	• Facilitate thermal deactivation of agent • Enhance biocidal activity of anti-microbial additive
• Inclusion of anti-microbial compounds that are minimally toxic to mammals	• Facilitate chemical deactivation of agent
• Low peak pressure	• Limit dispersion of active agent

Table 1.1. Desired attributes of high explosive formulations for use in agent defeat and their motivations.

In order to create effective formulations with the attributes listed in Table 1.1, it is necessary to study the chemical dynamics and decomposition pathways of such explosive materials; however, such mechanisms are not entirely known for any high explosives. This is partly because measurements of chemical transients during explosive events are often difficult to obtain due to short time scales and harsh environments (Cooper 1996; Carney, Miller et al. 2006; Petersen, Arvanetes et al. 2007; Lewis and Rumchik 2009). The detonation velocity of most common explosives is typically several kilometers per second causing the detonation wave to travel entirely through gram-scale explosives in several microseconds. Subsequently, the energy released in the after-burn of under-

oxidized detonation products can exceed the heat released in the detonation itself, producing a fireball that remains for several milliseconds (Cooper 1996). The short timescales of these events limit the diagnostics that can be implemented and the measurements that can be made. Further, the high pressures and temperatures created during explosive events also present significant measurement challenges as the diagnostics must survive long enough to record relevant data.

Optical techniques are attractive tools for use in explosive environments as they can be fast-response, minimally invasive methods for temporally resolving properties. Atomic and molecular emission spectroscopies are particularly well suited for detonation and post-detonation studies due to their capacity for large standoff distances and fast operation. By remotely monitoring emission from the combustion products, greater insight into the behavior of the chemical processes can be achieved (Carney, Wilkinson et al. 2007; Petersen, Arvanetes et al. 2007; Lewis and Rumchik 2009). Such emission spectroscopy has been successfully implemented in combustion applications, laser ablation events, strand burner combustion, shock tubes, and arena type experiments (Glumac, Krier et al. 2005; Bazyn, Krier et al. 2006; Bazyn, Glumac et al. 2007; Lightstone, Carney et al. 2007; Petersen, Arvanetes et al. 2007).

Emission spectroscopy can give temporally resolved information on the presence of chemical transients, their relative populations, as well as the temperature of the emitting species. Fast, time-resolved measurements from emission spectroscopy have been successfully obtained in large and small scale arena type explosives experiments in the ultra-violet and visible regions using streak cameras with very good temporal resolution (500 ns) by Caney, *et al.* Extending the spectral range, near-infrared emission

spectroscopy has also been effectively used in field tests involving large amounts of high explosives (tens of kg or more) by Orson and Gross; however, the temporal resolution in their experiments was low (on the order of tens of milliseconds) (Gross, Dills et al. 2003; Orson, Bagby et al. 2003). This temporal resolution is insufficient to capture the evolution of the structured atomic and molecular features present during the quick detonation event and was limited to capturing broad infrared emission from incandescent particles during the afterburn process.

New developments in high-speed InGaAs arrays have opened a new possibility for spectroscopic tools. Utilizing a fast InGaAs array, capable of acquiring up to 47,348 spectra per second, it is possible to couple the array with a spectrometer and obtain temporally resolved emission spectra in the near-infrared at much faster rates than previously possible. The work in this thesis will demonstrate the development of such a device and its application to detonation science.

Emission spectroscopy is an excellent diagnostic for explosives experiments; however, it is not without limitations. While emission spectroscopy can give relative information regarding the excited state populations of chemical species, it cannot yield direct concentrations of the species, which are of great importance in the study of the chemical kinetics. Further, when observing emission from optically thick detonation products, there is the possibility of self-absorption and the diagnostic is limited to probing the outer perimeter of the expanding combustion front. If the optical thickness of the cloud is not known, it is difficult to determine how far into the combustion front the diagnostic is probing and interpretation of the results can be problematic. Another optical method that avoids some of these limitations is absorption spectroscopy. This method

can allow for measurement of bulk gas temperature and direct species concentration measurements as well as more control over the probed volume. Absorption spectroscopy has been successfully employed in a range of harsh environments including shock tubes, internal combustion engines, and gas turbine engines (Glumac, Krier et al. 2005; Hagen and Sanders 2007; Kranendonk, Caswell et al. 2009). Recently, Carney et al. have effectively implemented short-path length absorption spectroscopy in an arena type experiment, observing aluminum absorption lines in the ultra-violet region (Carney, Wilkinson et al. 2007).

Of potential interest to detonation studies is water absorption spectroscopy. Water is a naturally occurring product of both detonation reactions and the subsequent post-detonation combustion. By monitoring water absorption lines, it is possible to obtain temporally resolved measurements of temperature, pressure, and concentration of water in the probed volume over a wide range of temperatures and pressures. Such water absorption techniques have been successfully implemented in comparable harsh environments such as shock tubes, pulse-detonation engines, and internal combustion engines (Arroyo, Langlois et al. 1994; Sanders, Mattison et al. 2002; Hagen and Sanders 2007; Kranendonk, An et al. 2007). This technique is particularly appealing as it does not require doping of the explosives, which may interfere with the combustion chemistry, has been shown to be robust (Kranendonk, Caswell et al. 2007), and can measure a wide range of properties extremely rapidly. Absorption spectroscopy can provide more information about specific species and allows for more control over the information obtained; however, there are several significant challenges to its implementation in explosive environments which will be discussed in the following section.

In this work, a novel near-infrared spectrometer is developed for use in arena-type explosives experiments. In order to maximize its effectiveness the design of the spectrometer allows for both emission and absorption experiments to be performed, increasing its applicability to detonation science and increasing the amount and types of information it can provide.

The objective of the work reported here is twofold:

1. Develop and apply a fast near-infrared spectrometer for measurement of spectral emission features and temperatures of atomic and molecular species with microsecond time resolution in an arena type high explosives experiment.
2. Investigate the feasibility of using the newly developed near-infrared spectrometer for measuring water absorption in the NIR region to determine temperatures and concentrations of water using a fiber coupled broad light source.

Each objective presents a set of challenges which must be overcome to validate this device's benefit to detonation science. Arena type emission and absorption experiments were performed in a blast-proof chamber at the Naval Surface Warfare Center, Indian Head Division in Indian Head, MD. Further water absorption feasibility studies were performed at Marquette University in Milwaukee, WI. The challenges and solutions for each objective are presented below and will be discussed in greater detail in the following chapters.

Measurement Challenges

While emission and absorption spectroscopy present some challenges common to all optical diagnostics, these challenges are intensified in a harsh explosive environment. In arena-type explosives experiments, the detonation is confined to a small room in which the atmosphere can be controlled. The extreme temperatures and pressure created following the detonation of high explosives are confined to the blast chamber and present some particularly difficult sensing challenges as summarized in Table 1.2.

Sensing Challenges	Potential Solutions
• Strong shockwave created • High temperatures (up to 5000K)	• Inexpensive, expendable collection lenses • Remote collection far from detonation site • Fiber-optic based sensor system to allow for sensitive equipment to be kept in adjacent shielded room
• Difficult timing	• Fast LabView controlled FPGA module for controlling camera timing • Trigger supplied to DAQ system by charge firing circuitry
• Optical resolution required for observation of discrete atomic lines	• Interchangeable dispersion gratings • Adjustable entrance slit to spectrometer to optimize signal levels and resolution
• Highly transient event	• Adjustable integration times on fast InGaAs camera
• Large intensity range	• Adjustable sensitivity of camera tuned to capture breakout and subsequent broad emission • Large fiber to collect weak emission • Large, fast collection optics
• Electro-magnetic pulse	• Electrically shield sensitive equipment in adjacent room

Table 1.2. Sensing challenges and potential solutions for emission spectroscopy in arena-type explosives experiments at NSWC, IH.

Both emission and absorption spectroscopies share many of the challenges in Table 1.2 and are mainly a result of the shockwave created from detonation. While the major challenges associated with the violent detonation event were managed in these arena-type emission spectroscopy experiments, absorption spectroscopy presents several

more difficult challenges due to the necessity of pitching and catching light all within the blast chamber. A summary of additional sensing challenges related to absorption spectroscopy and potential solutions is presented in Table 1.3.

Sensing Challenges	Potential Solutions
• Large temperature range to be measured (300-5000K) • Large pressure range to be measured (1-15 atm)	• NIR, broad SOA light source to measure water absorption features near 1.35μm • Accurate spectroscopic database • Robust method for accurately determining T,X_{H2O},P from simulated spectra
• Difficult light source/camera timing	• Fast LabView controlled FPGA module for controlling light source/camera timing • Trigger supplied to DAQ system by charge firing circuitry
• Temporal fluctuations in reference signal	• 90/10 split of reference allows 1:1 spectral correction for each light pulse
• Vibrations in pitch/catch gauge	• Optical setup of collection optics optimized to allow displacement of beam • Rigid steel gauge to hold fibers
• Long required path length (8 cm)	• Adjustable path length to optimize SNR
• Beam steering	• Collection fiber de-tuned from focal length of collection lens to allow for movement of beam
• Optical opacity of detonation products	• High Explosive PETN is known to be very optically thin • Direct fiber coupled NIR light source reduces coupling losses maximizing initial intensity • Fiber reflector coupled to source to increase light intensity

Table 1.3. Additional sensing challenges and potential solutions for absorption spectroscopy in arena-type explosives experiments at NSWC, IH.

Previous Work

Emission spectroscopy is a powerful optical technique that has been used in a wide variety of combustion studies; however, only a small number of studies have been

conducted that involve time-resolved measurements in detonation experiments. Even less work has been performed involving absorption spectroscopy in detonation environments due to the harsh conditions created in explosive environment. Below is a summary of previous work conducted in the related areas.

Time Resolved Emission Spectroscopy in Harsh Environments

Time-resolved emission spectroscopy has proven valuable for studying harsh combustion systems. Horn and Gupta developed a method for temporally resolving the wavelength shift of ruby luminescence R lines under shock loading (Horn and Gupta 1986). The results of their experiments demonstrated the ability to make temporally and spectrally resolved measurements in harsh environments using a fiber-coupled spectrometer and streak camera. Pangilinan and Gupta utilized a similar system examining Raman scattering in shocked carbon tetrachloride to determine temperatures, demonstrating high-speed (50 ns temporal resolution) property measurements in harsh environments (Pangilinan and Gupta 1997). Miller and Pangilinan adapted such time-resolved spectroscopy techniques for examining aluminum combustion in the extreme environment of arena-type detonation experiments (Miller and Pangilinan 2004). This study examined aluminized energetic formulations with high temporal resolution (~1.6 μs) in the visible region (350-550nm). Aluminum and aluminum oxide lines were identified and their temporal profiles were examined to determine the participation of the aluminum in the detonation and post-detonation combustion.

Further optical measurements in arena type detonation experiments have been carried out by Carney *et al.* at the Naval Surface Warfare Center in Indian Head, MD

(Carney, Miller et al. 2006; Carney, Wilkinson et al. 2007). Temporal, spatial and spectral specificity of the light emission from the detonation of PBXN-113 charges was achieved using a combination of optical diagnostics including two UV-visible streak spectrometers (2.5 nm spectral and 500 ns temporal resolution), fast photodiodes, and a digital framing camera. In their observation of post-detonation Al, and AlO lines, Carney *et al.* found that in-line, collimated collection is the optimum geometry for such experiments because signal levels are independent of distance between the optics and explosive charge (Carney, Miller et al. 2006). Thus, the emission experiments performed in this work utilized in-line collimated collection to produce consistent results.

Wilkinson *et al.* also examined aluminum lines present in post-detonation combustion of PBXN-113 in the UV-visible region using a fast streak spectrometer. With a temporal resolution of 2 μs and a spectral resolution of 0.6 nm, Wilkinson *et al.* were able to determine atomic aluminum temperatures of ~4000 K from the relative strengths of observed aluminum emission lines. Optical pyrometry temperature measurements were simultaneously acquired and found initial temperatures of ~2700 K cooling to ~2000 K at later times (Wilkinson, Lightstone et al. 2007). This discrepancy is thought to be from inaccuracy in atomic temperature measurements from spectral broadening by optical depth (Peuker, Lynch et al. 2009). Another method for measuring temperatures in arena type explosives experiments involves doping the explosives with strong thermometric impurities. Lewis and Rumchik obtained temporally resolved temperature measurements from emission spectroscopy of barium nitrate doped RDX in the visible region (450-800) nm with 1 nm spectral and 5 ms temporal resolution (Lewis and Rumchik 2009). It has been demonstrated that emission spectroscopy is a useful tool

for examining detonations and post-detonation combustion. High temporal and spectral resolution has been achieved in the aforementioned studies chiefly through the use of high resolution streak cameras; however, such cameras are not sensitive beyond the visible region (>750 nm) forcing alternate sensing methods to be employed in the near-infrared.

NIR Emission spectroscopy in Detonation Environments

In their work to remotely identify explosives via combustion emission signatures, Orson *et al.* examined infrared signatures from 56 events including aircraft delivered ordnance and ground detonations of a variety of bomb sizes and explosive formulations (Orson, Bagby et al. 2003). In their work, Orson *et al.* used a Fourier-transform interferometer coupled with a telescope to acquire time-resolved spectra in the mid-IR (1.6 μm-20 μm) with a spectral resolution of 4-16 cm^{-1} and temporal resolutions of 0.047-0.123 s. Orson *et al.* observed RDX and TNT based energetic materials and found that emission was well represented by a gray-body with continuously decreasing temperature with a characteristic decay time of 1-4 s. This successfully demonstrated the acquisition of time-resolved infrared spectra in field tests; however, the low temporal resolution of the experiments was unable to capture the highly transient emission during the detonation event and was limited to probing the slower after-burn process. From this work Gross *et al.* developed a phenomenological fireball model that allows for the remote identification of such high explosives (Gross, Dills et al. 2003; Gross, Perran et al. 2005; Gross, Wayman et al. 2007).

Optical Pyrometry in Detonation Environments

Optical pyrometry has been used in detonation experiments since the 1950's with the work of Gibson *et al.* and is still used to determine particle temperatures in harsh environments (Gibson, Bowser et al. 1958). As a fast-response, minimally invasive method for resolving temperatures, optical pyrometry has been used for measurements in numerous relevant combustion regimes including rocket plumes, shock tubes, and detonation experiments (Ogura, Okada et al. 2003; Glumac, Krier et al. 2005; Bazyn, Krier et al. 2006; Carney, Miller et al. 2006; Goroshin, L. Frost et al. 2006; Schmidt, Caswell et al. 2006; Bazyn, Glumac et al. 2007).

Goroshin *et al.* have recently utilized 2 separate 3-color pyrometers in the visible region to measure post-detonation combustion temperatures of kg scale TNT and nitromethane explosives in field tests (Goroshin, L. Frost et al. 2006). Early-time (within 100 μs of detonation) temperatures for homogenous TNT were found to reach 5000-6000 K (attributed to shock heated air), and the following fireball temperature was found to remain fairly constant (~2000 K) for more than 100 ms. Ogura *et al.* have performed similar field tests using 2 separate 4-color pyrometers in the 600-2000 nm region to examine kg scale TNT (Ogura, Okada et al. 2003). For similar conditions as reported by Goroshin *et al.*, shocked air temperatures of 8000-10000 K were recorded at early-times followed by a fairly constant fireball temperature of ~3500 K for hundreds of milliseconds.

These two studies show considerable variation of reported pyrometry temperatures for similar conditions suggesting that pyrometer setup has a large affect on measured temperatures. In addition, the work of Cezairliyan and Righini suggests that

the source of such discrepancies may be improper calibration and lack of knowledge of the emissivity function of the emitting material (Cezairliyan and Righini 1996). This work prompts investigation into alternate sensing strategies for temperature determination in post-detonation combustion of high explosives. The NIR spectrometer developed in this work provides alternate strategies for temperature measurements in such environments.

Absorption Spectroscopy in Harsh Environments

Absorption spectroscopy has been implemented in a variety of harsh environments including pulse detonation engines, internal combustion engines, and shock tubes (Arroyo, Langlois et al. 1994; Sanders, Mattison et al. 2002; Hagen and Sanders 2007; Kranendonk, An et al. 2007; Kranendonk, Huber et al. 2007) . Kranendonk *et al.* have developed a robust method for calculating temperature, pressure and absorber mole fraction from broadband absorption spectra that is particularly suited for such harsh environments as internal combustion engines, and potentially arena-type explosives experiments (Kranendonk, Caswell et al. 2007). In their method, a simulated database of H_2O absorption spectra is created for the relevant conditions from an accurate water line list such as the BT2 database (Barber, Tennyson et al. 2006). After a systematic scheme of smoothing, differentiation, and spectral axis warping is performed, the measured spectra are compared to the database using a linear least-squares fitting method to determine the properties of the measured spectra. The developed method requires H_2O vapor to be present, has been shown to be accurate in the relevant temperature region in harsh environments (300-3000 K), and is relatively insensitive to slight errors in

spectroscopic databases (Kranendonk, Huber et al. 2007). Since, H_2O vapor is a major product of detonation and combustion reactions, its use as the absorber molecule does not require additional doping of the energetic formulations used in this thesis. In their experiments Kranendonk, *et al.* utilized a Fourier-domain mode-locked laser to scan the R-branch of the $\nu_1+\nu_3$ band of H_2O (1330-1380 nm) and fast photodiodes to measure the absorption spectra at high rates (200 kHz) (Kranendonk, An et al. 2007; Kranendonk, Huber et al. 2007). To reduce complexity, cost, and extend the applicability of the newly created NIR spectrometer created in this work, a fast NIR broadband source was sought for the work presented in Chapter 4.

Previous research involving absorption spectroscopy in explosives experiments is limited. Carney *et al.* measured aluminum absorption lines in the visible region (390-400 nm) with some success using a spectrometer coupled with a streak camera (Carney, Wilkinson et al. 2007). In their experiments, Carney *et al.* successfully made measurements of aluminum concentration to aid in the modeling of fuel rich explosives; however, they found considerable variation from shot to shot. PETN was used as the base explosive material due to the optical clarity of the blast wave after detonation and aluminum micro-particles were added for their propensity to increase post-detonation combustion and strong known absorption lines in the visible region. The optical structure used to pitch and catch the light consisted of a commercially available lens tube assembly mounted to a rigid cage. Carney *et al.* found that this structure was suitable for small path lengths (6 mm); however, a greater signal-to-noise ratio can be achieved with larger path lengths that allow for more absorption. Thus, more rigid optical structures were investigated for the work in this thesis. The light source used in these experiments was a

fiber coupled tube filled with argon and high explosives that produced a broadband pulse of light ~100 ms in duration. Due to the complexity, hazards, and long turn-around time associated with this type of light source, alternate methods were sought and selected for the experiments detailed in Chapter 4.

Scope and New Contributions

The recent development of a novel, fast, InGaAs array has allowed for expansion of the regions in which temporally and spectrally resolved measurements are possible. This is of particular value to combustion and detonation sciences in which processes are characterized by very short timescales and has allowed for new developments to be made in arena-type explosives experiments. Key achievements and new contributions to this area that are presented in this thesis are summarized below.

Demonstration of High-Speed NIR Emission Spectroscopy for Use in Explosive Environments

High speed ultra-violet and visible spectroscopies have recently been used in arena-type explosive experiments for identification of atomic and molecular features from the intense emission at breakout, as well as atomic temperatures and the relative lifetimes that can be determined from such measurements (Carney, Miller et al. 2006; Carney, Wilkinson et al. 2007; Wilkinson, Lightstone et al. 2007; Lewis and Rumchik 2009). NIR emission spectroscopy has also been performed in large-scale field tests; however it utilized a Fourier-transform infrared spectrometer that had low temporal resolution 0.047-0.123s (Gross, Dills et al. 2003; Orson, Bagby et al. 2003; Gross, Perran et al. 2005; Gross, Wayman et al. 2007). This study extends such measurements in the

near-infrared by utilizing a newly developed NIR spectrometer capable of acquiring spectra at 47,348 kHz. Due to the higher temporal resolution, both the initial structured spectra from the detonation process and the broad emission that follows are able to be recorded with the new device. Chapter 3 summarizes the use of the new device in acquiring the following measurements: a baseline spectrum of PETN in the NIR, identification of spectroscopic features and their relative durations, and spectral pyrometry temperatures calculated from the spectra.

Feasibility Study of High-Speed NIR H_2O Absorption Measurements in Explosive Environments

Recent work in high-speed optical measurements has been performed using NIR H_2O absorption spectroscopy in combustion environments (Kranendonk, Huber et al. 2007). These measurements can yield high-speed and accurate temperature, pressure and H_2O concentration measurements; however, their use has been limited to more controlled combustion environments such as burners, shock tubes, and combustion engines (Arroyo, Langlois et al. 1994; Hagen and Sanders 2007; Kranendonk, An et al. 2007). Additionally, visible absorption spectroscopy measurements have been performed in arena-type explosive experiment observing aluminum absorption lines over a very short path length through the detonation products of aluminum doped PETN (Carney, Wilkinson et al. 2007). In order to apply the H_2O absorption method to arena-type experiments a longer path length is necessary which presents new challenges. The work presented in Chapter 4 summarizes a feasibility study of the application of high-speed NIR H_2O absorption spectroscopy for use in arena-type explosive experiments. The following contributions to this area are detailed: an investigation on the necessary path-

length for adequate signal to noise ratio, methods for reliable light collection over larger path lengths, and a study of the systems characteristics and limitations as they apply to arena-type experiments.

Chapter 2:
Background and Techniques

Spectroscopy is a diverse and broad field that has numerous applications. This chapter outlines some of the fundamentals and quantitative techniques that can be applied to spectroscopy measurements to extract temperature, concentration and other properties. Chapters 3 and 4 expand on the techniques as they apply to the NIR spectrometer developed to study the detonation process.

Czerny-Turner Spectrometer

The Czerny-Turner spectrometer is a versatile tool for use in near ultra-violet, visible, and near-infrared spectroscopy. The major elements and configuration of such spectrometers will be discussed briefly in this section. The basic elements of a Czerney-Turner spectrometer include an input slit, two focusing mirrors, a diffraction grating and a detector. As demonstrated in Figure 2.1 light enters through the input slit and is sent onto the first mirror which collimates the light while reflecting it onto the diffraction grating. The groove pattern of the diffraction grating causes the light to angularly

disperse as it travels toward the second mirror. This mirror then focuses the light onto a detector which converts the incoming light into measurable electrical signals. The Czerny-Turner spectrometer utilizes two mirrors to reduce or eliminate aberrations in the image caused by the use of conventional optics. As initially recognized by Czerny and Turner, the first mirror introduces aberrations in the image that can be partially corrected by a second symmetrical, but oppositely oriented, spherical condensing mirror (Shafer, Megill et al. 1964). In modern spectrometers the use of toroidal optics and asymmetrical designs further eliminates optical aberrations.

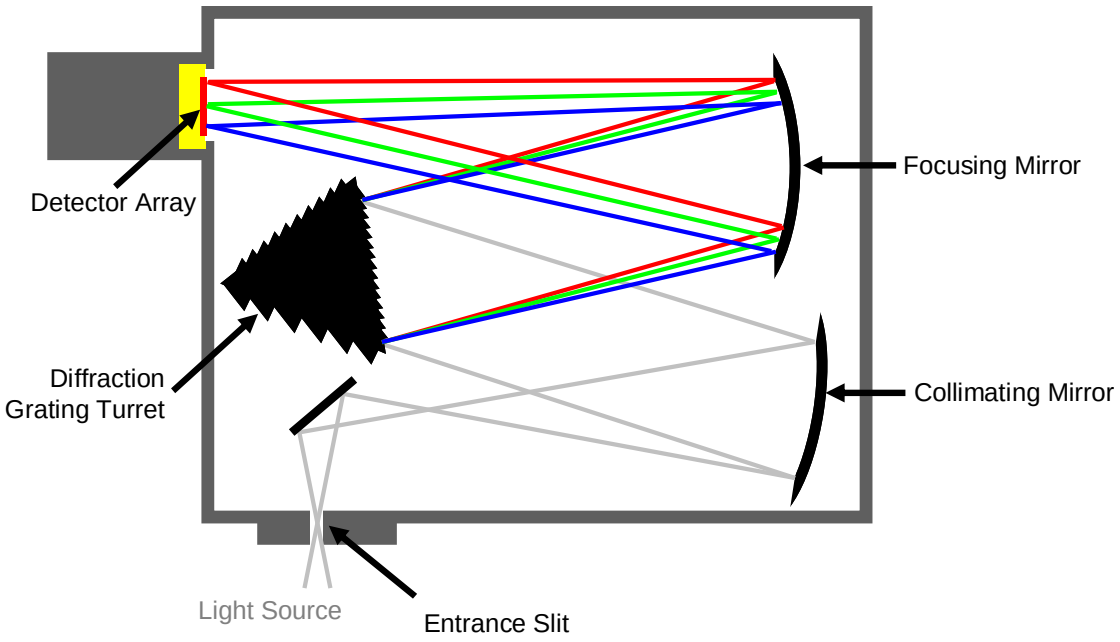

Figure 2.1. Typical Czerney-Turner spectrometer displaying input slit, collimating mirror, diffraction grating, focusing mirror and detector.

In such spectrometers, the resolution of the resulting spectra is dependent upon the slit width, diffraction grating, and detector pitch size. The maximum resolution obtainable by Czerny Turner spectrometers is restricted by the diffraction limit. The size

of the entrance slit can be adjusted to optimize resolution and signal strength; a smaller slit provides more resolution but reduces the amount of light that enters the spectrometer. For spectrometers operating above the diffraction limit, it is also noted that there is a minimum slit width below which no further gains in resolution can be made and is related to the pitch of the detector. This occurs when the spot size at the detector is smaller than the pitch of the detector. The groove density of the diffraction grating determines the angular dispersion of the reflected light and also affects the resolution of the spectrometer. A higher groove density will disperse light more and result in a higher resolution but also reduces the signal intensity. The spectral range collected by the detector is also dependant upon the groove density of the grating; a lower groove density yields a larger spectral range but a lower resolution. Also, the angle of the grating can be adjusted to change the wavelength region that is reflected onto the detector providing a flexible and reliable system. Due to its simple, adjustable design, a Czerney-Turner type spectrometer was used in the construction of a fast NIR spectrometer for the work presented in this thesis and its design will be discussed further in Chapter 3.

Optical Pyrometry

Optical pyrometry is an attractive tool for measuring temperatures in harsh environments that has been utilized to study metallurgy and fuel combustion since the early 1900's (Yiannis, Kelvin Rafael et al. 1992). High-speed pyrometry has been used to study furnaces, shock tubes, and detonation environments to provide fast-response, minimally invasive temperature measurements (Yiannis, Kelvin Rafael et al. 1992; Muller and Renz 2001; Ogura, Okada et al. 2003; Partouche-Sebban, Holtkamp et al.

2005; Goroshin, L. Frost et al. 2006). The theory and method of optical pyrometry has been well documented, and a brief review will be presented in this work.

The pyrometry technique is derived from Planck's law of blackbody radiation which states that spectral radiation of an ideal blackbody radiator is a function of temperature and wavelength. The emission intensity at a specific wavelength (I_λ [$J \cdot s^{-1} \cdot m^{-2} \cdot sr^{-1} \cdot m^{-1}$]) from a blackbody is given by Planck's law in Equation 2.1.

$$I_\lambda = \frac{\varepsilon_\lambda C_1}{\lambda^5}\left(e^{C_2/\lambda T} - 1\right)^{-1} \quad (2.1)$$

Where ε_λ is spectral emissivity, T is temperature of the emitter, λ is wavelength, C_1 and C_2 are constants of 1.91E-16 W m^2 sr^{-1} and 1.439E-2 m K, respectively. To illustrate the basics of optical pyrometry, a two-wavelength method for finding temperatures, outlined by Yiannis *et al.*, will be demonstrated (Yiannis, Kelvin Rafael et al. 1992).

In practical systems, collection lenses, band-pass filters, and photo detectors with less than ideal properties are used to investigate spectral regions and measured signals can be represented by Equation 2.2.

$$S_\lambda = \int_{\Delta\lambda} \eta_L \eta_D \eta_G \frac{\varepsilon_\lambda C_1}{\lambda^{-5}}\left(e^{C_2/\lambda T} - 1\right)^{-1} d\lambda \quad (2.2)$$

S_λ is measured signal intensity from radiation centered at wavelength λ and spanning a bandwidth $\Delta\lambda$. Modifying factors include η_L which includes lens and filter transmittances; η_G including (often unknown) geometric parameters such target size and shape, viewing distance, and other factors; and η_D incorporating detector efficiency. For

the two-wavelength pyrometer, the ratio of signals at wavelengths λ_1 and λ_2 is shown in Equations 2.3 and 2.4.

$$\frac{S_{\lambda_1}}{S_{\lambda_2}} = C_I \left(\frac{\varepsilon_{\lambda_1}}{\varepsilon_{\lambda_2}} \right) \left(\frac{e^{C_2/\lambda_2 T} - 1}{e^{C_2/\lambda_1 T} - 1} \right) \quad (2.3)$$

$$C_I = \left(\frac{\eta_{D_1}}{\eta_{D_2}} \right) \left(\frac{\eta_{L_1}}{\eta_{L_2}} \right) \left(\frac{\lambda_2}{\lambda_1} \right)^5 \left(\frac{\Delta\lambda_1}{\Delta\lambda_2} \right) \quad (2.4)$$

Since the geometry doesn't change between the measurements of the two signals, η_G is eliminated by the ratio. The instrument constant C_I contains all of the ratios for a particular wavelength pair that are independent of the target conditions. Yiannis notes that, in theory this constant could be calculated if such data on each component of the system was available, but this is rarely the case and experimental calibration is the often the only prudent method for determining C_I. To further simplify, the gray-body assumption is often invoked; this eliminates $\varepsilon_{\lambda 1}$ and $\varepsilon_{\lambda 2}$ and reduces Equation 2.3 to a function of temperature only. From a temperature sensitive line-pair ratio ($S_{\lambda 1}$/ $S_{\lambda 2}$) it is then possible to determine the corresponding temperature using a simple least square fitting method.

Wilkinson *et al.* have previously used two-color pyrometry to examine post detonation combustion of aluminized explosives at the Naval Surface Warfare Center in Indian Head Maryland (Wilkinson, Lightstone et al. 2007). Twenty-five millimeter right cylinder charges of aluminized HMX were detonated in a blast-proof chamber. Light

was collected with collimated f/4 lenses into 400 μm fused silica fibers (FiberGuide) and transmitted into an adjacent room as shown in Figure 2.1.

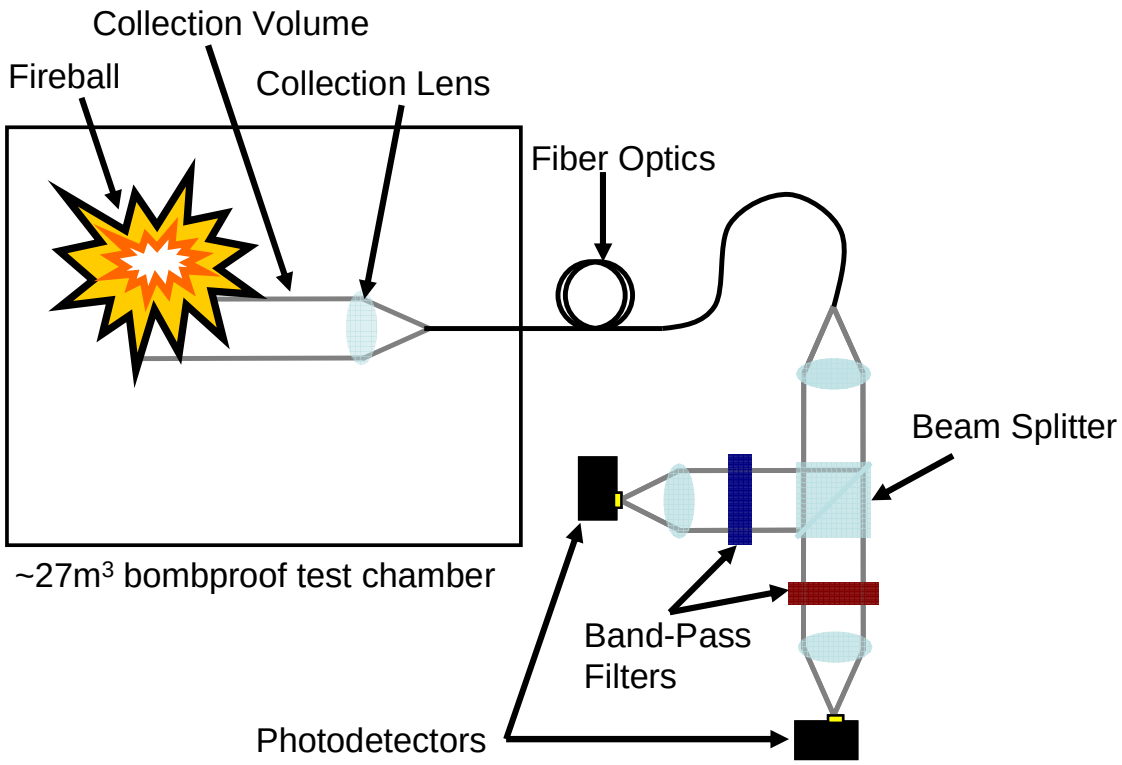

Figure 2.2. Two-color pyrometry setup used for examining explosive events displaying collection optics, transmission fibers, beam splitter and detectors.

Using 10 nm FWHM band-pass filters, light at 800 nm and 1150 nm was monitored by silicon photodiodes (Thorlabs DET-210). To find the instrument constant, the system was calibrated using a blackbody source of known temperature (Oriel QTH; 3200 K). This setup is typical of high-speed pyrometry for use in combustion studies and is similar to the setup that was used in the experiments presented in this work as described in Chapter 3.

Spectral Pyrometry

Spectral pyrometry is a similar technique to optical pyrometry but examines a large wavelength region by resolving the spectra. A detailed study of the spectral pyrometry technique has been performed by Magunov and a brief review will be presented here (Magunov 2009). Recent advancements in high-speed spectrometers allow for spectral pyrometry measurements to be recorded of relevant fast phenomena. The technique has been previously used in diamond-anvil, shock-wave compression, plasma and flame studies (Magunov 2009). When the emission from an object behaves similar to a blackbody (i.e. no atomic, molecular, or other strong features are present), it is possible to determine the temperature of the object by directly comparing the spectra to spectra created from Planck's law without data on its emissivity. This is advantageous as there is seldom adequate emissivity data for complex materials specifically, intermediates of detonation and combustion reactions.

Temperatures of >1000 K can be measured using this technique with a CCD array sensitive in the spectral region of 300-850 nm. Below this temperature, thermal radiation shifts toward longer wavelengths and noise overcomes the signal strength recordable by current devices. When the spectral range is extended to longer wavelengths (up to 1.3 μm), lower temperatures (~700 K) have been measured (McCauley, Israel et al. 1997). The upper boundary of temperature measurements possible from the spectral-pyrometry method is above tens of thousand Kelvins and is estimated by Magunov to be 140,000 K for a spectrometer with an upper wavelength limit of 1 μm. Previous optical pyrometry studies of explosives experiments have recorded post-detonation temperatures in the range of 1000-6000 K. This fits nicely into the measurable range of spectral pyrometry

making it an attractive tool for arena-type explosives experiments. Also, because the spectrum is more sensitive at these temperatures in the near-infrared, the NIR spectrometer developed in this work is well-suited for such measurements.

The accuracy of temperatures determined by spectral pyrometry is somewhat difficult to determine since there are often few alternative sensing methods. Error in measurements is primarily due to two factors: uncertainty in the experimental spectra, and systematic errors in the method. The uncertainty in the method is mostly caused by noise in the measurement and has been quantified as the rms deviation from the mean value determined by the least-squares method. Magunov demonstrates that the uncertainty from noise has been within 2-3% in all previous cases; however this value itself is only a measure of the precision of the method and does not represent the total error present. The systematic errors in the method are primarily due to the gray-body assumption (constant emissivity). It has been observed that for most metals, the emissivity is noticeably a function of wavelength. For example, the emissivity of tungsten at T=2000 K changes almost linearly by $\geq$20% in the range of λ = 500-1000 nm (Magunov 2009). Magunov found that errors for temperatures of metals in which the emissivity was assumed constant, are on the order of several (~2-5%) percent. This amount of error is significant but similar to other methods used in detonation experiments. The use of spectral pyrometry for determining temperature measurements in arena-type explosive experiments using the NIR spectrometer developed in this work is presented in Chapter 3.

Beer-Lambert Relation

The theory of absorption spectroscopy has been detailed previously by several researchers and will be briefly discussed in this section (Arroyo and Hanson 1993; Hanson 2006; Kranendonk, Caswell et al. 2007). The Beer-Lambert law (Equation 2.5) is the fundamental equation that governs experimental absorption spectroscopy and describes the transmission of light through a uniform absorbing medium, as depicted in Figure 2.2.

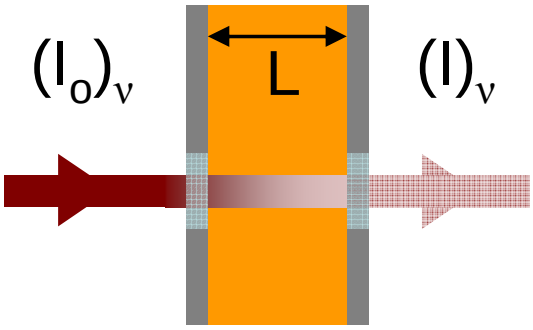

Figure 2.3. Schematic of typical line-of-sight absorption event showing incident $(I_o)_\nu$ and transmitted $(I)_\nu$ light intensity at frequency (ν). Sources used in this work include Nd:YAG lasers and NIR broad optical amplifiers.

$$T_\nu = \left(\frac{I}{I_o}\right)_\nu = \exp(-k_\nu L) \quad (2.5)$$

This law states that the transmission ratio T_ν at a specific optical frequency ν [cm^{-1}] is a function of the spectral absorption coefficient k_ν [cm^{-1}] and the path length L [cm] where I and I_0 are the transmitted intensity and initial intensity at a specific frequency. The product $k_\nu L$ is also known as absorbance α_ν and can be expressed as function of several properties as shown in equation 2.6.

$$\alpha_\nu = k_\nu L = PX_i S_i(T)\phi_\nu L \quad (2.6)$$

P is the total pressure [atm], X_i is the mole fraction of the absorbing species, ϕ_ν [cm^{-1}] is a normalized line shape function and $S_i(T)$ [cm^{-2} atm^{-1}] is the linestrength of the transition at the temperature T [K].

Linestrength is highly dependent on temperature and can be expressed in terms of a known linestrength at a specified reference temperature T_o by the following equation.

$$S(T) = S(T_o)\frac{Q(T_o)}{Q(T)}\left(\frac{T_o}{T}\right)\exp\left[-\frac{hcE''}{k}\left(\frac{1}{T}-\frac{1}{T_o}\right)\right] \times\left[1-\exp\left(-\frac{hc\nu_o}{kT}\right)\right]\times\left[1-\exp\left(-\frac{hc\nu_o}{kT_o}\right)\right]^{-1} \quad (2.7)$$

T is the temperature at which the linestrength centered at frequency ν_o is to be calculated. Constants in equation 2.7 are Boltzmann's constant k [J/K], Planck's constant h [J s], and the speed of light c [cm/s]. $S(T_o)$ is the linestrength at the reference temperature, E'' [J] is the lower state energy of the transition, and $Q(T)$ is the temperature dependent partition function. The partition function can be evaluated for rovibronic or rovibrational energy transitions or determined through empirical correlations. For H_2O transitions, Vidler and Tennyson have created an accurate database of the partition function for temperatures of 10-6000 K through explicit summation of experimental vibration-rotation energy levels (Vidler and Tennyson 2000).

$$\log(Q_{\text{int}}) = \sum_{i=0}^{6} a_i (\log(T))^i \quad (2.8)$$

Equation 2.8 represents a functional fit to their database using the least squares method and coefficients $a_0 - a_6$ are given in Table 2.1.

a_0	- 14.087 469 157 417 9
a_1	37.924 324 853 988 2
a_2	- 42.681 797 873 178 9
a_3	25.330 244 851 791 6
a_4	- 8.108 512 629 355 32
a_5	1.331 068 717 205 35
a_6	- 0.087 298 105 109 575 7

Table 2.1. Coefficients of the fit to the internal partition function Q_{int} for H_2O vapor given by Equation 2.8.

The lineshape function, ϕ_ν, reflects the variations in relative strength of a single transition with respect to frequency. Broadening mechanisms are responsible for the lineshape function and are influenced by temperature, pressure, and gas composition. Many physical mechanisms influence the lineshape function; however, only two dominant broadening mechanisms are considered for the research in this thesis: Doppler (velocity) and collisional (pressure) broadening. Doppler broadening can be represented by a Gaussian distribution with a $\Delta\nu_D$ full-width half-max (FWHM) defined as

$$\Delta\nu_D = \nu_o\sqrt{\frac{8kT\ln 2}{mc^2}} \quad (2.9)$$

where *m* is mass [kg/molecule], *k* is Boltzmann's constant [J/K], and c is the speed of light [m/s]. Collisonal broadening is dependent upon temperature, pressure, and gas composition and follows a Lorentzian distribution and is more difficult to model. The FWHM for collisional broadening, $\Delta\nu_{C,}$ can be described by Equation 2.10.

$$\Delta\nu_C = 2P\sum_A X_A\gamma_{B-A}\left(\frac{T_o}{T}\right)^n \quad (2.10)$$

P is the total Pressure, n is the temperature coefficient, X_A is the mole fraction of species A, and $\gamma_{B\text{-}A}$ is the process-dependent collisional broadening coefficient at reference temperature T_o. Unfortunately, collisional broadening coefficients are not always known and experimental data often must be used to determine $\Delta\nu_C$, the collisional broadening FWHM. In this work, an approximation developed by Kranendonk *et al.* is used to estimate the collisional broadening coeficients. The following equation was developed from 6000 measured spectra spanning 5 to 35 atm (Kranendonk, Caswell et al. 2007):

$$\Delta\nu_C = 0.019 * P + 0.652$$

Where $\Delta\nu_C$ is the FWHM [cm^{-1}] for collisional broadening, and P is the pressure in atmospheres.

Both Doppler and collisional broadening are significant and the lineshape function can be represented using a Voigt profile, which combines Gaussian and Lorentzian distributions. Equations 2.11-2.14 describe a lineshape function with a Voigt profile $\phi_V(\nu)$.

$$\phi_V(\nu) = \phi_D(\nu_o)V(a,w) \quad (2.11)$$

V(a,w) is the Voigt function for which many numerical approximations exist. The Voigt *a* parameter is a function of the FWHM for collisional ($\Delta\nu_C$) and Doppler ($\Delta\nu_{D)}$ broadening as shown in Equation 2.12.

$$a = \frac{\Delta\nu_D\sqrt{\ln 2}}{\Delta\nu_C} \quad (2.12)$$

A non-dimensional line position *w* is described as:

$$w = \frac{2\sqrt{\ln 2}\left(\nu - \nu_o\right)}{\Delta\nu_D} \quad (2.13)$$

The linecenter magnitude, $\phi_V(\nu)$, is given by Equation 2.14

$$\phi_D(\nu_o) = \frac{2}{\Delta\nu_D}\sqrt{\frac{\ln 2}{\pi}} \quad (2.14)$$

A rapid method for the approximation for the Voigt function has been developed by Wells for use when efficient line-by-line calculations are necessary (Wells 1999). The algorithm created by wells is both accurate and efficient and was used in this work.

Direct-Line Thermometry (2-Line Method)

A powerful technique for investigating combustion phenomena is direct-line ratio thermometry. Direct-line thermometry can be applied to both emission and absorption spectroscopy and has recently been used to measure temperatures in the harsh environments of laser ablation and detonation events (Lightstone, Carney et al. 2007; Lewis and Rumchik 2009). The theory and background for the direct-line ratio technique in absorption studies has been described previously in the literature and a brief review will be presented here (Ouyang and Varghese 1990; Arroyo, Langlois et al. 1994; Hanson 2006).

The linestrength of a particular transition is dependent on temperature as described in Equation 2.7. By taking a ratio of the integrated absorbance areas for two transitions *(R)*, the pressure and species concentration parameters are removed, leaving only the temperature and lower state energies for the transitions as shown in Equation 2.15.

$$R = \frac{S(T_o,\nu_1)}{S(T_o,\nu_2)} \exp\left[-\left(\frac{hc}{k}\right)\left(E_1'' - E_2''\right)\left(\frac{1}{T} - \frac{1}{T_o}\right)\right] \quad (2.15)$$

$S(T_o,\nu_1)$ and $S(T_o,\nu_1)$ [cm^{-2} atm^{-1}] are the linestrengths (at the reference temperature, T_o) of the transitions centered at ν_1 and ν_2 [cm-1] respectively. The lower state energies for the two transitions, E_1'' and E_2'' [cm^{-1}], are typically known from quantum-mechanical calculation or from measurement. Thus, for a given pair of lines, the intensity ratio is a function of temperature only and from a measured intensity ratio, the temperature T [K] can be found from Equation 2.16.

$$T = \frac{\frac{hc}{k}\left(E_2'' - E_1''\right)}{\ln R + \ln\frac{S(T_o,\nu_1)}{S(T_o,\nu_2)} + \frac{hc}{k}\frac{\left(E_2'' - E_1''\right)}{T_o}} \quad (2.16)$$

The differentiation of Equation 2.16 yields the temperature sensitivity for a given line pair at a specific temperature as shown in Equation 2.17.

$$\frac{dR}{dT} = \frac{hc}{k}\frac{\left(E_1'' - E_2''\right)R}{T^2} \quad (2.17)$$

This equation is of particular importance when selecting appropriate line pairs with adequate sensitivity for temperature determinations. A useful parameter for selecting line pairs for investigations of specific temperature ranges is the peak sensitivity temperature T_p and can be found from Equation 2.18.

$$T_p = \left(\frac{hc}{k}\right)\left(E_1'' - E_2''\right) = 0.72\Delta E'' \quad (2.15)$$

Ouyang and Varghese have demonstrated that the selection of line pairs is critical to the sensitivity and accuracy of this technique and proposed a set of criteria for selecting spectral lines based on spectral line resolution, thermal sensitivity, absorption strength, and insensitivity to systematic errors (Ouyang and Varghese 1990).

Broad H_2O Absorption Thermometry

Using wavelength-swept lasers or broadband light sources, it is possible to rapidly measure absorption spectra from an absorbing medium. H_2O absorption spectra are of particular interest to combustion studies since water is a major product of most combustion processes. Because it is already present, this eliminates the need to seed absorber molecules into the flow and can give direct measurements of key parameters. Kranendonk *et al.* have developed a robust method for determining temperature and mole fraction H_2O from measured absorption spectra in combustion environments (Kranendonk, Caswell et al. 2007; Kranendonk, Huber et al. 2007). The H_2O absorption method, which will be reviewed here, shows much potential for use in detonation environments and Chapter 4 of this work presents a feasibility study for implementing this method with the newly develop NIR spectrometer in arena-type explosive environments.

As demonstrated previously, absorbance can be considered dependent upon pressure, temperature, mole fraction absorber. If relevant spectroscopic parameters are known, it is possible to quantitatively determine these properties from measured spectra. The values for such spectroscopic coefficients and parameters can be found in various databases such as HITRAN and HITEMP. Recently, Barber *et al.* have developed the

BT2 database, a high-accuracy computed water line list of infrared transition frequencies and intensities (Barber, Tennyson et al. 2006). Using the BT2 database and the relations outlined previously, it is possible to simulate H_2O absorption spectra for conditions relevant to combustion and detonation processes. By comparing measured and simulated spectra, temperature and mole fraction H_2O, can be accurately determined using the method demonstrated by Kranendonk *et al*. This comparison can be performed at virtually any wavelength; however, it yields the best results when the investigated region contains strong lines that are highly dependent on the sought properties. The region of 1330-1380 nm, containing the entire R-branch of the $\nu_1 + \nu_3$ band of H_2O, is suited for such investigations as it includes lines with all available lower-state energies, guaranteeing that the measured spectra includes the optimum line pairs regardless of the experimental conditions.

As stated, a database is created consisting of spectra across a range of temperatures and pressures. For the measured spectra to be compared to this database to successfully determine the properties that exist in the measured spectra, both spectra must have the same resolution wavelength range and resolution. First, calibration of the wavelength axis is performed for the measured spectra by measuring a spectrum at room temperature and pressure (T=295 K, P=1 atm) and fitting the wavelengths of measured peaks to a simulated spectrum at the same conditions using a least-squares fit as shown in Figure 2.4. The wavelength axis is then converted into frequency using equation 2.16. Wavelength (λ) is in nanometers and wavenumber (ν) is in inverse centimeters.

$$\nu = \frac{1}{\lambda} 1.0E7 \quad (2.16)$$

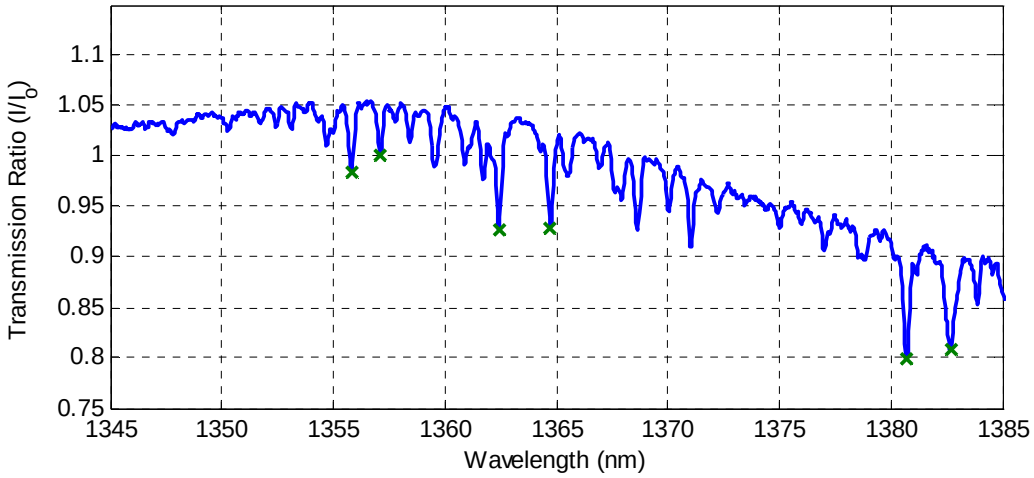

Figure 2.4 Calibration of wavelength axis performed by fitting peaks from measured spectrum (blue) at room conditions (T=295K P=1atm) with known peaks from simulated spectrum (shown by green x's).

The measured transmission spectrum is obtained by taking the ratio of the initial intensity I and transmitted intensity I_o. A sample transmission spectrum taken in a furnace at an elevated temperature (T=700 K) from the spectrometer and plotted by wavenumber is shown in Figure 2.5.

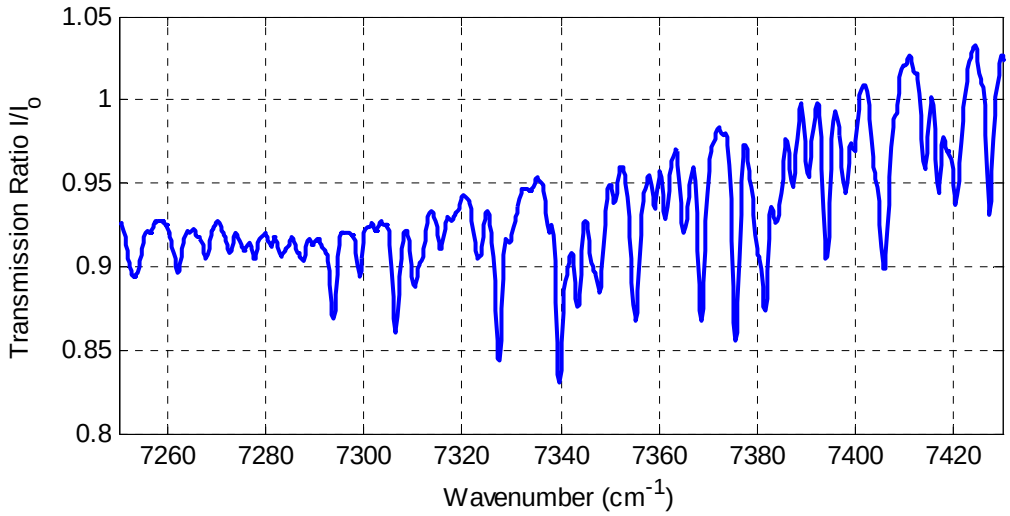

Figure 2.5 Sample transmission spectrum plotted vs. frequency from spectrometer taken in a furnace at elevated temperature (T=700K, P=1 atm).

The transmission spectrum is then converted to absorbance α_ν, by beer's law, and divided by the path length to obtain the spectral absorption coefficient k_ν (Equations 2.17-18).

$$T_\nu = \left(\frac{I}{I_o}\right)_\nu = \exp(-\alpha_\nu) \quad (2.17)$$

$$\alpha_\nu = k_\nu L \quad (2.18)$$

Where T_ν is the transmission ratio at a specific optical frequency ν [cm^{-1}], α_ν is absorbance, L is the path length [cm], I and I_0 are the transmitted intensity and initial intensities and k_ν [cm^{-1}] is the spectral absorption coefficient. Figure 2.6 shows measured absorption coefficients vs. frequency from the data in Figure 2.5.

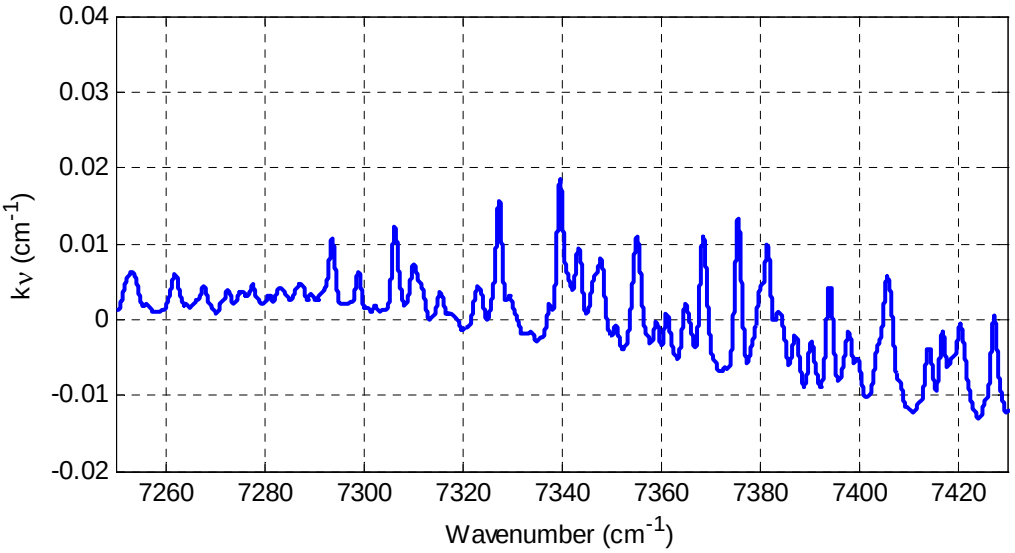

Figure 2.6 Absorption coefficients (k_ν) plotted vs. frequency from data in Figure 2.5 taken in a furnace at elevated temperature (T=700K, P=1 atm).

To facilitate the comparison of the simulated and measured spectra, the frequency axes of the two must be identical. Various methods of accurate interpolation exist and can be used to interpolate the spectra. In this work a piecewise cubic Hermite

interpolating polynomial is used to create closely matched interpolated data since Hermite interpolation matches data points in both value and first derivative. Figure 2.7 displays the interpolated measured spectrum from Figure 2.6 and interpolated simulated spectrum at a temperature of 700 K and pressure of 1 atmosphere.

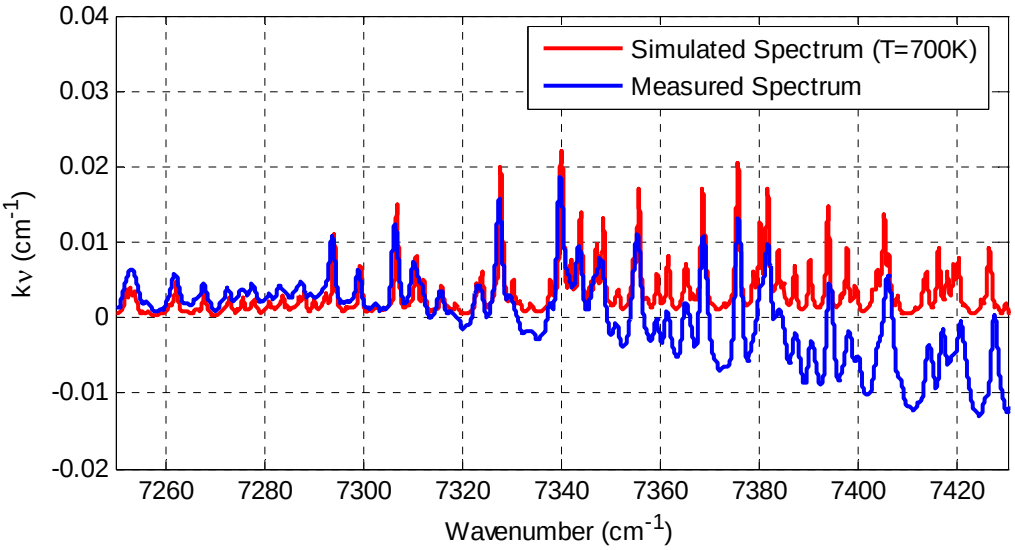

Figure 2.7 Absorption coefficients (k_v) plotted vs. frequency from data in Figure 2.6 taken in a furnace at elevated temperature (T=700K, P=1 atm).

To remove high-frequency noise that can be present in the measured spectrum, a smoothing process can be implemented through the convolution of a Gaussian pulse. The optimum degree of smoothing is carefully considered. The measured spectrum is smoothed by the convolution of a Gaussian pulse of Full-Width Half-Max (FWHM) of $\Delta\nu_G$ to remove high frequency noise but not eliminate major features of the spectra. It was found that smoothing the measured spectra to $\Delta\nu_G$ of 1.5 cm^{-1} was sufficient to remove high-frequency noise while retaining the major features. The simulated spectra are also smoothed to incorporate the broadening caused spectral resolution of the

instrument. A mean-squared method is used to match the smoothing of the measured and simulated spectra described in Equation 2.19.

$$\Delta\nu_{sim} = \sqrt{\Delta\nu_G{}^2 + \Delta\nu_{instr.}{}^2} \quad (2.19)$$

The FWHM smoothing factor for the simulated spectra $\Delta\nu_{sim}$ [cm^{-1}] is determined from the smoothing factor chosen for the measured spectra $\Delta\nu_G$ [cm^{-1}] and the spectral resolution of the instrument $\Delta\nu_{instr.}$ [cm^{-1}]. Figure 2.8 shows smoothed measured and simulated spectrum from the data in Figure 2.7.

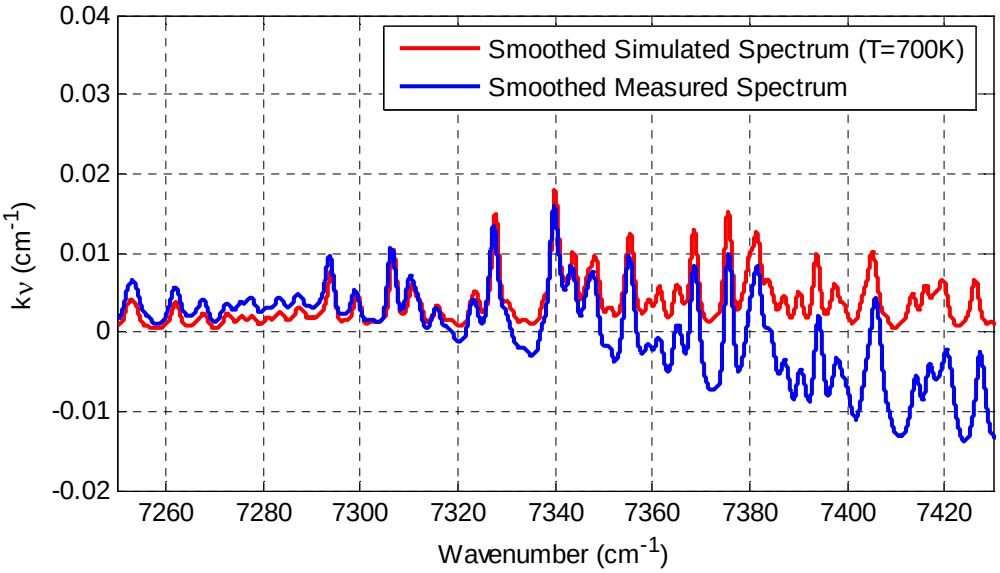

Figure 2.8 Smoothed absorption coefficients (k_ν) plotted vs. frequency from data in Figure 2.7 taken in a furnace at elevated temperature (T=700K, P=1 atm).

It can be seen in Figures 2.7 and 2.8 that large spectral offsets and low frequency noise exist in the measured spectrum causing negative absorption coefficients. Artificial or unrelated features can be added to the spectra by wavelength dependent interferences from broadband absorbers, window fouling, and beamsteering, and such offsets make direct comparison of the spectra problematic. It has been demonstrated that taking the

derivative of the smoothed spectra eliminates these offsets and is a convenient systematic method for processing measured spectra (Kranendonk, Caswell et al. 2007; Kranendonk, Huber et al. 2007). The data in Figure 2.7 was differentiated and is plotted in Figure 2.8.

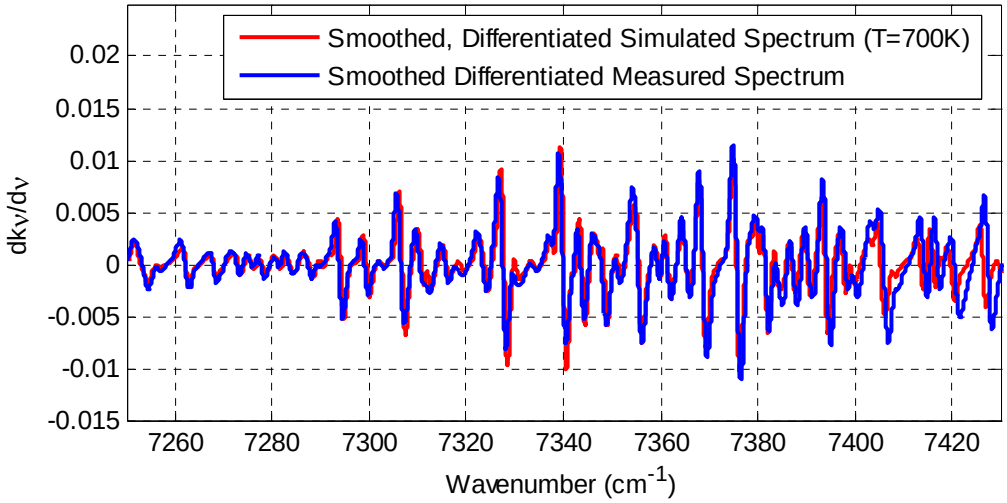

Figure 2.9 Smoothed, differentiated absorption coefficients (k_v) plotted vs. frequency from data in Figure 2.8 taken in a furnace at elevated temperature (T=700K, P=1 atm).

The measured and simulated spectra are now ready for comparison. To determine temperature, the measured smoothed differentiated spectra can then be plotted individually versus each of the smoothed differentiated simulated spectra at the measured pressure (from a pressure transducer). A line is fit through each plot using the general linear least squares method as a maximum likelihood estimator. The mean squared error (MSE) of each fit is calculated and recorded. Figure 2.10 shows the smoothed, differentiated measured data plotted versus smoothed, differentiated simulated data at two different temperatures. The MSE describes the quality of the fit, with the lowest MSE being the best fit spectra.

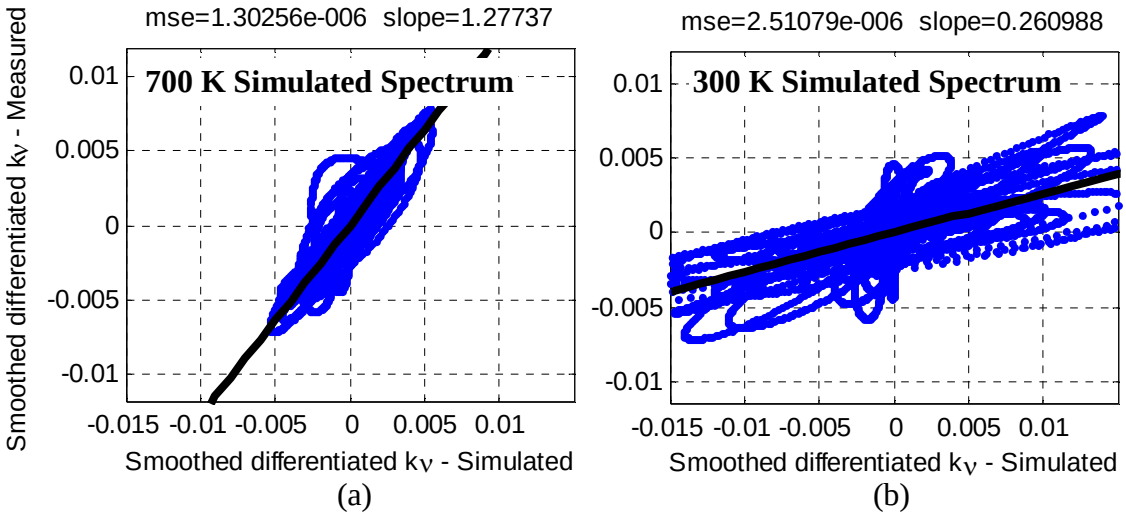

Figure 2.10 Measured versus simulated smoothed, differentiated absorption coefficients from data in Figure 2.9. (a) Measured coefficients compared to simulated coefficients at T=700 K, with a MSE of 1.3e-6 this is the best fit. (b) Measured coefficients compared to simulated coefficients at T=300 K, with a MSE of 2.5e-6 this is a poor fit.

The mean-squared error (MSE) for each condition is then plotted versus simulated temperature. The minimum MSE is interpolated from this and its location corresponds to the temperature of the measured spectra. For the data in this calculation, a temperature of 690 K was determined at the minimum MSE.

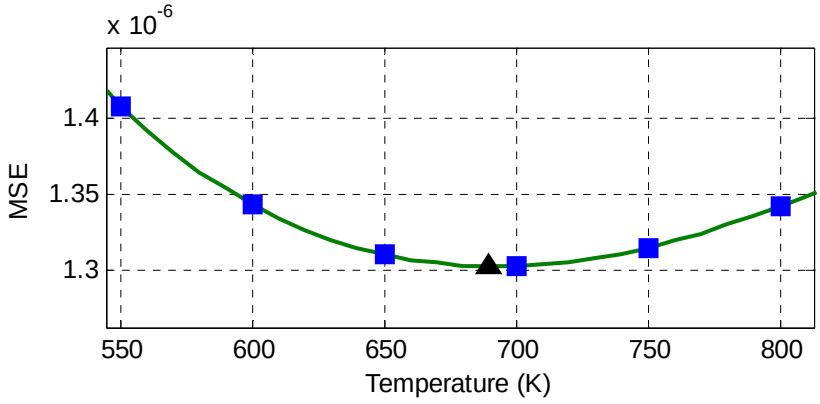

Figure 2.11 Mean-squared error versus simulated temperatures from the data in Figure 2.9. Square points are calculated from the simulated spectra. The black triangle indicates the min. MSE and predicted temperature of the measured spectrum.

Once the temperature has been calculated, mole fraction H_2O can be determined. The slope of the best fit lines from the measured versus simulated spectra can be plotted versus temperature as shown in Figure 2.12. The slope at the calculated temperature can then be interpolated from this plot.

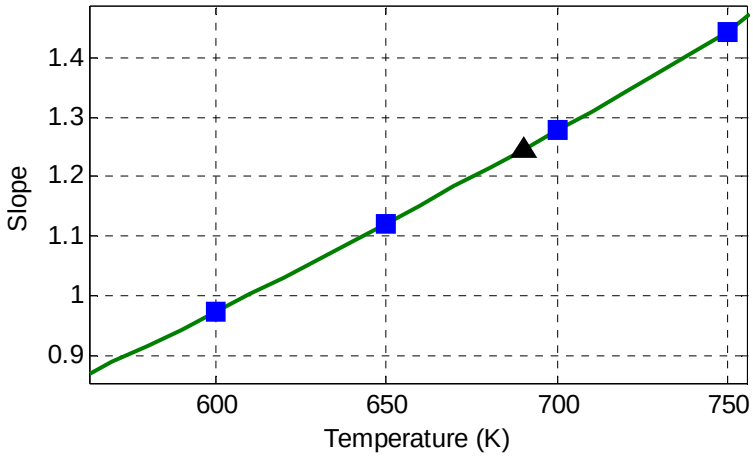

Figure 2.12 Slopes of the best-fit lines from the measured versus simulated data in Figure 2.9. Square points are calculated from the simulated spectra. The black triangle indicates the predicted slope for the best-fit line of the measured spectrum.

Since the mol fraction of the simulated spectra $(x_{sim.})$ is known, the interpolated slope (sl) can be used as a scaling factor to determine the mol fraction H_2O of the measured spectra $(x_{meas.})$ as shown in Equation 2.20.

$$x_{meas.} = sl \cdot x_{sim.} \quad (2.19)$$

For example, the database of spectra used in this work were simulated at x=0.2126 mole fraction water. The slope of the best fit temperature is found to be 1.246; using Equation 2.20, the mole fraction of water in the measured spectrum is 0.265. This linear scaling with mole fraction assumes that the gas is following the ideal gas law.

The methods presented here have been successfully used in combustion engines, gas turbines, and shock tubes and has been found to be highly accurate, within 2% at 3000 K (Hagen and Sanders 2007; Kranendonk, Caswell et al. 2007; Kranendonk, Caswell et al. 2009). A feasibility study of this method for investigation of arena-type explosives experiments is discussed in Chapter 4.

Chapter 3:
Near Infrared Emission Spectroscopy for Examining Post-Detonation Combustion of PETN Based Explosives

Introduction

As discussed in Chapter 1, advanced high explosives formulations with low peak pressure, high persistent temperature, and the inclusion of anti-microbial particles such as Ag are desired for use in agent defeat. In order to effectively create formulations with tailored properties, a better understanding of the chemical kinetics and decomposition pathways of such explosives is necessary. Conventional measurements employed in arena-type experiments such as detonation velocity and pressure history provide valuable data; however, temperature and species concentration measurements can provide more detailed information on chemical transients furthering understanding of the underlying chemical kinetics (Carney, Miller et al. 2006; Petersen, Arvanetes et al. 2007). The harsh environment and short-timescales present in arena-type explosives experiments limits the measurement techniques that can be employed and optical methods have shown to be

minimally invasive, fast-response methods for making such measurements (Gross, Dills et al. 2003; Carney, Miller et al. 2006; Goroshin, L. Frost et al. 2006; Wilkinson, Lightstone et al. 2007). High-speed ultra-violet and visible emission spectroscopy has been employed in past arena-type explosive experiments examining aluminum features and temperatures determined from them (Carney, Miller et al. 2006). With the recent development of a novel fast InGaAs array, such measurements can be expanded to the near-infrared region.

In this chapter, the development of a new high-speed NIR spectrometer for application to explosives experiments is detailed. The system's development, characteristics, and example results are described below.

Experimental Setup

This section will describe the experimental setup of the near infrared spectrometer used for measuring temporally resolved emission spectra of silver and aluminum doped PETN explosives at the Naval Surface Warfare Center in Indian Head, MD.

Naval Surface Warfare Center, Indian Head Facilities

Experiments were carried out at the Sigmund J. Jacobs Detonation Science Facility at the Naval Surface Warfare Center, Indian Head division. The facility included a bombproof chamber approximately 30 kiloliters in volume that was used as the detonation arena. Sensitive instrumentation and other experimental equipment were kept in adjacent rooms, shielded from the blast environment. The test setup within the bombproof chamber is shown in Figure 3.1. The test stand consisted of ½ inch stainless

steel rods held vertically by weighted feet and set on a sheet of plywood over a large steel cylinder. A crossbar was attached to the vertical rods by 90 degree clamps and the explosive charge assembly was hung from the crossbar by the charge firing wires. A sacrificial wood dowel was used to aid in holding the charge vertically in place long enough for the experiment to be safely executed. The collection lens tube assembly was mounted ~1.3 meters to the side of the vertically mounted charge and held in place by clamps attached to a weighted stand.

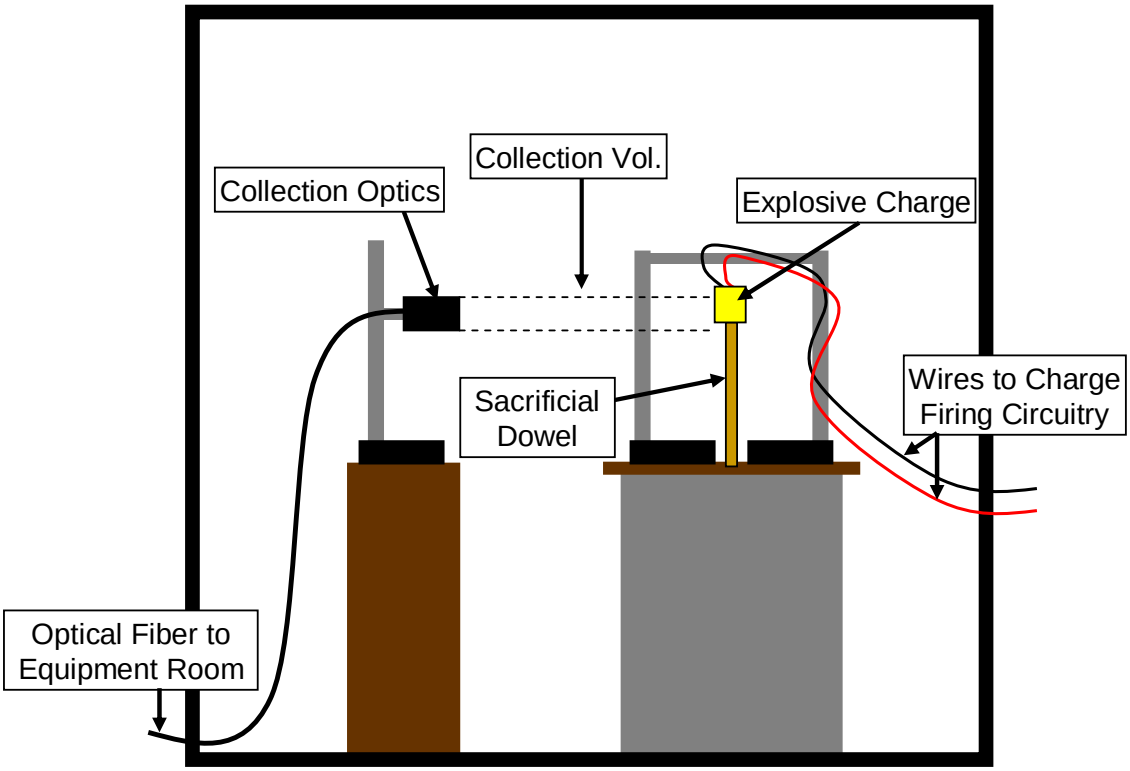

Figure 3.1. Experimental configuration for NIR emission spectroscopy experiments in a 30 kL blast-proof chamber at the Naval Surface Warfare Center in Indian Head, Maryland. The explosive charge was suspended by the detonating wires and the collection optics were mounted ~1.3m to the side of the charge.

For the collection assembly, a 1 inch diameter, 4 inch focal length plano-convex lens was mounted in a lens tube 4 inches from the collection fiber. A helium-neon laser was used

prior to the test for alignment purposes to ensure that the lens-fiber assembly created a 1 inch diameter collimated cylindrical collection volume from the lens to the target. The fibers used were 400 μm diameter, low-OH silica fibers (Fiberguide AFS400-440Z) with a numerical aperture of 0.22. Light collected by the lens assembly was transmitted by the fibers to an adjacent room where it was transmitted into the near-infrared spectrometer. The spectrometer's setup and capabilities will be detailed in the following section.

Twenty-five millimeter right cylinder charges were used in a setup similar to those performed previously at Indian Head (Carney, Miller et al. 2006; Carney, Wilkinson et al. 2007; Wilkinson, Lightstone et al. 2007). The charge assembly consisted of an RP-80 exploding bridgewire detonator, followed by a Detasheet booster (25 mm diameter x 6 mm thick), and the main charge (25 mm diameter x 25 mm thick). Charges were either composed of pure PETN or 90% (by mass) PETN with a 10% load of microparticles. Table 3.1 lists the different formulations that were used in these experiments.

Formula Number	**Formulation (% by mass)**		
P	100% PETN		
S-1	90% PETN	10% Ag (84um)	
S-2	90% PETN	10% Ag (1um)	
SI	90% PETN	10% AgIO3 (1um)	
SCA	90% PETN	10% Ag-coated Al (H5)	
SA-1	90% PETN	5% Ag (5um)	5% Al (H5)
SA-2	90% PETN	5% AgIO3 (1um)	5% Al (H5)

Table 3.1. Explosive formulations used in arena-type explosives experiments at the NSWC, IH.

As discussed in Chapter 1, silver and silver-iodate were used because of their potential for agent defeat (Morones, Elechiguerra et al. 2005; Sambhy, MacBride et al. 2006). Aluminum was used because of its potential to maintain a higher post-detonation temperature to enhance the biocidal activity of the silver (Russell 1990; Levi 2004; Goroshin, L. Frost et al. 2006).

To fire the charges, a 500 V pulse generator was used and timing was controlled by Stanford Research Systems DG535 digital delay generators. The spectrometer was triggered in advance of the detonator trigger pulse so that at least two frames of background signal were recorded before the charge was detonated. It was found that first light emerged from the charge approximately 8 μs following the detonator trigger pulse, and the delays for each instrument were adjusted accordingly.

NIR Emission Spectrometer

Light from the bombproof chamber was transmitted to an adjacent room by the optical fibers and emitted into a 300 mm, Andor Shamrock 303-i spectrometer. The spectrometer had three different dispersion gratings (300 g/mm, 600 g/mm, and 1000 g/mm) internally mounted on a turret allowing for different spectral resolution. For optimal dispersion in the near-infrared, the gratings were blazed at 1.3μm. For these measurements, the 300g/mm grating was used and the entrance slit width was 200 μm. The spectral resolution in these emission experiments was low, about 2.5 nm, limited predominantly by the size of the fiber and input slit to the spectrometer. A coarser spectral resolution was chosen in order to obtain broad spectral coverage (~250nm) and collect sufficient signal from a stand-off distance of more than a meter from the small

charge. Finer gratings (1,000 g/mm) and smaller fibers (9 μm) have been used with the system to achieve a spectral resolution of 0.093 nm and spectral range of ~45 nm for use in the water absorption study discussed in Chapter 4; however, a brighter light source or larger faster optics are required to collect emission at such higher resolutions.

After the light was dispersed, it was focused onto 1x1024 pixel InGaAs array (Goodrich Sensors Unlimited Inc., SU-LDH Digital Line Scan Camera).

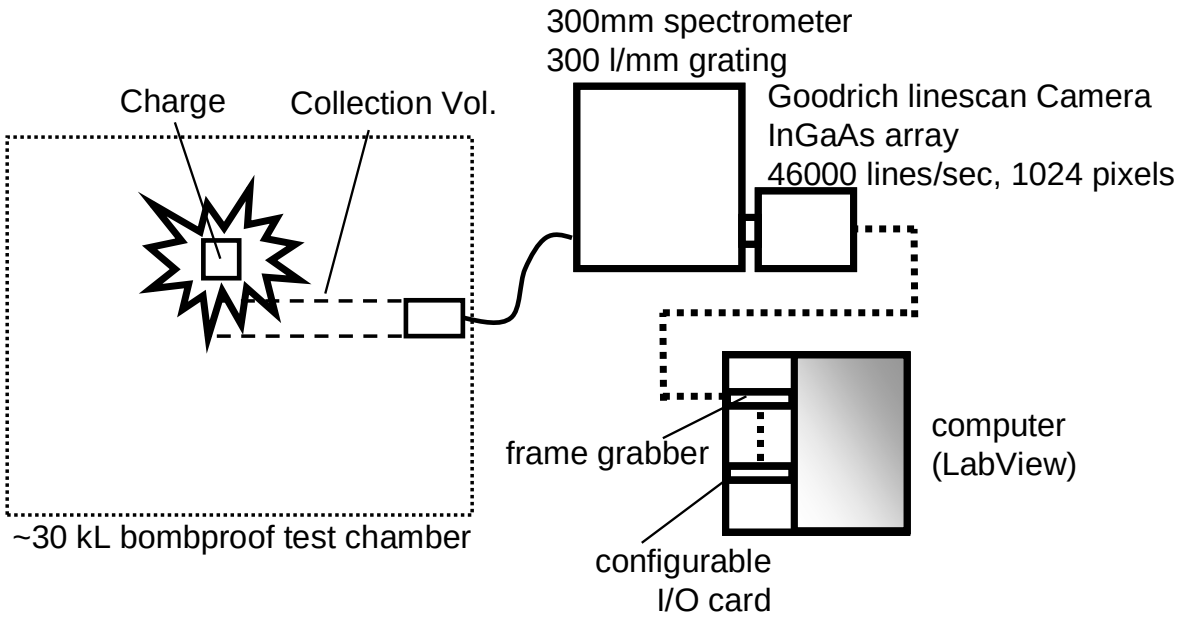

Figure 3.2. Experimental configuration of emission experiments. Light is collected in the bombproof chamber by a lens assembly and focused onto 400 μm fiber optic cables. The fibers transmit the light into an adjacent shielded room where it enters the spectrometer which is controlled by a LabView based DAQ program.

As shown in Figure 3.2, a LabView-based acquisition program controlled the camera and was capable of acquiring up to 10,000 spectra per detonation once an external trigger was received (which was generated by the charge-firing circuitry). It is noted that the number of spectra that can be acquired by the system is limited by the amount of RAM in the

DAQ computer and that it is easily possible to capture more spectra with greater amounts of RAM.

The InGaAs array was a CCD linescan camera with a 1x1024 array of 500 μm tall pixels with a pitch of 25μm. To facilitate high-speeds, the camera employs an integrate – while-read acquisition, and is capable of 47,348 lines read per second. The typical quantum efficiency of the array given by the manufacturer is shown in Figure 3.3 and shows a wavelength response over 0.8 μm to 1.7 μm.

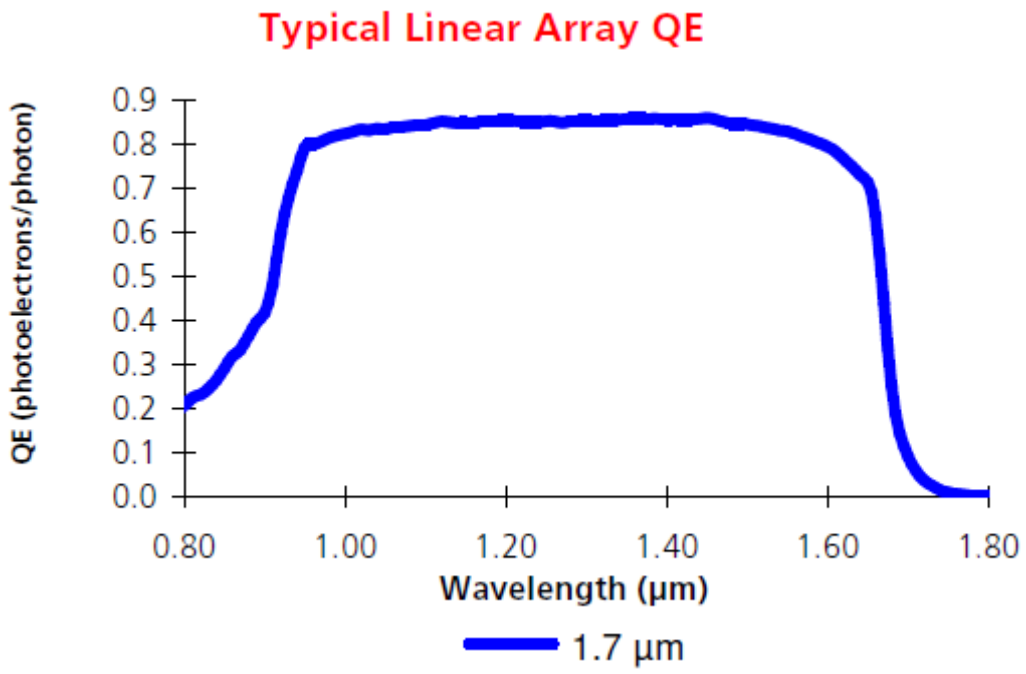

Figure 3.3. Quantum efficiency curve of Goodrich Sensors Unlimited Inc., SU-LDH Digital Line Scan Camera, supplied by manufacturer.

Settings on the camera were easily adjusted to maximize the signal to noise ratio using the LabView based DAQ program. The sensitivity of the camera could be adjusted to three different levels corresponding to the coupled gain capacitors allowing for greater versatility of the system. For these experiments, the camera was set to its maximum

sensitivity to ensure adequate signal to noise ratio at fast operating speeds. The camera could be set to 4 different trigger modes: free run, single line per trigger, programmable exposure, or gated burst. For these experiments the single trigger generated from the charge firing circuitry was used to initiate a free run exposure with the exposure setting selected to maximize signal to noise ratio while keeping high temporal resolution. The camera's timing and operation are outlined in Figure 3.4.

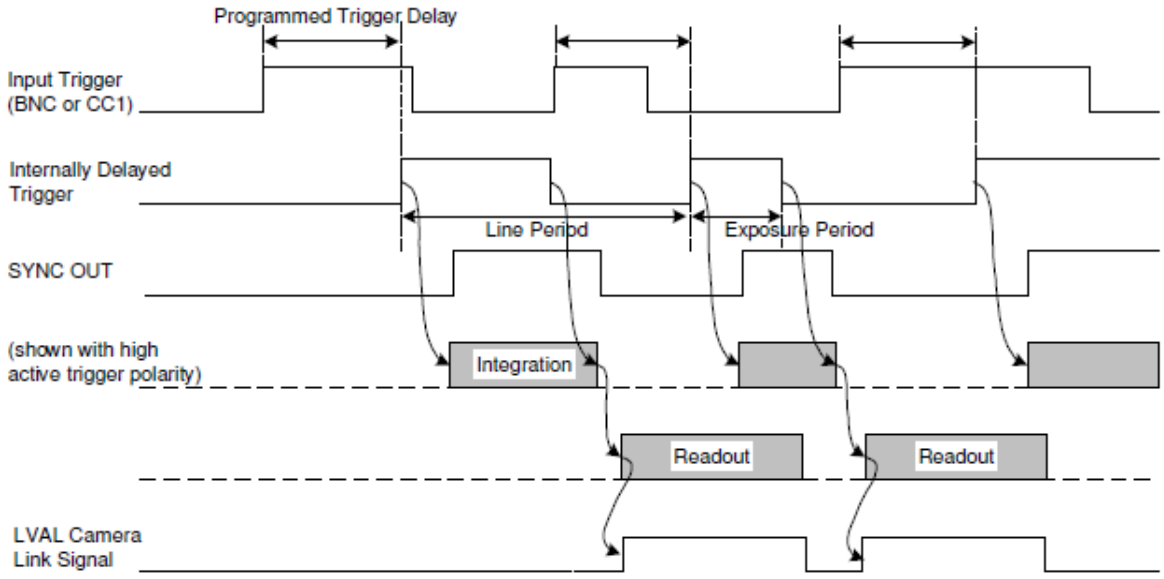

Figure 3.4. Timing diagram of Goodrich Sensors Unlimited Inc., SU-LDH Digital Line Scan Camera, supplied by manufacturer.

For each external trigger the camera receives there is a set delay of 6.68 µs before the camera begins operation. The camera then integrates for the specified interval, holds the signal, and then reads the value. This sample and hold process requires that 3.92 µs of each frame be reserved for the supplementary camera processes. This means that the total integration time will be 3.92 µs shorter than the given frame rate as demonstrated in Equation 3.1.

$$T_{\max \exp} = T_{frame} - INT_{low} - \frac{38}{P} \quad (3.1)$$

The maximum exposure period (T_{maxexp}) is a function of the frame period (T_{frame},) the parameter (INT_{low}) (0.880 μs for this camera), and the pixel rate (P) of the camera (12.5 MHz). At the fastest factory setting (46,992 spectra/sec), the camera's duty cycle was only 65%. That is, of the 21.3 μs that were required to take one spectrum, the camera only integrated for 13.9 μs. There was thus a trade-off between the speed of operation and the fraction of the signal that could be collected from the explosion. Some explosions were thus observed using a slower setting – 16,846 spectra/sec with a 93% duty cycle – to ensure that adequate signal-to-noise could be obtained.

Data Reduction procedure

Post-processing and data reduction methods were performed in Matlab. Wavelength calibration was performed using an argon lamp (Oriel). To correct for the relative spectral response of the system, an efficiency image was acquired by collecting light from a known blackbody source (Oriel Model 68835 power supply with QTH lamp, 3300 K). To obtain a relative spectral response of the system, a black body spectrum at 3300 K was simulated from the Planck equation and compared to the measured spectrum from the QTH lamp. The measured spectral response of the system is shown in figure 3.5 along with a calculated spectral response of the system. The calculated spectral response was determined from efficiency curves of the major components in the system including the collection lenses, optical fibers, dispersion grating, and InGaAs array. The dispersion grating and InGaAs array contribute the most to the calculated spectral response.

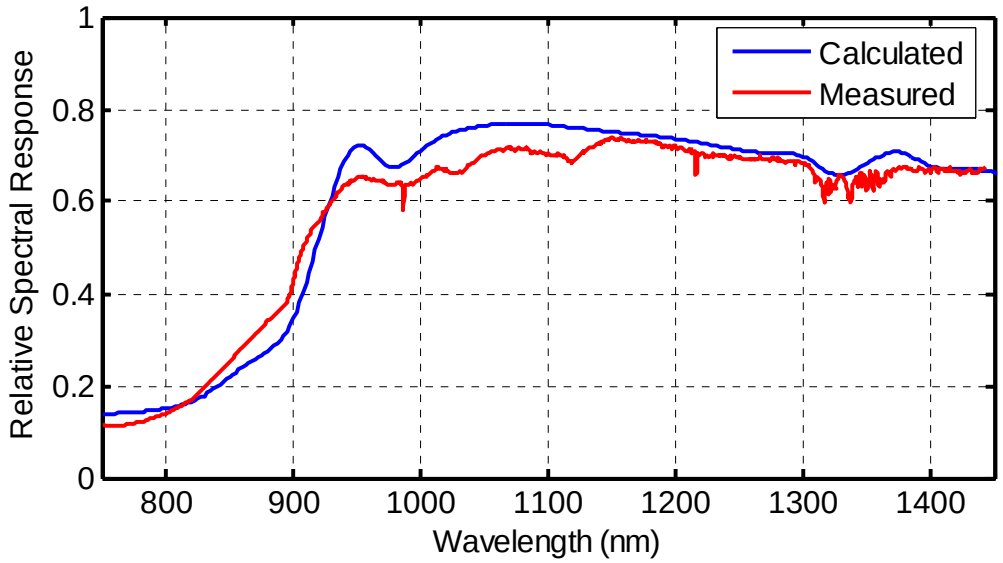

Figure 3.5 Calculated and measured spectral response of the system.

The measured and calculated spectral responses are fairly similar, deviating less than 10% across the spectra. The differences between the two responses are likely due to three factors: absorption from molecules in the spectrometer (there is significant absorption from H_2O at 1330-1380 nm), an efficiency curve for the detector that is slightly different from the manufacturer's typical curve (Figure 3.3), and deviation from gray body behavior by the QTH lamp used to determine the measured spectral response.

Due to time limitations, it was unfeasible to record a new spectrum from the QTH lamp before each experiment. In order to expedite the acquisition process, a spectrum from a second tungsten halogen lamp (Mikropack GmbH, HL-2000-HP) was recorded for each of the QTH measured spectra at the same setting. The Mikropack lamp required very little time for warm up and was easily fiber coupled minimizing turn-around time between experiments. The relative spectral response obtained from the QTH lamp was compared to the measured spectrum obtained from the Mikropack lamp to obtain the relative spectral response of the system with respect to the Mikropack lamp.

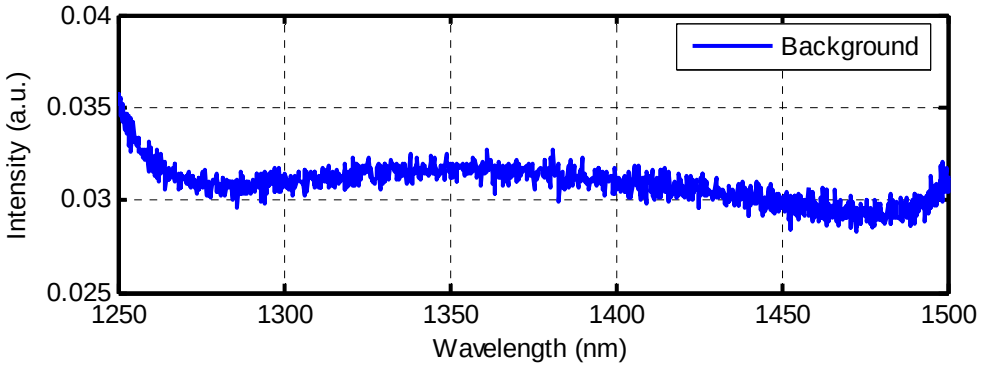

(a)

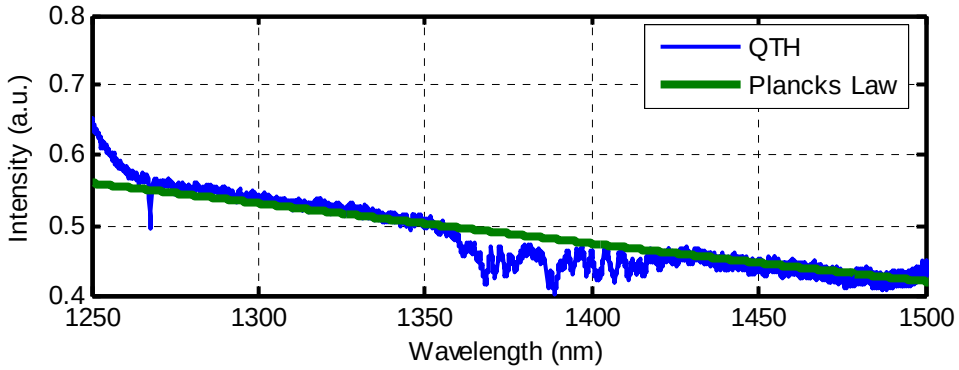

(b)

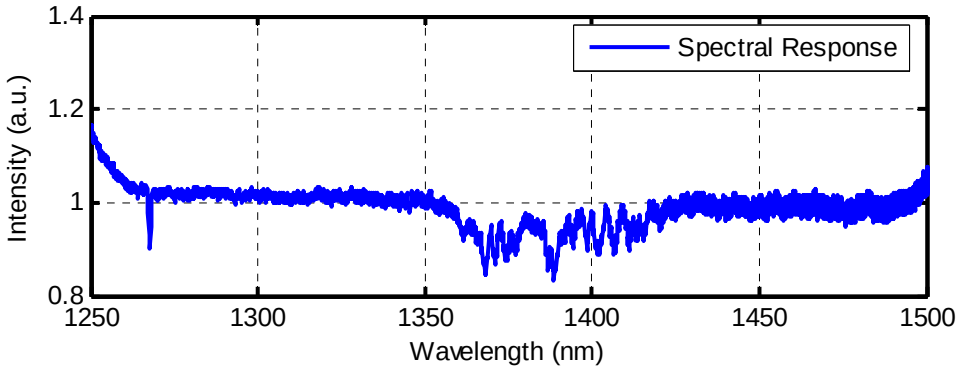

(c)

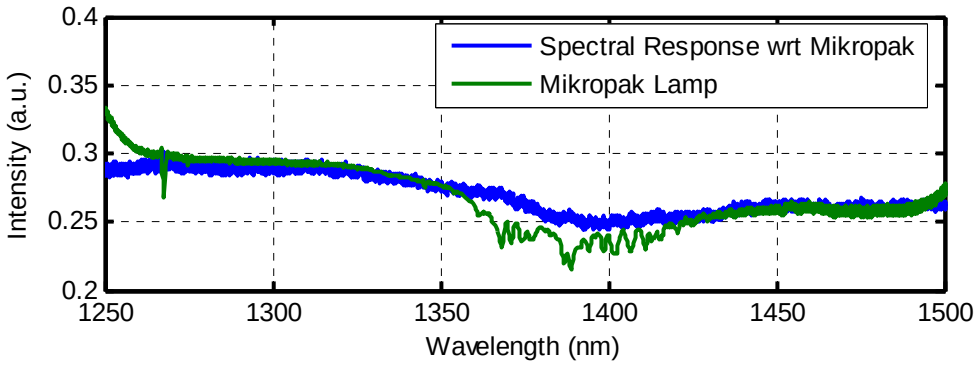

(d)

Figure 3.6 Data reduction steps to obtain relative spectral response of the system with respect to the Mikropak Lamp.

The steps for obtaining this relative spectral response are demonstrated in Figure 3.6. Background subtraction was performed to all measured spectra by subtracting an averaged background image taken previous to each measured spectrum. A sample background image is shown in Figure 3.6 (a); the intensity is normalized by the maximum intensity of the camera (i.e. saturation =1). Figure 3.6 (b) shows a sample image of the QTH lamp and a gray-body simulated at T=3300 K from Planck's law. The spectral response of the system (Figure 3.6 (c)) is obtained by dividing the measured spectrum from the QTH lamp by the simulated gray-body. A spectrum from the Mikropak lamp is then measured and the relative spectral response with respect to the Mikropak lamp is obtained by dividing the Mikropak spectrum by the spectral response of the system as shown in Figure 3.6 (d).

Then, for each experiment, a background spectrum, and a spectrum of the Mikropack lamp were acquired just before conducting the experiment. Figure 3.8 (a) shows the overall spectral response of the system for the shot that is determined by dividing the spectrum from the Mikropak acquired before the shot by the relative spectral response with respect to the Mikropak lamp. Figure 3.8 (b) shows raw emission data from the detonation and the data after it has been spectrally corrected by dividing the raw data by the overall spectral response from Figure 3.7 (a). Finally, Figure 3.8 (c) shows the spectrally corrected emission data after it has been smoothed to eliminate high-frequency noise and make the relevant features easier to see.

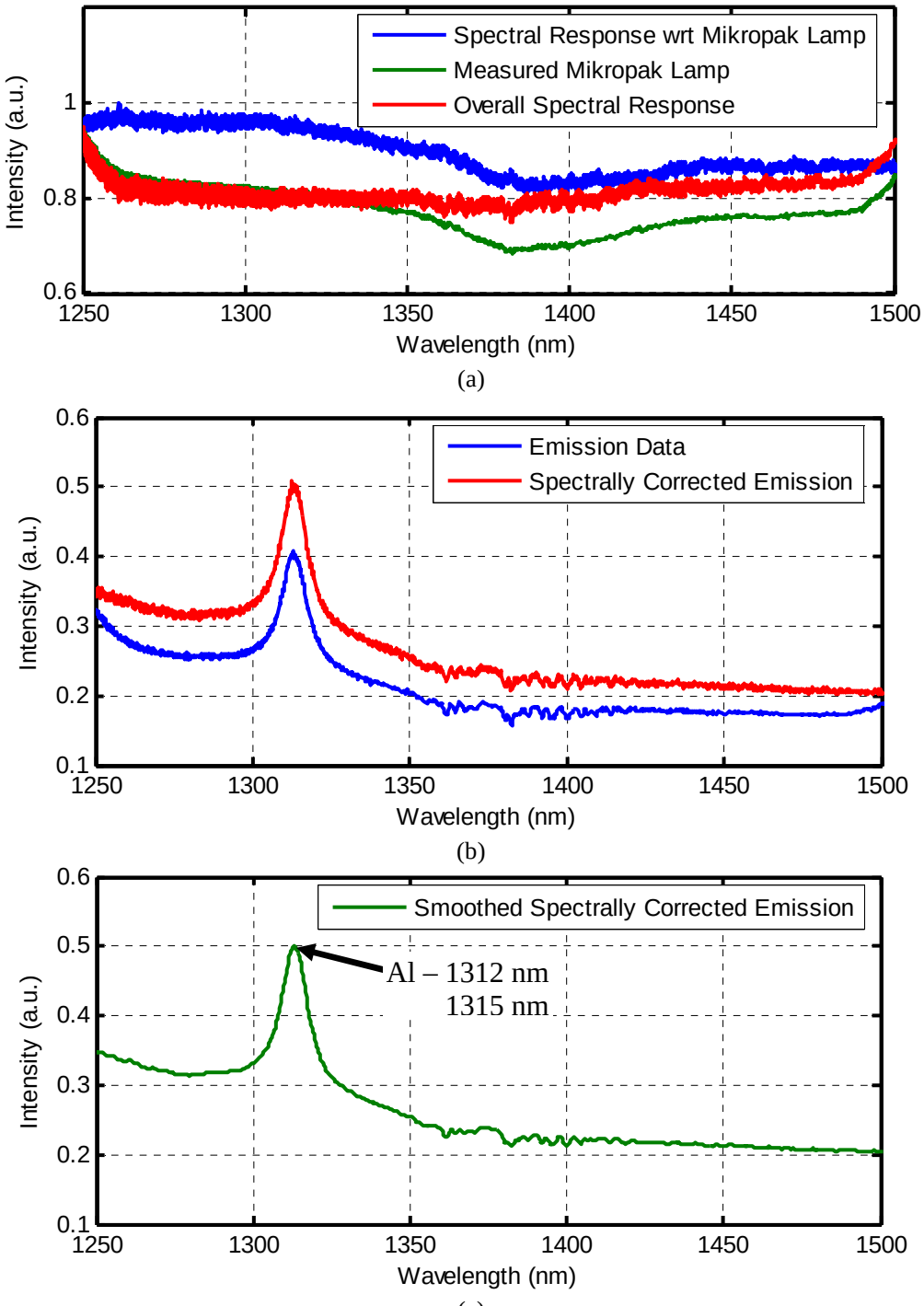

Figure 3.7 Data reduction steps for obtaining spectrally corrected smoothed emission data. (a) Spectral response with respect to the Mikropak lamp, spectrum from Mikropak lamp prior to shot, overall spectral response of system prior to shot. (b) Raw data from sample shot of SA-1 formula and spectrally corrected emission data. (c) Final, smoothed spectrally corrected emission data showing Al doublet at 1312.3nm and 1315.6nm.

The data used in Figure 3.8 was obtained in the first 55 μs after breakout from an SA-1 charge consisting of 5% Al and 5 % Ag. It should be noted that the camera collects intensity measurements in number of photoelectrons, but in the spectral response correction, this intensity is converted to units of power and that is the intensity in the final processed data plots.

Results

The fast NIR spectrograph can provide the observer with three kinds of data. First, the spectral content of the data reveals the presence of atomic and molecular species that are emitting, along with any information that can be interpreted from relative emission strengths and shapes of these discrete spectra (e.g. temperature). Second, the time-resolved spectra give an indication of how long the discretely emitting species are present. Finally, the broadband background present after the atomic and molecular signatures disappear can be used to interpret spectral pyrometry temperatures of hot particles that persist or appear during combustion. Details of these data types and sample results from the experiments conducted at the NSWC-IH will be presented in this section.

Atomic and Molecular Signatures

Structured, atomic and molecular signatures resulting from the detonation process have been measured in the uv-visible region by Carney *et al.* using high-speed streak cameras (Carney, Miller et al. 2006; Carney, Wilkinson et al. 2007; Wilkinson, Lightstone et al. 2007). In previous work done in the near-infrared region by Gross *et al.*, such highly structured atomic and molecular features were not observed due to lower

temporal resolution (Gross, Dills et al. 2003; Orson, Bagby et al. 2003). With a temporal resolution of 125 ms, Gross *et al.* were able to see broad emission resembling a Planckian distribution following the detonation of TNT explosives. Due to the higher temporal resolution of the fast NIR spectrometer developed in this work, the highly structured emission present immediately following detonation can now be observed in the NIR.

Using the PETN based explosives described in this section atomic and molecular features were observed in experiments at NSWC-IH. In order to study the effects of adding Ag and Al to the explosive formulations the emission spectra from pure PETN was first recorded from 750 nm to 1500 nm.

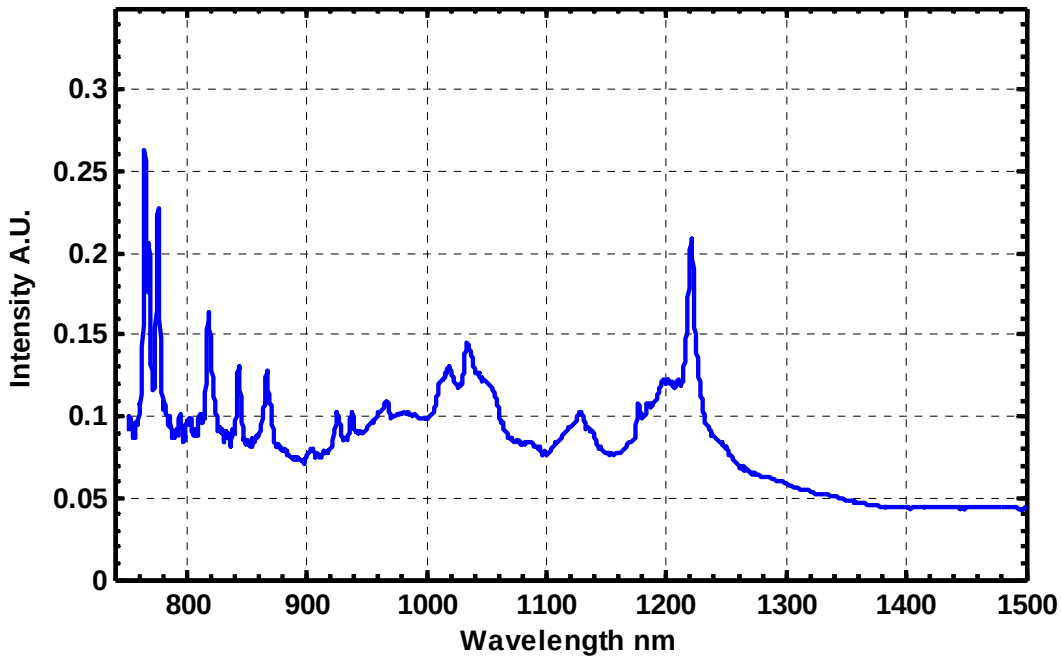

Figure 3.8 A compilation of 3 sets of pure PETN emission spectra from 750-1500 nm (250 nm each).

A compilation of 3 sets of pure PETN emission spectra from 750-1500 nm (250 nm each) is presented in Figure 3.8. Figure 3.9 shows the emission spectra collected in the first 55

μs following the detonation of pure PETN. Atomic oxygen triplets are present at 844 nm and at 777 nm that are thought to be contributed by shocked heated air in between the shock wave and detonation products. A sodium doublet (818 nm and 820 nm) and potassium doublet (766 nm and 770 nm) have also been identified and are thought to be impurities in the PETN samples.

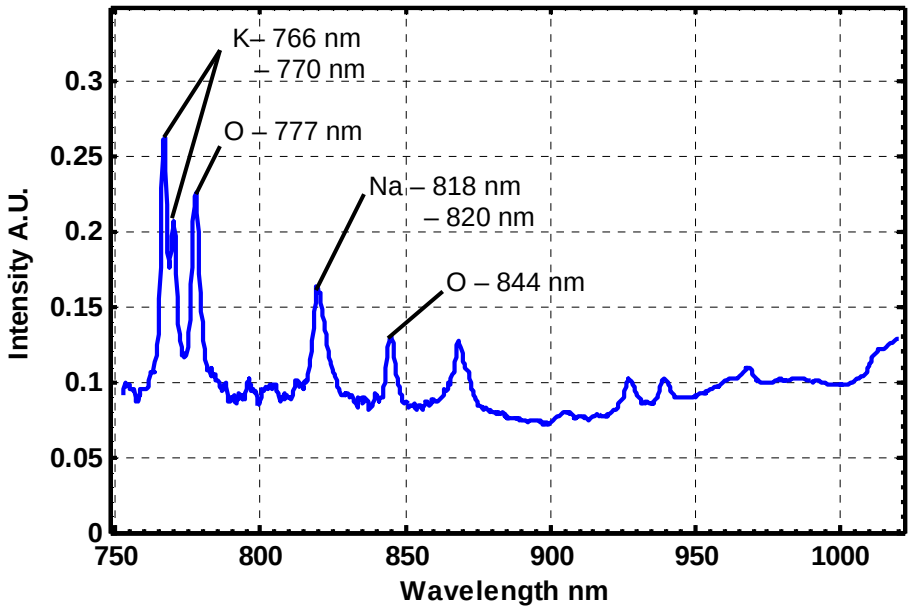

Figure 3.9 Emission spectra 750nm-1000nm in first 55 μs after detonation of pure PETN displaying a sodium doublet (818nm, 820nm), potassium doublet (766nm, 770nm) and Oxygen triplets at 844nm and 777nm.

Features beyond 850 nm were difficult to identify as the molecular signatures may be from the detonation products or from shock heated air. More definite assignments of these signals will be made with the aid of future experiments. The NIR emission spectrum of pure PETN was very repeatable and could potentially be used for the remote identification of explosive formulations as Gross *et al.* have proposed (Gross, Wayman et al. 2007). When aluminum was present, Emission from an atomic Al doublet 4S ← 4P (1312.3nm and 1315.6nm) was observed. It was also observed that when silver is present

in the formulation, an Ag line at 827.4nm was detected. The presence of these atomic Al and Ag emissions illustrates their involvement in the combustion reactions and time-resolved measurements discussed in the next section can further illuminate their participation in such events. As mentioned previously, atomic temperatures could be calculated from the spectra provided by the NIR spectrometer when strong, temperature sensitive pairs are present. Future work with the NIR spectrometer could involve the doping of explosive formulations with strong emitters in the NIR similar to the work done by Lewis and Rumchik, but measurements can now be made on faster timescales (Lewis and Rumchik 2009).

Temporal Information

As described previously, the temporal resolution of the camera can be easily adjusted to obtain adequate signal, with a maximum resolution of 21.3 μs. Immediately following break-out of the detonation, all measured spectra are highly structured due to atomic and molecular emission. This emission typically decayed within the first 40 μs following break-out. Typical time-resolved NIR emission spectra from a single experiment are presented in Figure 3.10. The intensity values have been corrected by the relative spectral response of the system and are presented on a log scale for clarity. For this experiment, the camera was set to its fastest factory setting (46,992 spectra/sec). Emission from an atomic Al doublet 4S ← 4P (1312.3 nm and 1315.6 nm) was observed and lasted less than 21 μs as shown in Figure 3.10. The NIR spectrometer is able to capture this emission, but does not capture the evolution of the feature making quantitative measurements of early atomic features difficult.

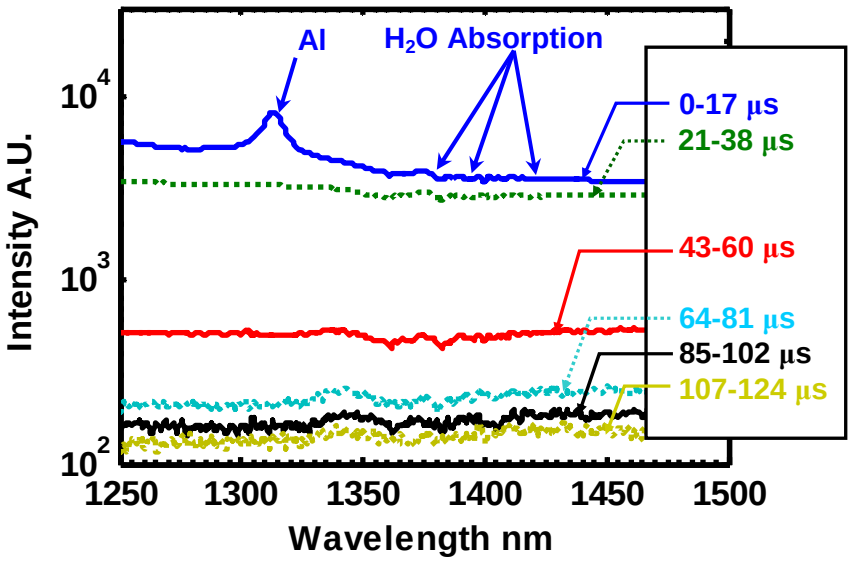

Figure 3.10 NIR time-resolved emission spectrum of PETN with 5%$AgIO_3$/5%Al. Atomic Al is observed at 1312 nm lasting for less than 21 µs. H_2O absorption features are observed around 1400 nm.

Spectrally broad emission persisted until ~400 µs after breakout (not shown in Figure 3.10). It was observed that when either Ag or Al was present, broad emission occurred for longer (~400 µs) than when pure PETN was used (~60 µs). Thus, broad emission after breakout is from silver and aluminum particles. Around 1400 nm water absorption features from cool water between the emitting species and lens were detected. These are the same water absorption lines investigated in Chapter 4. The newly developed NIR spectrometer is versatile with easily adjustable temporal resolution to capture relevant phenomena with adequate signal levels. Unfortunately, the NIR spectrometer is not fast enough to make quantitative measurements of the development of the early atomic and molecular emission; however, it is fast enough to capture this early structured emission (for the first time) and see the evolution of the broad emission. Because the timing of the camera can be easily controlled by the developed LabView DAQ program, future

experiments can be conducted using increasing integration periods as time progresses. This will increase the signal acquired at later times when the intensities are lower and changing more slowly, thus providing a better signal to noise ratio.

Spectral Pyrometry

When emission spectra exhibit broad Planckian behavior, it is possible spectral pyrometry measurements of the temperature of the emitter. Gross *et al.* and Goroshin *et al.* observed broad spectra in the near-infrared from trinitrotoluene explosions that exhibited Planckian behavior (Goroshin, L. Frost et al. 2006; Gross, Wayman et al. 2007). Such behavior was also observed in this work after initial atomic and molecular features subsided as demonstrated in Figure 3.11.

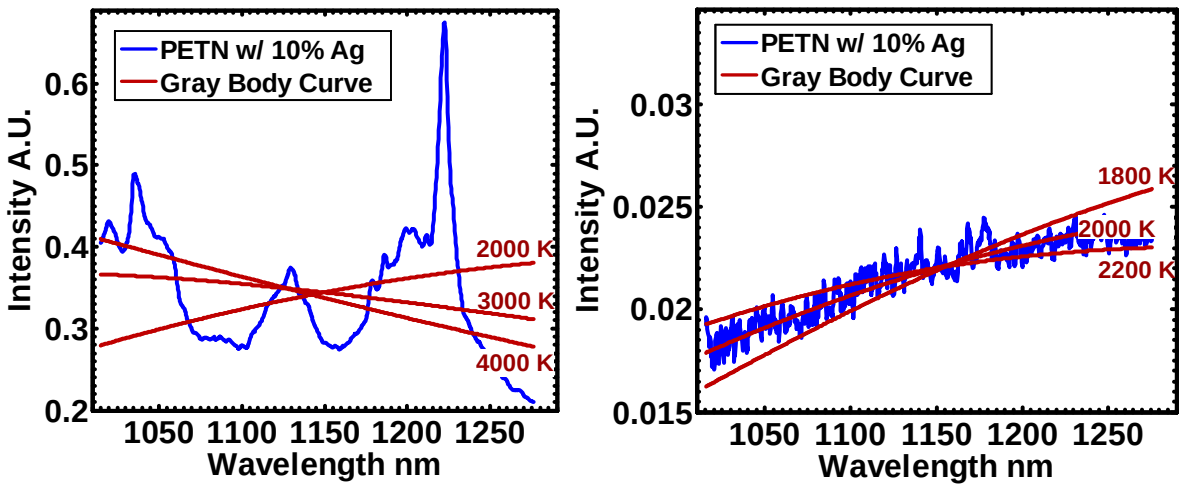

Figure 3.11 PETN with 10%Ag and lines of Planckian emission at several temperatures. (a) Shows discrete emission at breakout (0-17 μs) showing deviation from gray-body. In, (b) (43-60 μs) Planckian behavior is observed.

Using the method outlined in Chapter 2, time-resolved spectral pyrometry temperatures were determined by comparing the measured spectra from the PETN based detonations

with a Planckian distribution using a non-linear least squares fit. Spectral pyrometry temperatures at breakout (0-60 μs) were determined to be 3000K-4500K as shown in Fig. 3.12. At later times (60-350 μs) particle temperatures cooled significantly to the range of 1200K-1800K.

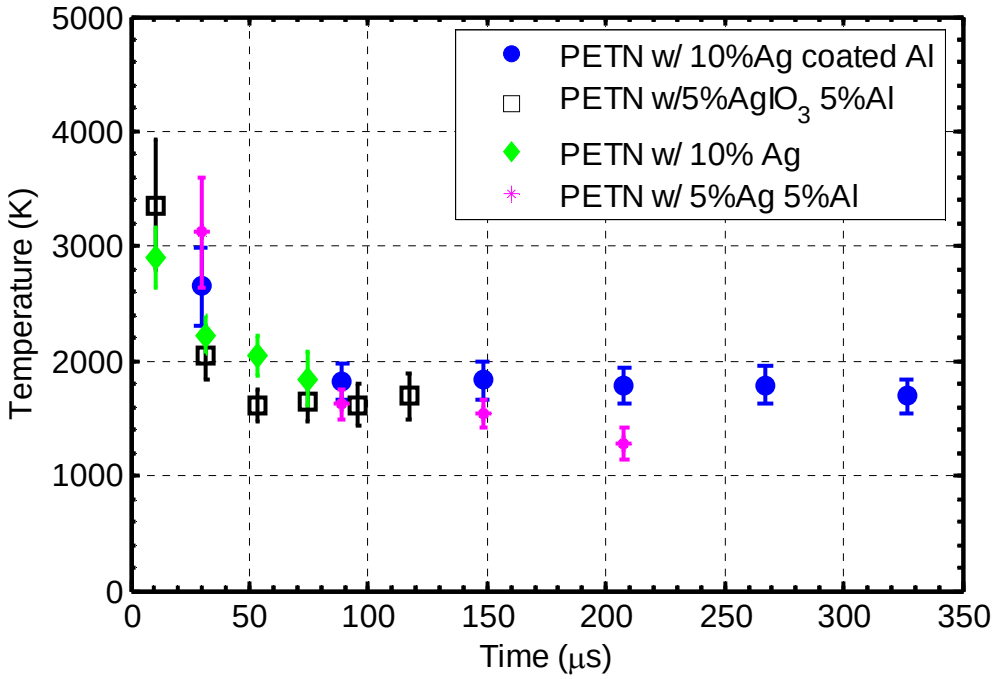

Figure 3.12 Time-resolved spectral pyrometry temperatures for various compositions.

Temperatures for pure PETN explosions are not included in figure 3.12 since early signals are dominated by atomic and molecular emission, and broad emission lasted for a very short time (21-42 μs). There is little information regarding time-resolved temperature measurements of PETN explosions in the literature to compare these temperatures with; however, they exhibit similar trends to optical pyrometry measurements of HMX and TNT by Wilkinson *et al.* and Goroshin *et al.* (Goroshin, L. Frost et al. 2006; Wilkinson, Lightstone et al. 2007). In both studies, temperatures

reached high initial temperatures then quickly stabilized within ~100 μs to nearly constant temperature for several hundreds of microseconds. As mentioned in Chapter 2, optical pyrometry (OP) is a similar method to spectral pyrometry but usually only investigates 2 or 3 narrow bands of wavelengths. Optical pyrometry measurements were simultaneously recorded in this work; however signal levels from the collection optics used were low and useable data was only recorded for short times. The results from these measurements are shown in Figure 3.13.

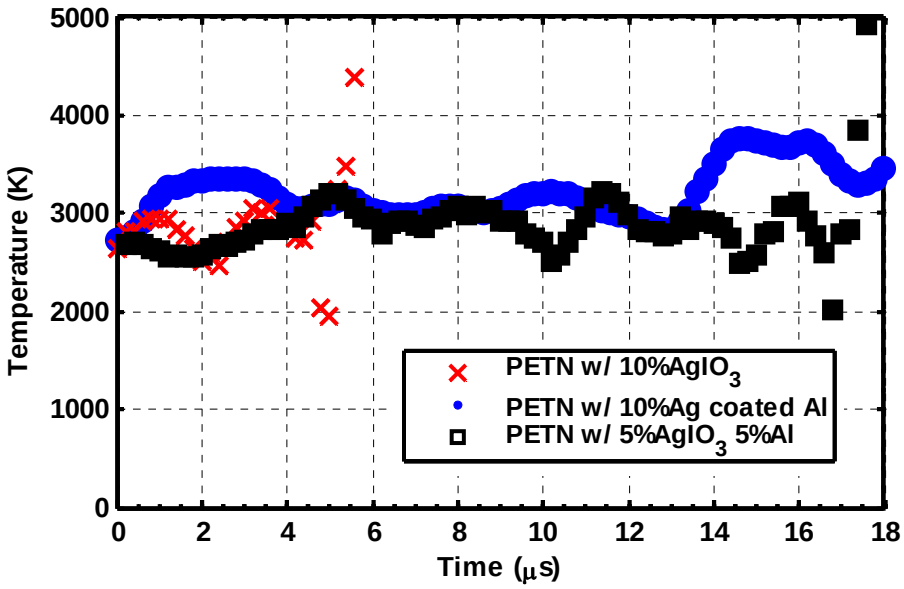

Figure 3.13 Time-resolved optical pyrometry temperatures for various compositions

Although data only persists for short times for most formulations, it shows that early temperatures tended to be around 3000 K. This is in general agreement with the spectral pyrometry data; however future experiments using better optical pyrometry collection optics and more sensitive detectors would prove useful in verifying the extent of agreement between the two methods. For the experiment involving formula SA-2 (PETN

w/5%-$AgIO_3$ 5%-Al) OP measurements were obtained for longer times and a comparison to the spectral pyrometry data for the same shot is shown in Figure 3.14.

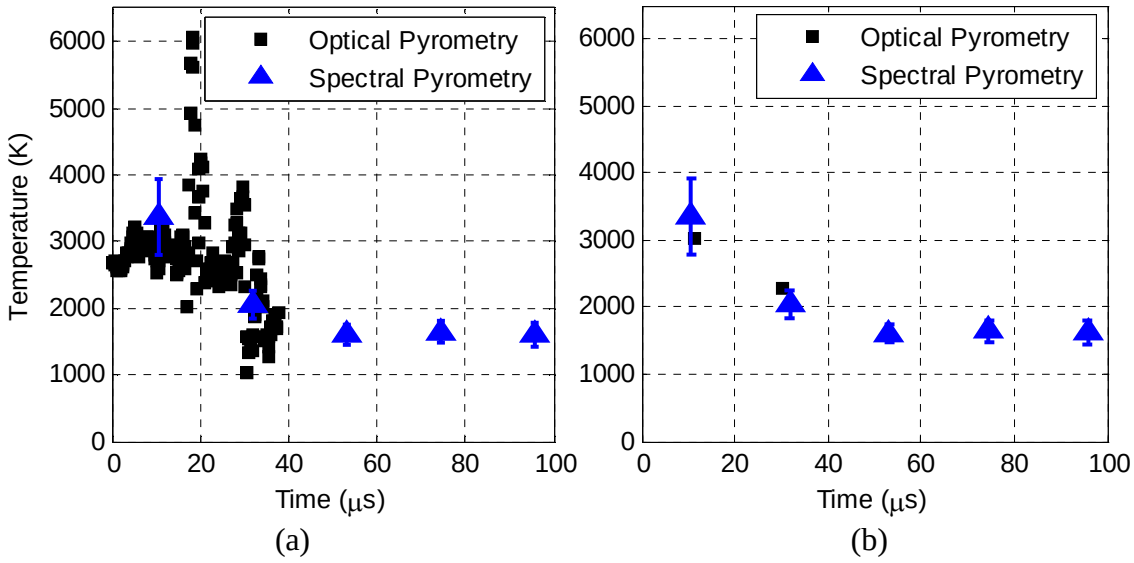

Figure 3.14 Time-resolved optical and spectral pyrometry temperatures for SA-2 formulation. (a) complete data from OP and spectral pyrometry. (b) window averaged OP temps and complete spectral pyrometry temperatures.

Figure 3.14 (a) displays the complete data from the optical and spectral pyrometry techniques. Figure 3.14 (b) shows window averaged OP temperatures with corresponding spectral pyrometry temperatures. The OP temperatures show fair agreement with the spectral pyrometry temperatures and fall within the uncertainty of the measuremnents as discussed in the following section.

Error Analysis

As mentioned in Chapter 2, error in spectral pyrometry measurements is primarily due to two factors: uncertainty in the experimental spectra, and systematic errors due to

greatly varying emissivity. To estimate the uncertainty in the fit of the spectra, the 95% confidence intervals on the nonlinear least squares fit were determined for the temperature estimates. The estimated error in temperature due to the uncertainty of the nonlinear least squares fit was found to be low (~1-2%) for temperatures determined after initial structured breakout, and much higher (~5% or greater) for temperatures determined from initial highly structured emission at breakout. It is clear that the initial, highly structured emission deviates greatly from Planckian emission and temperatures determined from the entire emission signature will be of high uncertainty. It is noted that within the highly structured initial spectra there are regions that appear to follow Planckian emission as shown in Figure 3.15.

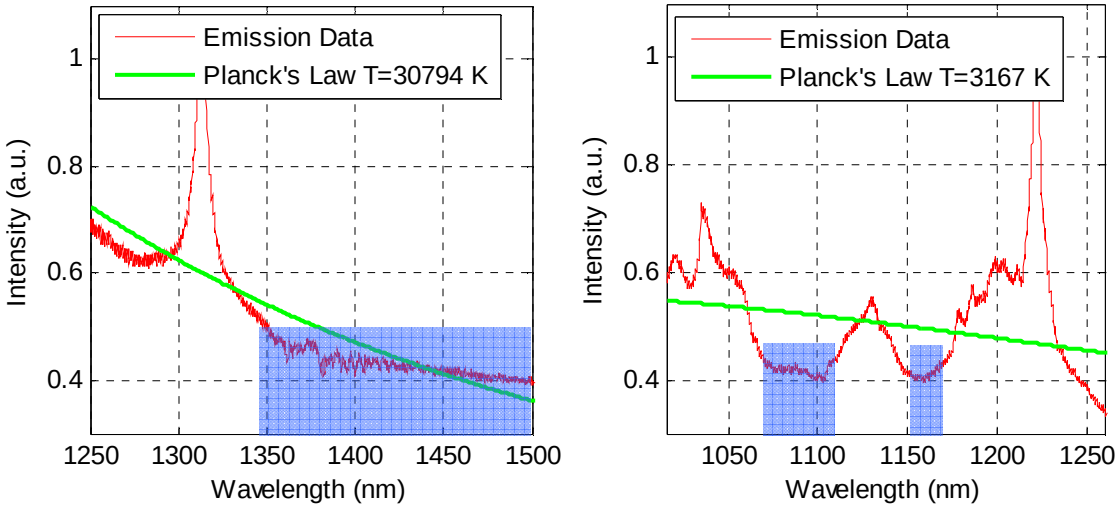

Figure 3.15 Emission from first 17 μs after detonation showing highly structured spectra with some regions of broad Planckian emission highlighted in blue. (a) Formula SA-2 (5% $AgIO_3$ /5% Al) best fit temperature of T=30794 K. (b) Formula S-1 (10% Ag) and best fit temperature of T=3167 K.

The temperature determined from Figure 3.15 (a) (T=30,794 K) seems very high compared to all other measurements and carries a high uncertainty of fit (~90%) due to

the strong atomic signature. The temperature from Figure 3.15 (b) has an uncertainty of fit of ~6%. To determine temperatures with lower uncertainty from such structured data, the spectral pyrometry method can be performed only on the areas that exhibit broad emission and do not have highly structured features. Such regions are highlighted in Figure 3.15 in blue. Temperatures were determined using only the highlighted regions and much lower uncertainties (~1-3%) were obtained for initial, structured spectra. Figure 3.16 shows the Planckian emission fit only to the regions highlighted in blue in Figure 3.15. The best fit temperature determined from Figure 3.16 (a) was T=3360 K with a much lower uncertainty of ~3%. The emission from the highlighted regions in Figure 3.16 (b) had a best fit temperature of T=2895 K with an uncertainty of ~2%.

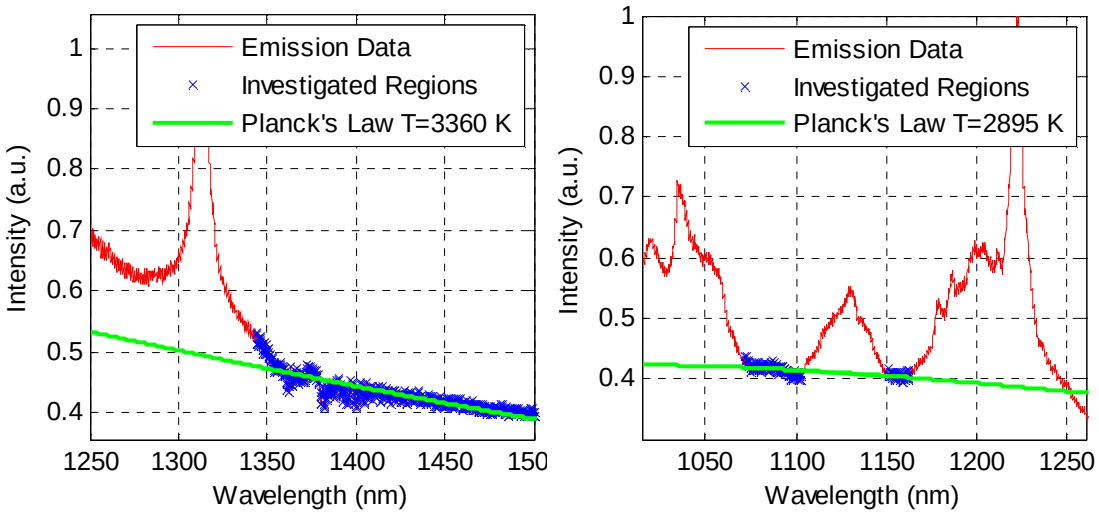

Figure 3.16 Emission from first 17 μs after light breakout. Temperatures were determined only from regions of broad Planckian emission highlighted in blue. (a) Formula SA-2 (5% $AgIO_3$ /5% Al) best fit temp. of T=3360 K. (b) Formula S-1 (10% Ag) and best fit temp. of T=2895 K.

Using these methods, the uncertainty for the fit of the temperatures in general was found to be ~1-3%. This uncertainty from these measurements is a propagation of the

noise present in the data. This value of uncertainty is itself only a partial measure of the precision of the method and does not represent the total error present. The broad emission from which the temperatures were calculated was very weak and exhibited a low signal to noise ratio (<5 at later times). The effect of background subtraction on these low signal levels proved to significantly change the temperature that was determined by the spectra. To estimate a level of error introduced by the background subtraction, temperatures were determined with two standard deviations of the background added to the emission data and with two standard deviations subtracted from the data. The error estimates from this method are lower (~1-2%) at earlier times (<100 μs) for spectra with higher signal levels and higher (~2-10%) at later times (>100 μs) from spectra with lower signal levels.

Systematic errors in the method are primarily due to the gray-body assumption since, for most metals, the emissivity is noticeably a function of wavelength. For example, the emissivity of tungsten at T=2000 K changes almost linearly by ≥20% in the range of λ = 500-1000 nm (Magunov 2009). Despite this, Magunov found that errors for temperatures of metals, in which the emissivity was assumed constant, are only on the order of several percent (~2-5%). To estimate the error associated with the gray-body assumption, a linear emissivity model was incorporated into the spectral correction of the data that varied the emissivity by a linear decrease of 10% over the range of spectra (250 nm). After this correction, temperatures were determined by the same method. A sample spectrum and best fit temperatures is plotted in Figure 3.17. The data in Figure 3.17 was taken from 43-64 μs after breakout from detonation of a charge of formula S-1 (10%Ag). The emission data is plotted in blue and Planckian emission at its best fit temperature

(T=2047 K) is the red line. The emission was corrected for a linear decrease of emissivity of 10% over 1000-1250nm and is plotted in green along with planckian emission at its best fit temperature of T=2212 K (black line). Determined temperatures varied by ~8-15% when non-constant emissivity was introduced suggesting a systematic error in the system of the same order.

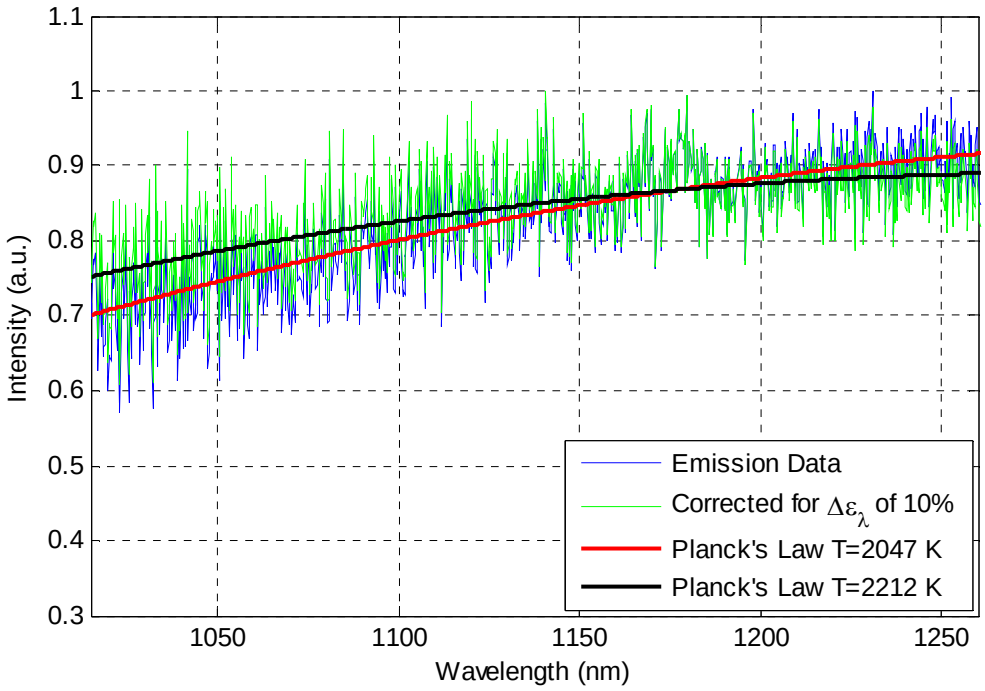

Figure 3.17 Emission from 43-64 μs after breakout μs after detonation of S-1 charge (10%Ag) demonstrating effect of incorporating varying emissivity on temperature determination.

Further information on the emissivity of aluminum and silver at the temperatures present in post-detonation combustion could help better quantify the systematic error due to varying emissivity present in this work.

To incorporate the uncertainty estimates and systematic errors presented here into a total uncertainty estimate, the root sum squared uncertainty *(u_T)* was calculated from Equation 3.2.

$$u_T = \sqrt{u_{fit}^{\ 2} + u_{BG}^{\ 2} + u_{emissivity}^{\ 2}} \quad (3.1)$$

Where u_{fit} is the uncertainty of the fit u_{BG} is the uncertainty associated with the background subtraction and $u_{emissivity}$ is the uncertainty related to varying emissity. Root sum squared uncertainties for the data were ~9-18%. This is the uncertainty that is plotted as error bars in the previous figures. It is noted that the largest source of uncertainty is attributed to the unknown variation of emissivity and efforts to reduce this uncertainty could significantly improve the quality of the results.

With higher loadings of particles brighter intensity borad emission is expected which would produce higher overall signal to noise ratio and reduce the uncertainty due to the background subtraction. Also, a better model for the emissivity of the silver and aluminum particles can reduce the uncertainty related to varying emissivity. Spectral pyrometry temperatures made by this spectrometer show promise in supplementing existing techniques used in detonation science.

Summary

Previous temporally and spectrally resolved measurements of detonation events have been limited to probing the ultra-violet and visible regions. In this section the development of a novel, fast, near-infrared spectrometer utilizing a fast InGaAs array for use in harsh (explosive) environments is described. Spectrally and temporally resolved NIR emission measurements were obtained from observing post-detonation combustion of silver- and aluminum- doped pentrite (PETN) charges using the spectrometer. Atomic NIR spectral features were identified and found to last less than ~40 μs. As a reference,

baseline spectra of pure PETN were recorded over 750-1500 nm. When silver or aluminum particles were present, broad Planckian emission was observed following the discrete spectra and lasted for several hundred microseconds. Spectral pyrometry temperature measurements were determined from the spectra temperatures at breakout (0-60 μs) were determined to be 3000K-4500K. At later times (60-350 μs) particle temperatures cooled significantly to the range of 1200K-1800K. A comparison to limited optical pyrometry data suggests fair agreement. Better signal levels in future experiments could be achieved with heavier doping of particles and more sensitive optical pyrometry equipment. The basic characteristics of the newly developed fast NIR spectrometer are investigated in this work and the spectrometer has demonstrated its usefulness as a tool for use in explosives research extending the range of temporally and spectrally resolved measurements.

Chapter 4:
Feasibility Study of NIR H_2O Absorption Method for In-Situ Measurements of T and X_{H2O} for Examining Post-Detonation Combustion of PETN Based Explosives

Introduction

As discussed previously, fast in-situ measurements of key properties including temperature and species concentration during detonation reactions are difficult to obtain due to the harsh environment and short timescales. Absorption spectroscopy is an appealing method for use in explosives experiments as temporally resolved spectra can be analyzed to produce such measurements. As discussed in chapters 1 and 2, a NIR H_2O absorption method has been developed by Kranendonk *et al.* to measure properties in combustion environments (Kranendonk, Caswell et al. 2007). In this chapter, the feasibility of applying this NIR H_2O absorption method to arena-type explosives experiments using the newly developed NIR spectrometer is examined. A system for making such measurements was constructed and the characteristics of the system are

discussed along with major challenges associated with detonation environments and potential solutions.

Bench-top experiments were also conducted at Marquette University in order to demonstrate the capabilities of the system and optimize the system for eventual use in detonation environments. The findings of these experiments and sample results will be presented here. Finally, details on the creation of a database of relevant H_2O absorption spectra and an advanced data reduction scheme will be discussed.

Experimental Setup

This section will describe the setup of a NIR H_2O absorption spectrometer for use in studying post-detonation combustion of high explosives at the Naval Surface Warfare Center in Indian Head, MD. Bench-top measurements of water cells in a furnace were also performed at Marquette University and the scheme used will be presented here.

Naval Surface Warfare Center, Indian Head Facilities

Experiments were carried out at the Sigmund J. Jacobs Detonation Science Facility at the Naval Surface Warfare Center, Indian Head division in a manner similar to the previous emission experiments. Pure PETN charges were chosen for their optical clarity allowing the use of long path lengths with minimal extinction. The test setup within the bombproof chamber is shown in Figure 4.1. A one-inch charge of PETN is placed 12” from the absorption gauge which is bolted to an optical table resting on plywood over a steel cylinder. The charge assembly consisted of an RP-80 exploding bridgewire detonator, followed by a Detasheet booster (25 mm diameter x 6 mm thick),

and the main charge (1 in diameter x 1 in thick). To fire the charges, a 500 V pulse generator was used and timing was controlled by the LabView based DAQ system described in this section. It was found that first light emerged from the charge approximately 8 μs following the detonator trigger pulse, and the delays for each instrument were adjusted accordingly.

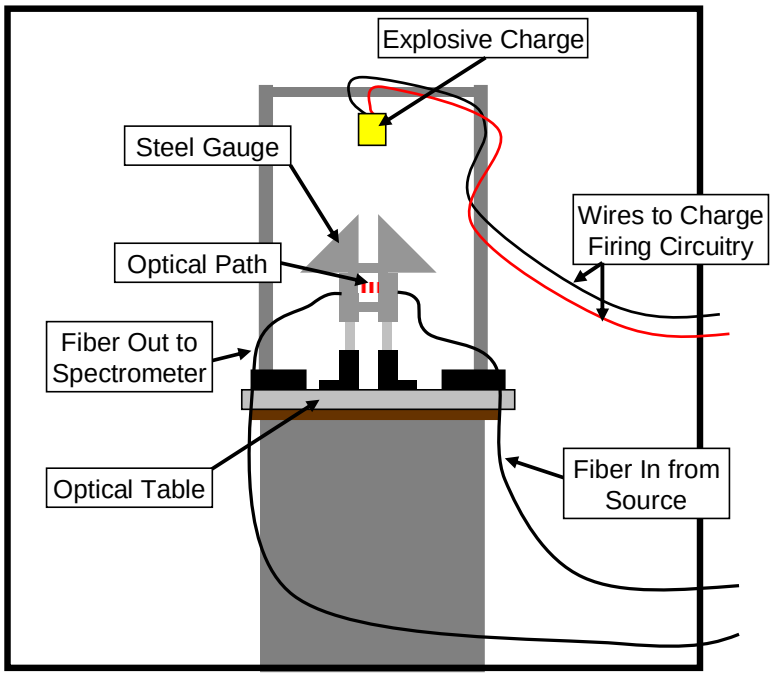

Figure 4.1 Overall layout of absorption experiments in bombproof chamber. A one inch pure PETN charge is hung 12" above the absorption gauge bolted to an optical table.

A high-speed camera was also used in initial experiments to verify the timing of the arrival of the shock front to the absorption gauge.

NIR Absorption Spectrometer

To record absorption spectra, the following major elements are required: a light source, absorbing medium, and a detector capable of making spectrally resolved

measurements. Kranendonk *et al.* achieved this by using an FDML laser which temporally separates the wavelength, transmitting the light through the cylinder of an optically accessible combustion engine and then detecting the light with a fast photodiode (Kranendonk, An et al. 2007). The use of an alternate source of NIR light was sought in this work to reduce the complexity of the system and to facilitate the use of the newly developed NIR spectrometer.

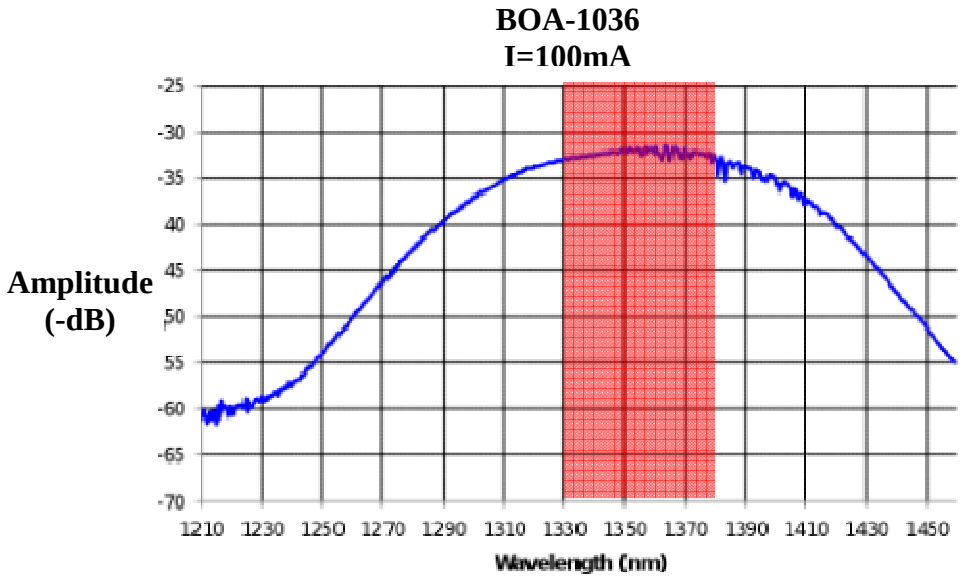

Figure 4.2. Amplitude (-dB) vs. wavelength (nm) plot of Covega BOA 1036 used as the source in the NIR absorption spectrometer and covering the R-branch of the $\nu_1+\nu_3$ band of H_2O (1330-1380 nm) shown in red.

As discussed in Chapter 2, the R-branch of the $\nu_1+\nu_3$ band of H_2O (1330-1380 nm) is an attractive region for use in determining temperature and mole fraction of water from measured spectra. Thus, a source is sought that covers this entire region. A Booster Optical Amplifier (Covega BOA 1036) was chosen as the NIR source as it was capable of generating up to 3 mW of infrared light in the 1310-1390 region. This allowed for observation of the desired wavelengths with a simple, fiber-coupled, broad source. A gain vs. wavelength plot for the BOA is shown in Figure 4.2. One end of the BOA was

coupled to a fiber mirror to improve optical output. The BOA was controlled by a diode laser driver board (Micro Laser Systems DBDL2000T/S) and cooled by a thermo-electric cooler (Inphenix IPEVM1010).

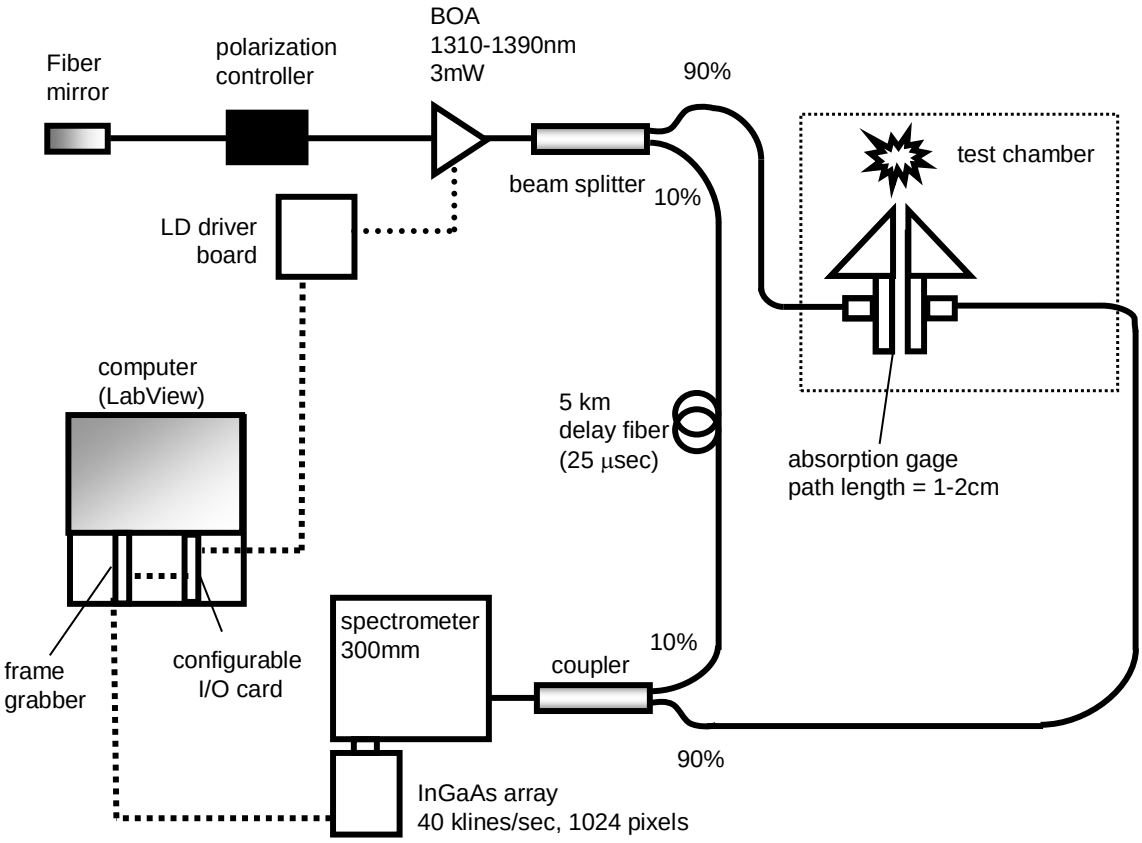

Figure 4.3 Layout of NIR H_2O absorption spectrometer. The light source is coupled to a fiber mirror on one end and a fiber coupled beam splitter on the other. The splitter sends 90% of the light to the blast chamber where it is pitched over a short path length (1-2 cm) then focused onto another fiber which carries it out of the chamber. The other 10% goes through a delay line and then both signals are sent to the spectrometer by a second coupler. A Labview based DAQ program controls the entire system.

Figure 4.3 depicts the layout of the NIR H_2O absorption spectrometer. The driver board is triggered by a LabView based computer data-acquisition system. To achieve highly controlled data acquisition at speeds up to 40 kHz, a field-programmable gate array (FPGA) card was used. This card is easily reconfigurable and allowed for precisely

controlled timing at high speeds to be executed with the data acquisition system. This was advantageous when adjusting the timing for the delay line and optimizing the duty cycle of the source. It is known that some of the components including the BOA and diffraction gratings are polarization sensitive and a polarization controller is placed in between the BOA and the fiber mirror to provide some control over the effects of the dependencies.

$$T_\nu = \left(\frac{I}{I_o} \right)_\nu = \exp\left(-k_\nu L\right) \quad (4.1)$$

Beer's Law (Equation 4.1) states that absorbance ($k_\nu L$) can be determined from the ratio of the transmitted intensity (I) to the initial intensity (I_o). To measure the initial intensity, the light from the BOA is sent to a beam splitter which sends 10% of the signal through a 5 km delay line (I_o) and 90% of the signal to the blast chamber (I). The delay line temporally separates the two signals and allows a single detector to record both signals. This removes the problems associated with comparing signals from two detectors such as bias and differing spectral responses. Although there will still be some differences in spectral response between the reference and transmitted signals due to the fibers and lenses used, these will be shown to be small and have little affect on the final temperature measurements due to the data reduction scheme. To calculate the length of delay line necessary to acquire absorption spectra at 20 kHz, Equation 4.2 was used.

$$d = \frac{c}{n} \cdot \frac{1}{f} \quad (4.2)$$

The required distance d [m] is determined from the speed of light c [m/s], the refractive index of the fiber n, and the frequency at which the camera is operating f [Hz]. To acquire absorption spectra at 20 kHz, the camera must operate at 40 kHz to record both a transmitted signal I and a reference signal I_o every 50 μs. At this speed, a delay line of 5 km is necessary.

The other 90% of the light from the BOA is sent to the blast chamber via a 9 μm diameter, 15 m long, single-mode fiber optic patch cable (Corning SMF-28e). The fiber attaches to a steel gauge where the light is then collimated with ½" diameter, 25 mm focal length lens as shown in Figure 4.4.

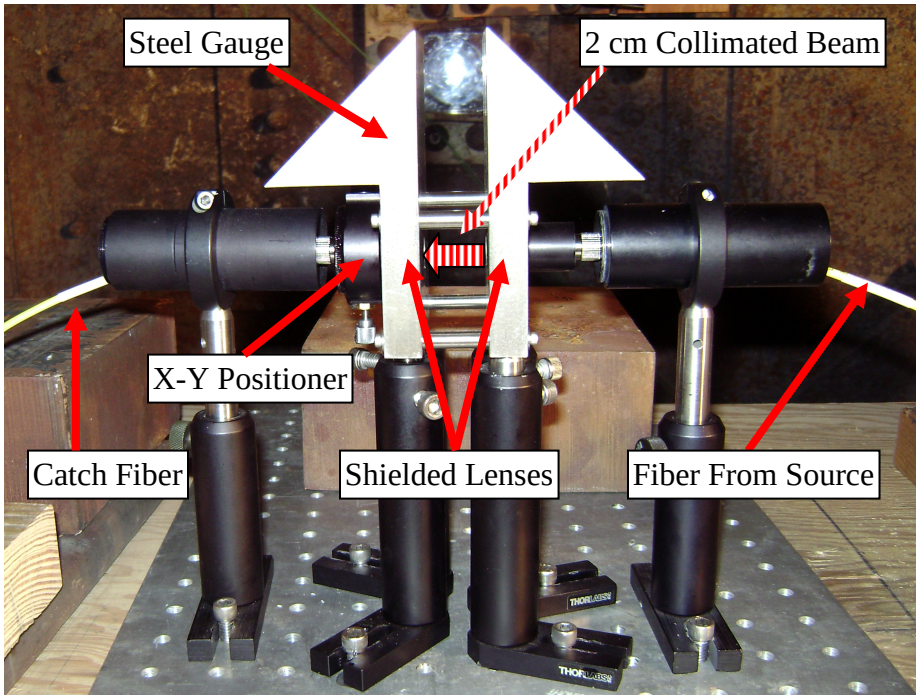

Figure 4.4 Steel absorption gauge in blast proof chamber with input and output fibers, x-y positioner, and 2 cm path length.

The collimated light was sent over a path length of 2 cm where it was then focused onto the catch fiber using a second ½" diameter, 25 mm focal length lens. Due to mode noise, which will be discussed later in this section, a single-mode fiber was chosen. To couple

light into a single-mode, 9 μm diameter fiber, precise control over the fiber's position is needed and an x-y positioner (Thorlabs LM05XY) was used to align the fiber with the focusing lens. In attempt to minimize the effects of beam steering and absorption gauge vibrations, the catch fiber was positioned slightly further from the lens than the focal point. Although this reduced the amount of light entering the fiber, this allowed for coupling of the light even with slight translation of the beam with respect to the focusing lens.

The light was then transmitted out of the blast chamber and coupled with the delay line before entering the spectrometer. The slit on the spectrometer was opened to a maximum of 600 μm allowing light from the entire fiber to enter the spectrometer. Thus, the 10 micron fiber determined the resolution obtainable for the spectra. A 1000 g/mm grating blazed at 1.3 μm was used in the spectrometer to provide a spectral resolution of 0.093 nm and a range of ~45 nm. The camera was set at its highest sensitivity to allow faster operation and its timing was controlled by the LabView program.

The timing diagram in Figure 4.5 details the operation of the camera and light source. The entire process is triggered by the charge firing circuitry which sends signals to the DAQ program. To quantify the background level and noise before the shot, several background images are taken before the detonation is triggered. Also, several absorption spectra are recorded at ambient conditions before the detonation event to ensure proper system operation and to determine when the system has returned to pre-detonation conditions.

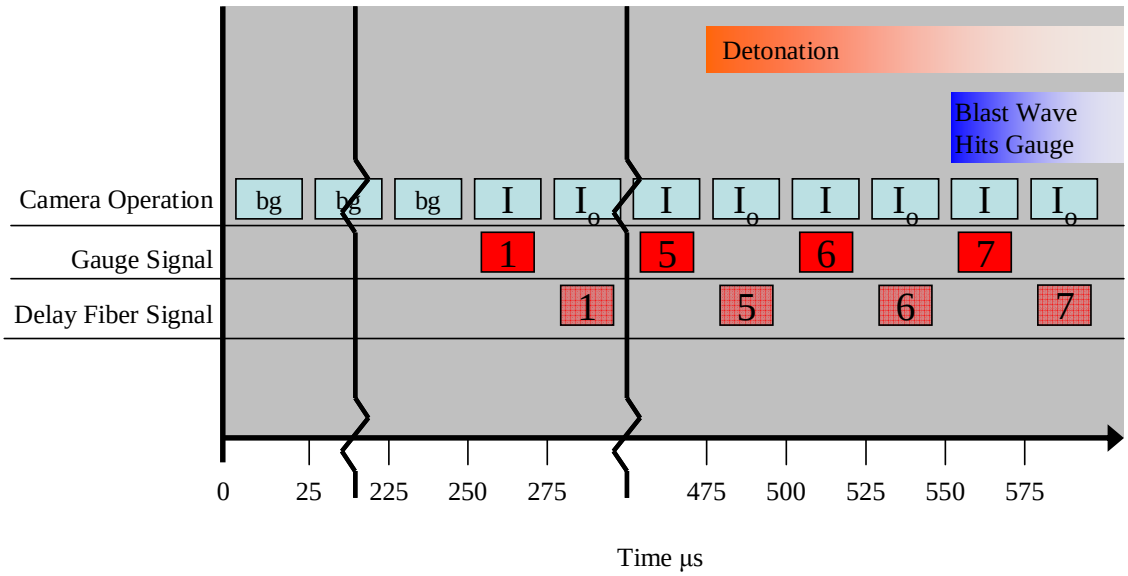

Figure 4.5 Timing diagram of NIR H_2O absorption spectrometer.

As shown in Figure 4.5, for each light pulse, two spectra are recorded: the transmitted signal *I* and the reference delay fiber signal I_o. The duty cycle of the camera is maximized to record as long as possible at 40 kHz and was set to record for 84% of each 25 µs window. The duty cycle of the light source was optimized to match the duty cycle of the camera and prevent multiple signals (i.e. both *I* and I_o) from being recorded in a single frame and was set at 35%.

Data Reduction Procedure

The spectrometer is calibrated by comparing a measured spectrum at room temperature and pressure with a simulated spectrum at the same conditions. The data reduction procedure to determine temperatures and mol fraction H_2O used in this work follows the method discussed in Chapter 2, developed by Kranendonk *et al* (Kranendonk, Caswell et al. 2007). The simulation of a spectral database and details of the temperature determination method will be discussed in this section.

A high accuracy database of H_2O absorption spectra is needed at relevant conditions. To create such a database, the BT2 water line list is used. Barber *et al.* have created a highly-accurate list of H_2O infrared transition frequencies and intensities, which is the most complete water line list in existence (Barber, Tennyson et al. 2006). From the line list, a database of spectra is created for T=250-3500 K in increments of 50 K at each pressure of 1 to 35 atm in increments of 1 atm. The lineshapes in the spectra were modeled using a voigt profile incorporating both Doppler and collisional broadening as described in Chapter 2. A step by step procedure of the database creation can be found in Appendix A.

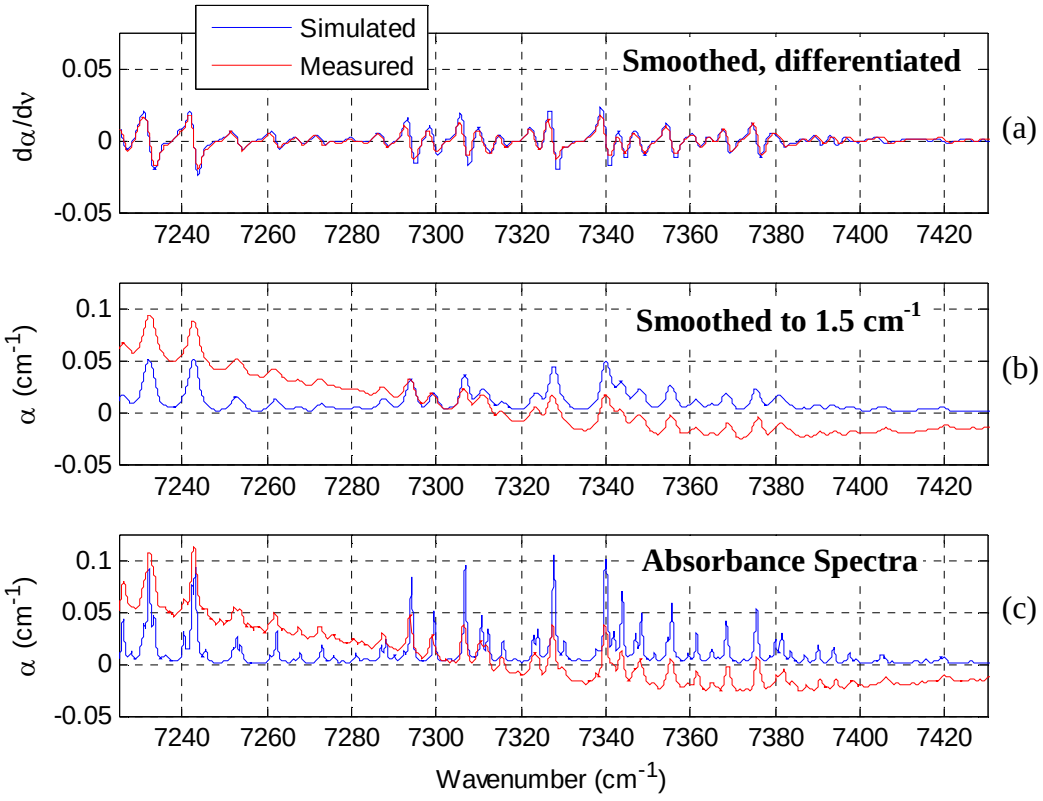

Figure 4.6 Steps to prepare simulated (blue) and measured (red) spectra for comparison. (c) Actual absorption spectrum α (cm^{-1}) vs. ν (cm^{-1}). (b) Spectra smoothed to 1.5 (cm^{-1}). (a) Smoothed, differentiated spectra.

As discussed in Chapter 2, the method for determining temperature involves interpolating, smoothing, and differentiating the measured and simulated spectra. Figure 4.6 demonstrates the steps in preparing the spectra for comparison. After processing, plots of the measured spectra vs. each simulated spectra at the measured temperature are made. A line is fit through each plot using a linear least-squares error method. The slope of the line and the mean-squared error (MSE) are saved for each plot. The mean-squared error vs. simulated temperature is plotted and the minimum MSE and corresponding temperature are interpolated from the data as shown in Figure 4.7. Mole fraction H_2O can be determined by plotting the slope of the best fit lines versus temperature and interpolating the slope at the calculated temperature.

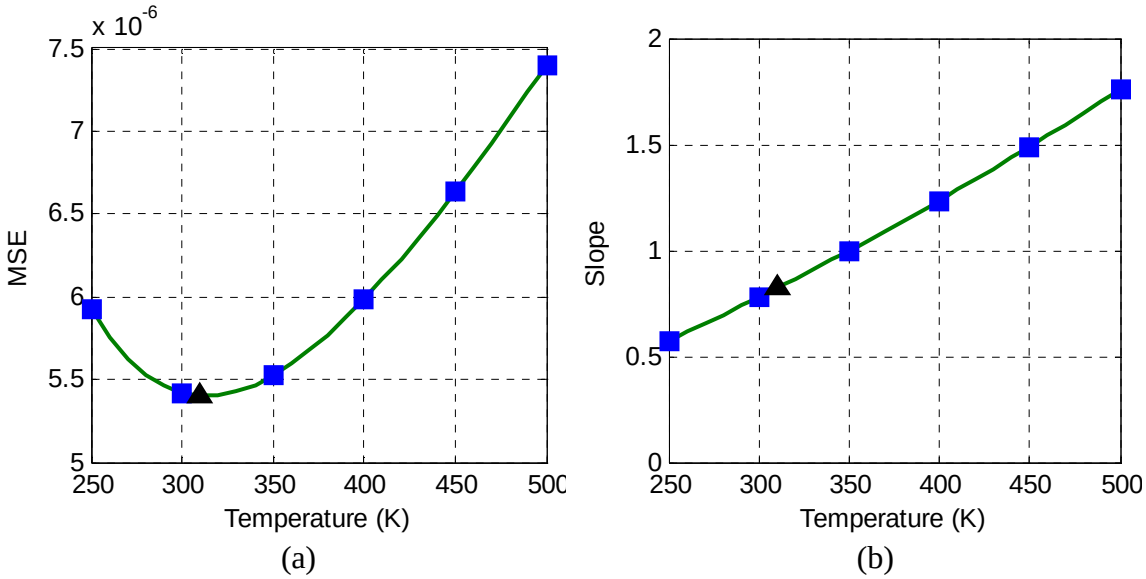

Figure 4.7 (a) MSE vs. simulated temperatures from data in Figure 4.6. Blue squares are calculated from spectra in the database. Black triangle is the predicted MSE of the measured spectrum. (b) Slopes of the best-fit lines from data in Figure 4.6 vs. corresponding simulated temperatures. Blue squares are calculated from spectra in the database. Black triangle is the predicted slope for the best-fit line of the measured spectrum.

Since the mol fraction of the simulated spectra is known, the interpolated slope can be used as a scaling factor to determine the mol fraction H_2O of the measured spectra. This procedure has been used to successfully determine H_2O temperatures and mol fractions in a furnace cell setup as described in this section. The Matlab program created to perform this procedure can be found in Appendix B.

Furnace Setup at Marquette University

In order to demonstrate the systems capabilities, bench-top experiments were performed using a small furnace at Marquette University. The absorption spectrometer was setup in a similar manner to the setup at the NSWC-IH. The furnace was T-shaped with electrical resistance heating elements. As shown in Figure 4.8, the light was sent to the furnace via fiber-optic cables where it was collimated by a ½" diameter 12.5 mm focal length lens. The light then passed through the cell containing H_2O vapor and was then focused by a ½" diameter 12.5 mm focal length lens onto a second fiber. The collection fiber was adjusted with an x-y-z translation stage to facilitate maximum coupling. An electronic control unit was used that regulated the current delivered to the heating elements. A temperature was specified on the control unit and the heating elements were automatically adjusted until the set temperature was measured by a thermocouple placed near the center of the water cell. Two different size water cells were used in the furnace experiments with path lengths of 2.5 cm and 10 cm. The water cells were ½" diameter T-shaped quartz tubes with a single opening at the end of the longer section. The open end of the cell was stuffed tightly with silica insulation that slowly allowed water vapor to leak out of the tube as the vapor expanded in the chamber.

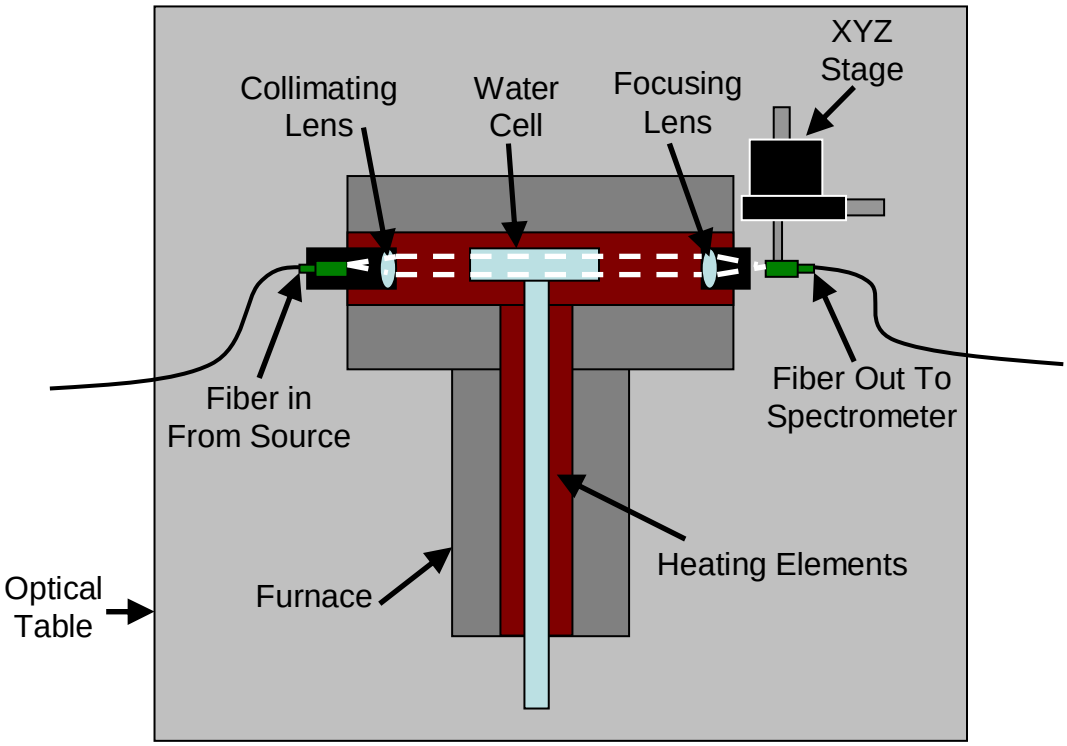

Figure 4.8. Furnace setup for bench-top H_2O absorption measurements. Light was sent from the NIR source to a collimating lens where it entered the furnace. Light then passed through a water cell and into a focusing lens where it was coupled into a second fiber optic cable.

To maximize the amount of water vapor in the cell, it was initially filled entirely with water. The furnace was then heated to 400 K and held at the temperature just until the water completely evaporated. Then the temperature of the furnace was elevated in 100 K increments and measurements were taken to a maximum of 900 K (limited by furnace). Results from experiments using the furnace at Marquette University will be discussed in this section.

Results

In this section, results obtained from two sets of experiments will be discussed: (1) results from initial experiments in the bomb-proof chamber at the Naval Surface

Warfare Center at Indian Head, MD will be presented; and (2) results from experiments to characterize the systems capabilities conducted at Marquette University will be discussed.

Blast Chamber Experiments (NSWC-IH)

The experimental challenges of performing absorption spectroscopy in detonation environments (presented in Table 1.3) are difficult to overcome. In order to obtain sufficient resolution in the spectrometer and reduce mode noise, a 9 μm single-mode fiber is used. Coupling light into a single mode fiber is difficult and the strong forces created during an explosion can easily vibrate optical components enough to move the fibers out of alignment.

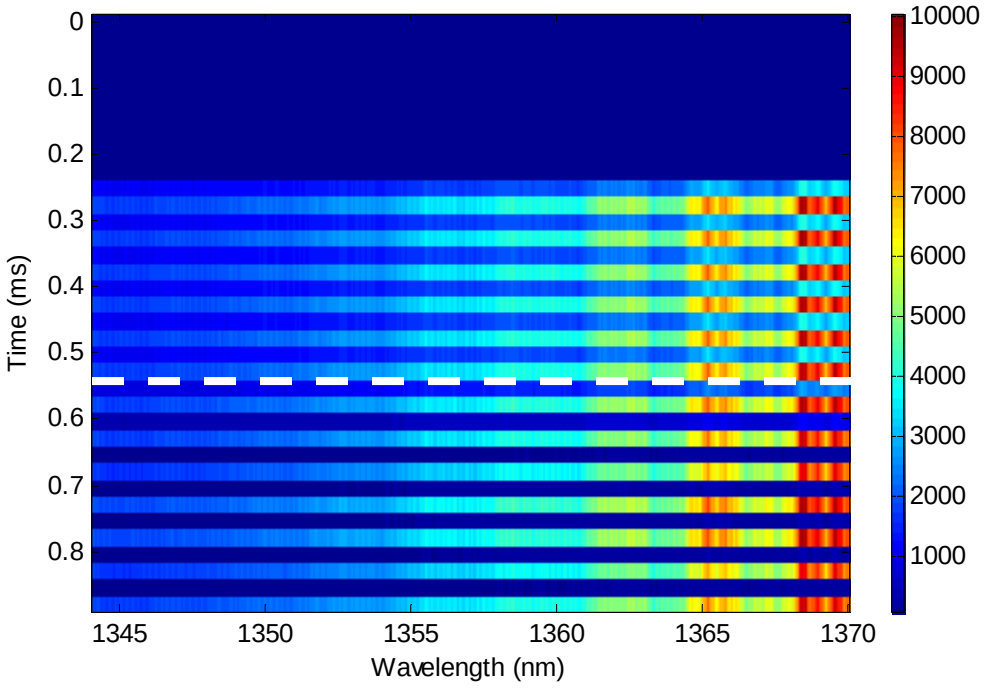

Figure 4.9 Sample results from initial H_2O absorption experiments at NSWC-IH. The initial blue region is 10 frames of background then frames alternate between transmission I and reference I_o signals. The white dashed line identifies the arrival of the blast wave at the gauge, after which, the transmission signal does not return.

This proved to be a major challenge in initial experiments at the NSWC-IH involving 1" PETN charges. Short path lengths were chosen in initial experiments (2 cm) to minimize beamsteering and vibration effects; however, the force of the shockwave impacting the gauge proved to be powerful enough to force the fibers just out of alignment. This is demonstrated in Figure 4.9. The white dotted line identifies the arrival of the shock front at the absorption gauge (~600 μs) and was verified by correlating the spectra with images from the high-speed camera. Figure 4.10 is an image from the high-speed camera showing the shock front as it contacts the absorption gauge.

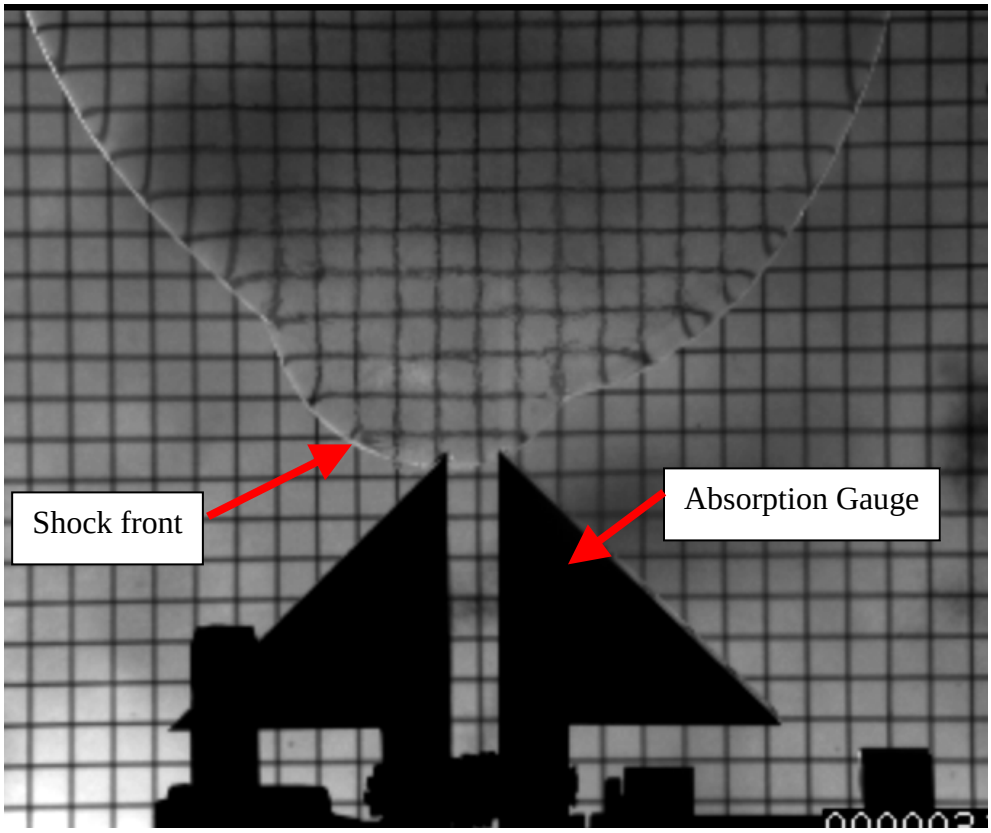

Figure 4.10 Image from high speed camera of 1" PETN detonation. The leading edge of the shock front has just reached the absorption gauge.

If the loss of signal in Figure 4.9 were caused by beamsteering by the shock front, one would expect the signal to return after the shock waves subsided; however the signal did not return. This suggests that a permanent mechanical shift occurs in the gauge that is large enough to destroy the alignment of the optics. Subsequent attempts to increase the rigidity of the gauge were made using epoxy to keep the optics in place. These experiments produced the same results: a loss of signal when the shockwave contacted the gauge. These results suggest that the rigidity of the gauge is a critical limiting factor in such absorption experiments.

In the design of an absorption gauge that can overcome the light collection problems observed in initial experiments, the factors in Table 4.1 are considered.

Attribute	**Motivation**	**Investigation**
• Fiber size	• Smaller fiber yields higher resolution but increases sensitivity of gauge to vibrations	• Fiber size and resolution required for accurate temperature determination is examined
• Necessary path length	• Longer path length allows for better SNR due to more absorption but requires extremely rigid gauge to couple light	• Path length required for temperature measurements of PETN detonations is investigated
• Gauge design	• Small, simple design is desired for ease of implementation	• Other layouts and more rigid designs are considered

Table 4.1 Factors for consideration in the design of new absorption gauge to overcome light collection problems for absorption spectroscopy in detonation environments.

These issues were examined in experiments conducted at Marquette University and will be discussed in the following section.

Bench-Top Experiments (Marquette University)

The results from feasibility studies and furnace experiments conducted at Marquette University will be discussed in this section.

Fiber Size Results (Resolution Study)

The temperature dependence of absorption spectra is manifested in the relative strength of absorption features. For accurate temperature measurements to be made, the spectra must be resolved enough to capture this temperature dependence. As mentioned in Chapter 2, the resolution of a Czerny-Turner spectrometer is a function of input slit size (fiber size), diffraction grating density, and detector pitch. The resolution of the system with various fiber sizes is investigated in this section. First, the resolution of the system was estimated from the fiber size, reciprocal linear dispersion, and pixel pitch. The reciprocal linear dispersion (given by manufacturer) indicates the wavelength density per millimeter at the focal plane. Thus, from the spot size at the focal plane, the resolution of the system can be estimated. In this estimation, the spot size is approximated as the fiber size at the input of the spectrometer. It is also noted that the minimum detectable spot size is limited by the pitch of the detector (25μm) and fibers below this size will not change the resolution beyond the minimum estimated at 25μm.

The spectrometer was setup as described previously for bench-top studies at Marquette University. Fibers of different sizes were inserted into the system and their resolution was determined as described here. The spectrometer recorded spectra at room temperature and pressure (T=300 K P=1atm). A database of simulated spectra (T=300 K P=1atm) with different simulated spectral resolution was compiled. The simulated

resolution was obtained by convolving the simulated spectrum with a Gaussian pulse of defined FWHM, which is the resolution of the resulting spectra. The measured spectra were then compared to simulated spectrum using a least-squares covariance method to determine the resolution of the measured spectra. The measured and estimated resolution of the system are presented in Figure 4.11

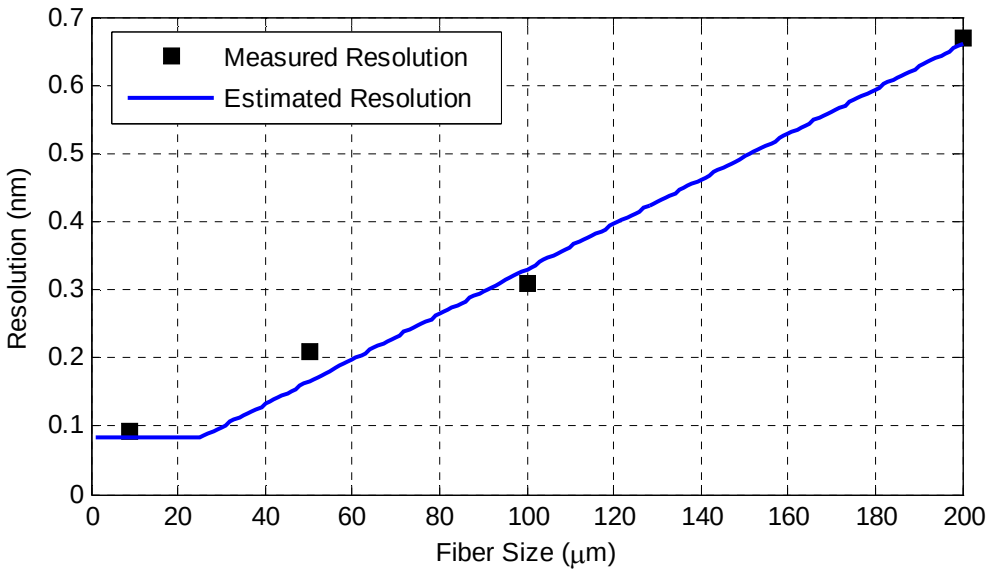

Figure 4.11 Estimated and measured resolution of system.

The resolution of the 9 μm and 50 μm fibers are sufficient to accurately determine temperatures; however, when multi-mode fibers were used, significant mode noise was observed. Figure 4.12 shows sample data from the 50μm fiber showing both the transmitted and reference intensities.

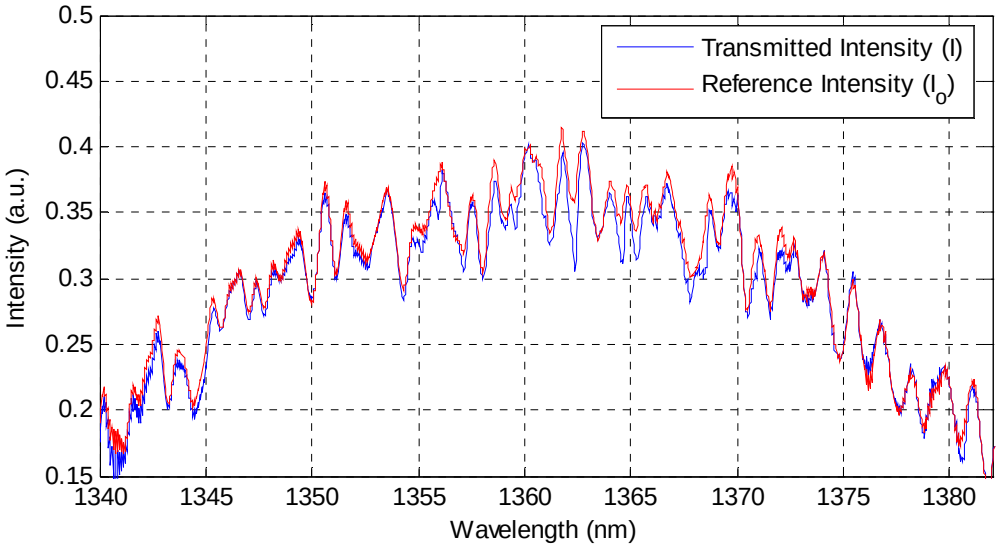

Figure 4.12 Transmitted (I) and reference intensity (I_o) spectra from system with 50 μm fiber showing significant mode noise.

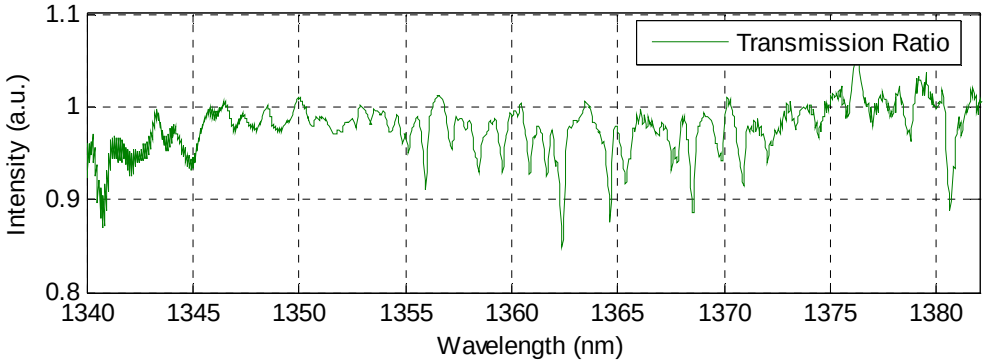

Figure 4.13 Transmission ratio obtained from data in Figure 4.12 using a 50μm fiber. Adequate resolution and H_2O absorption features are observed to determine temperature from the spectrum

The intensity fluctuations in Figure 4.12 are a result of the mode noise from the fiber. With the 50μm fiber, mode noise was on the order of ~20% of the overall signal while peak absorption features are on the order of ~10%. Figure 4.13 shows the transmission ration I/I_o from the data in Figure 4.12, displaying several strong H_2O absorption features. Thus, temperature can be determined from the spectrum in Figure 4.13 as the resolution of the system provides enough detail to discern the variations in intensity of the temperature dependent lines despite the strong mode noise. Unfortunately, this mode

noise is highly dependent upon the orientation of the fiber. In a stable and controlled environment such as a furnace on a bench top, the orientation and states of stress of the fibers can be controlled allowing for consistent and reproducible mode noise; however, in a detonation environment, it is difficult to control the movement and state of stress in the fibers and the fluctuations in signal due to mode noise in the transmission fiber would overcome any absorption signal that is present. Figure 4.14 shows two transmitted intensity (I) spectra acquired consecutively with a 50μm fiber. In between the two spectra, the catch fiber from the gauge was lifted from the table it was resting on. This slight change in position caused a drastic change in the mode noise that is not reproduced in the reference intensity (I_o) causing a transmission spectrum that contains overwhelming artifacts.

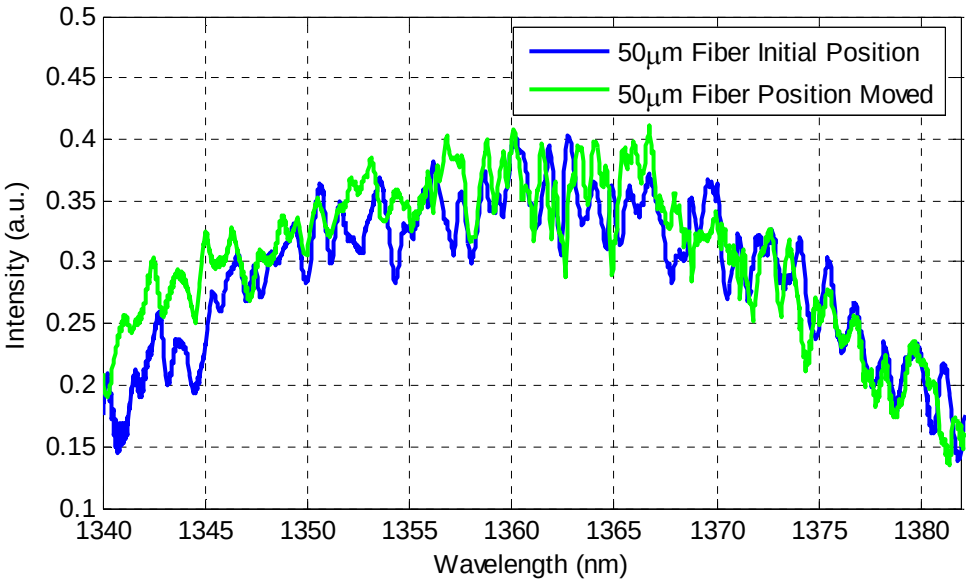

Figure 4.14 Transmitted intensity (I) from 50μm fiber showing significant mode noise. The two spectra were taken consecutively with the catch fiber held in different positions.

From these results it is determined that larger fibers are unlikely to produce acceptable results unless they can be adequately shielded. Another possible alternative is to agitate the fibers rapidly so that the varying effect of the mode noise is averaged out within each exposure and methods for accomplishing this will be investigated in future work. For robustness, the design of a new absorption gauge will take into account the requirements necessary to accommodate a small single-mode fiber, and be capable of using larger fibers if a solution to the mode noise can be developed.

Path-Length Simulation

According to Beer's Law (Equation 4.1) the amount of absorption is dependent upon the path length through the absorbing medium. A longer path-length results in more absorption and thus a higher signal to noise ratio when determining absorbance; however, a longer path length increases the effects of beamsteering and can cause translation of the optics with respect to each other. This can cause incomplete or unsuccessful coupling into the catch fiber. These problems intensify in detonation environments as longer path lengths reduce the rigidity between optics allowing for greater beam translation. Thus, for absorption spectroscopy in explosives experiments the path-length should be carefully considered for optimal design. The shortest path length that produces enough absorption to accurately determine properties is sought.

As mentioned previously, the absorbance at any wavelength is a function of temperature, pressure and mol fraction. In order to estimate the necessary path length, the temperature and pressure history at various distances from a 1" PETN detonation were simulated by Tom Mcgrath at the NSWC-IH. The simulations were performed

using CTH calculations, in which, the detonation properties were used in a Continuum-based model to calculate the expanding blast properties.

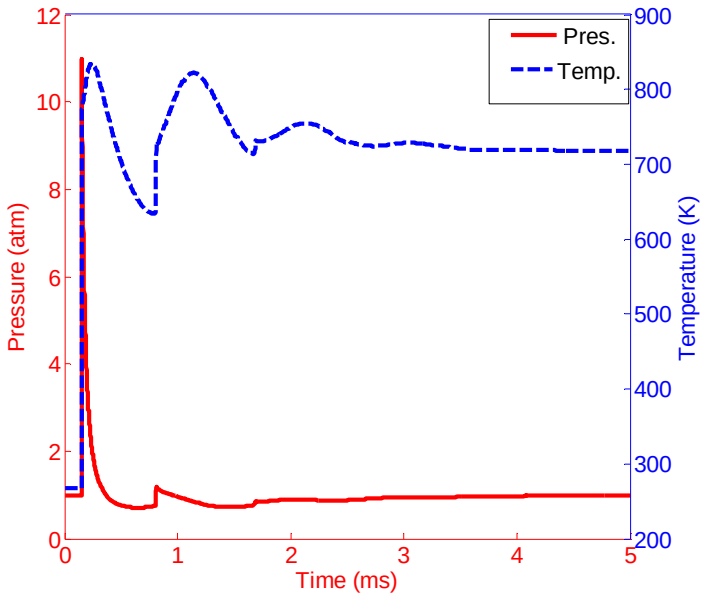

Figure 4.15 Simulated temperature and pressure history 12” from a 1” PETN charge.

Figure 4.15 shows the temperature rise to over 800 K then cool slightly to 700 K over several milliseconds at a distance of 12 inches from the exploding charge. The pressure reaches a maximum of 11 atm. then drops rapidly to nearly 1 atm. From this data and the methods outlined in Chapter 2, H_2O spectra can be simulated at these temperatures and pressures. With a noise level of 1% in the absorption spectrometer, a 10% absorption signal yields a SNR ratio of 10, which is adequate for temperature determination. From the simulated temperatures and pressures, the path length necessary for 10% peak absorption can be determined from Beer’s law and the spectral database and is shown in Figure 4.16.

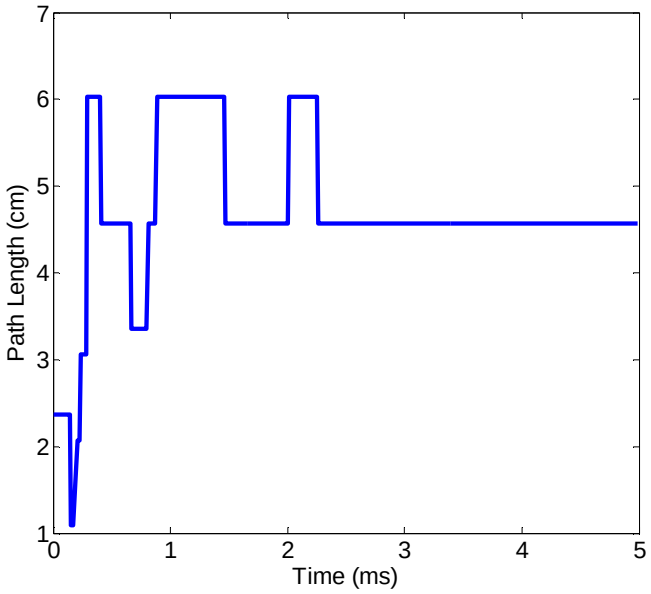

Figure 4.16 Required path length for 10% peak absorption xH2O=0.21 determined from simulated temperatures and pressures for gauge placement 12” from 1” PETN charge.

The low resolution of the path length plot is a result of the coarse resolution of temperatures at which spectra were simulated, i.e. spectra were only simulated in temperature increments of 50 K. From the simulated data, a path length of 8 cm is a conservative estimate to ensure 10% peak absorption for temperatures up to 1000 K and pressures down to near 1 atm. This long path length presents considerable design challenges for the collection of the light with the current system.

Furnace Results

In order to demonstrate the system’s capability to produce temperature measurements from H_2O absorption spectra, experiments were conducted using a T-shaped furnace at Marquette University. The results of these experiments are presented here. When taking measurements with the spectrometer there was significant water

absorption occurring with in the spectrometer. To compensate for this, nitrogen gas was pumped into the spectrometer during experiments. This nitrogen purge reduced the absorption occurring within the spectrometer to just above the noise level and was barely detectable.

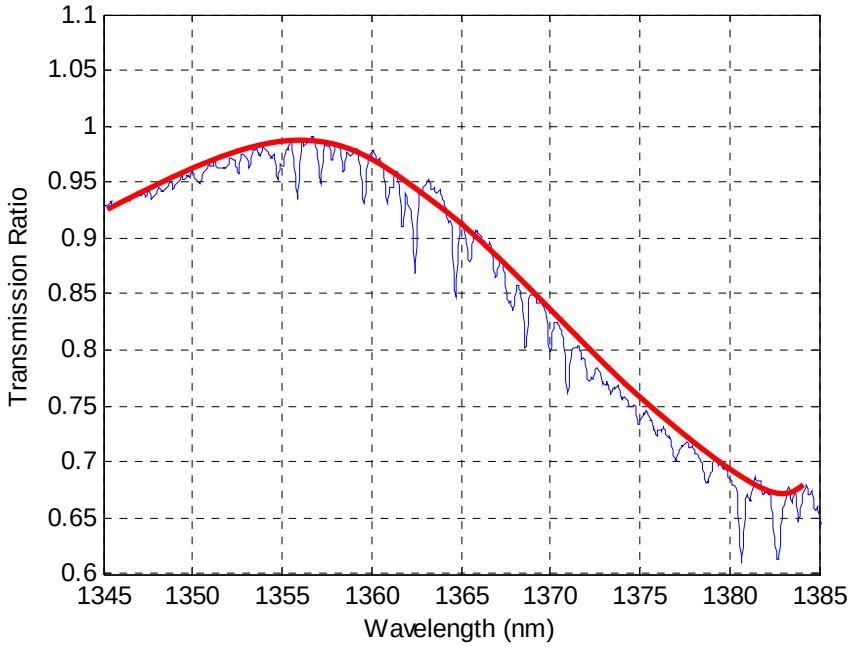

Figure 4.17 Transmission ratio in furnace cell (T=300 K L=10 cm) showing very structured transmission ratio from large differences between I and I_o.

It was observed that the transmission spectra had considerable offsets and the shape of the transmitted *(I)* and reference *(I_o)* spectra were very different. This was partially due to the polarization of each signal and the polarization dependency of the grating and detector. A sample spectrum in which the transmitted and reference signals are very different is shown in Figure 4.17. The spectra in sample 4.17 was taken at room temperature and pressure (T=300K P=1atm) with a path length of 10 cm. To reduce the discrepancies in signals due to polarization, one paddle-wheel polarization controller was placed on each the reference and transmission fibers. The polarization controllers were

adjusted until the detector observed a more flat transmission curve as shown in Figure 4.18.

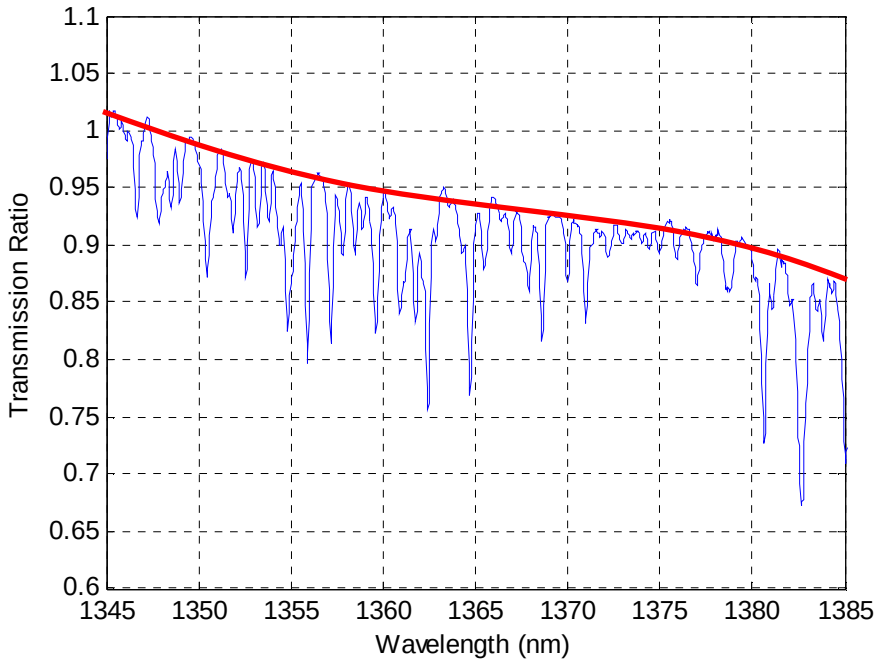

Figure 4.18 Transmission ratio in furnace cell (T=600 K L=10 cm) showing more flat transmission ratio from very similar I and I_o.

The spectrum in Figure 4.18 was taken with a cell path length of 10cm and the furnace temperature set at 600 K. After optimizing the transmission curves, measurements of the furnace at several temperatures were recorded. Using the data reduction procedure outlined previously, temperatures were determined from the measured spectra. Figure 4.19 shows a graph of smoothed differentiated measured and simulated spectra compared from data taken at a furnace temperature of T=860 K and a water cell length of 10 cm.

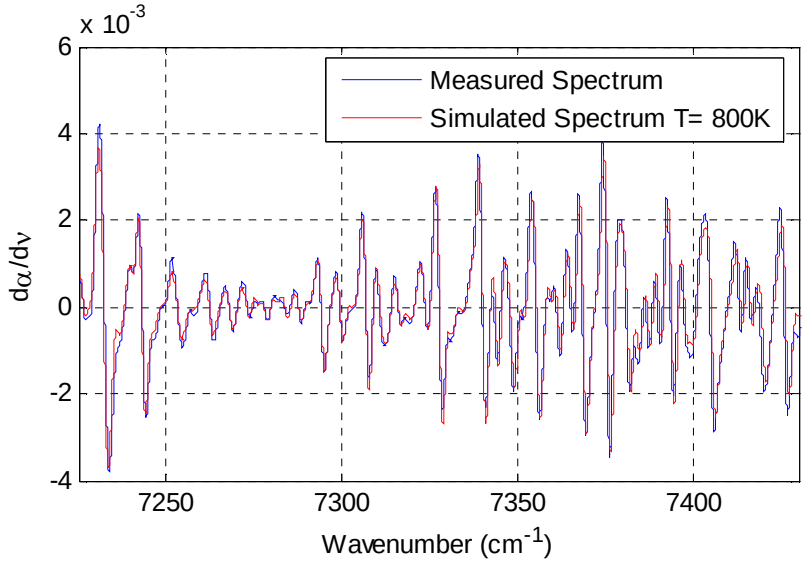

Figure 4.19 Smoothed, differentiated measured and simulated absorption spectra measured in furnace set at T=860 K with a water cell length of 10 cm.

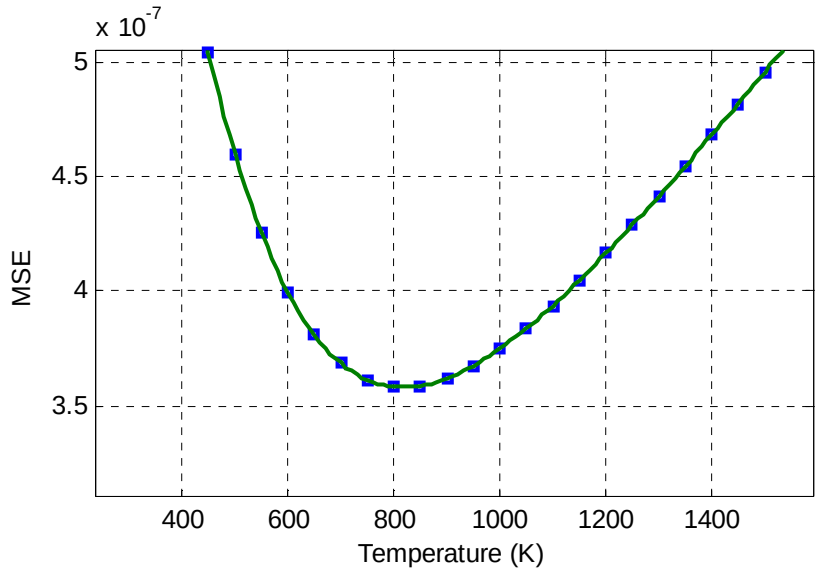

Figure 4.20 Mean-squared error versus simulated temperatures from the measured data in Figure 4.19. Blue points are calculated from spectra in the simulated database. The temperature determined from the least MSE was found to be 820 K.

As shown in Figure 4.20 the temperature determined from the least MSE method was found to be T=820 K and mol fraction was found to be x_{H2O}=0.221. This is slightly below the temperature from the furnace's thermo couple (860 K). This may be due to

thermal gradients within the furnace as well as spectral contributions from cool water absorption between the lenses and fibers. Absorption spectra recorded using a 10 cm path length and ~20% mol fraction water demonstrated adequate absorption and precisely determined the temperature from the spectra.

It should be noted that the temperatures determined from the absorption spectra are path-length averaged. When the thermocouple controlling the furnace was moved to different locations along the path length it was observed that there were temperature differences of up to 10% along the path length. Although the ultimate accuracy of the system cannot be determined from this simple setup, its characteristics and general response are useful in assessing the system's applicability to detonation studies. It was also noted during the furnace experiments that there were significant beamsteering effects from convection currents exiting the furnace ends. This beamsteering was strong enough to reduce the acquired signal by up to 80% at times; however, temperatures could still be determined from the low signal levels. This suggests that beamsteering caused by the shock-front may be strong enough to temporarily attenuate the signal. In attempt to reduce the effects of such beamsteering the fiber is placed slightly beyond the focal length of the lens so that roughly 1% (~0.03 mW) of the light was collected by the fiber. The amount of signal captured was optimized to match the signal intensity from the reference line to provide a baseline transmission ratio of nearly 1. In the benchtop studies, it was found that the collection fiber could be laterally translated up to 80 μm and still retain enough signal to determine a temperature from the spectra (~20% of the max).

New Absorption Gauge Design

From the analysis conducted at Marquette University, it is concluded that the H_2O absorption method for determining temperatures and mole fraction can be applied to the detonation of PETN charges in an arena-type environment if the collection challenges can be overcome. In initial experiments the strong shock wave created during detonation caused mechanical vibration and translation of optical components. This displacement caused a misalignment of the optics and a loss of signal. To reduce the relative movement of optical components in future experiments, a stronger more rigid gauge has been designed. A section view of the new gauge is shown if Figure 4.21.

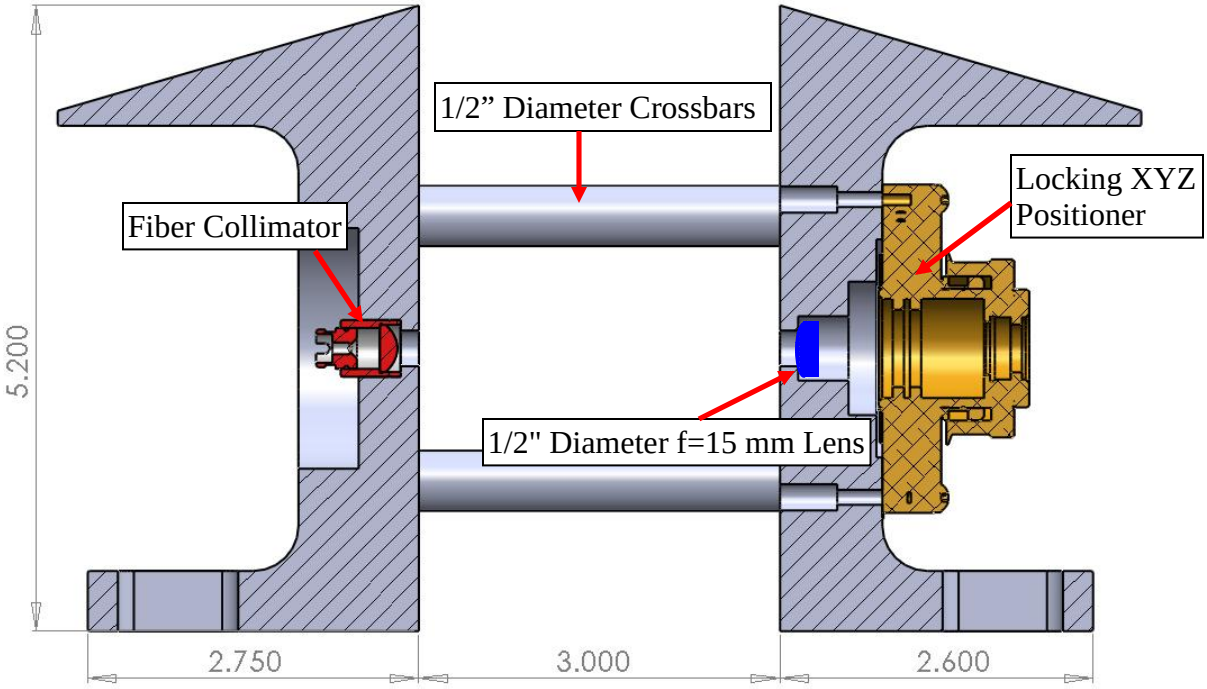

Figure 4.21. Section view of re-designed absorption gauge with more rigid posts, better shielding for components and better locking optical positioner.

The new gauge is made of 1018 steel for its stiffness and machinability. The design incorporates larger ½” diameter crossbars and slight interference fits to increase the

rigidity of the structure and reduce the relative motion of the pitch and catch optics. The crossbars are also removable so the path length can be varied to optimize the amount of absorption. A fiber collimator with a focal length of 8mm and numerical aperture of 0.55 is used on the pitch side to minimize the cool water absorption between the fiber and lens and provide a stable secure method for collimating the pitch fiber (Thorlabs F240FC-C). On the catch side, a ½" diameter 15.0 mm focal length lens is used to focus the light (Thorlabs LA1540-C) onto the single-mode fiber that is held by a locking three-axis positioner (Newport LP-05A-XYZ). This three-axis lens positioner allows for easier alignment of the catch fiber and has a stronger locking mechanism than the one used previously to reducing the potential for movement of the fiber with respect to the lens. The roof of gauge has also been extended to better shield the components from the blast-wave. More detailed drawings of the absorption gauge can be found in Appendix C. Through these improvements to the design of the gauge, it is expected that vibrations will be reduced and the relative motion of optical components will be minimized allowing for sustained coupling of light after the blast-wave hits the gauge in future experiments.

Summary

In this section, the application of the newly developed NIR spectrometer to absorption experiments in detonation environments was investigated. A database of simulated water absorption spectra for temperatures of T=250-3500 K and pressures of P=1-35 atm was created from the BT2 water line list. The database was used in the data reduction procedure outlined in this section to determine temperatures from measured water absorption spectra. A Labview program was created to precisely control the timing

of the system and was adjusted to provide optimal SNR. Temperature measurements for spectra were successfully obtained at temperatures of T=300-900 K and P=1 atm using a furnace at Marquette University. These experiments demonstrated the systems capabilities and limitations. It was determined that a single mode fiber must be used in such experiments as mode noise present in multi-mode fibers is greater than the measurable absorption signal. Also, a path length of 8 cm was determined to provide adequate signal levels at temperatures up to 1000 K. The resolution of the spectrometer was determined to be 0.093 nm with a spectral range of ~45 nm.

Experimental challenges associated with detonation environments proved to be problematic in initial experiments conducted at the Naval Surface Warfare Center at Indian Head, Maryland. The collection of the NIR light into the catch fiber proved difficult and the signal was lost after the shock front reached the device. Since single-mode fibers must be used, methods for reducing the effect of the blast on the gauge are sought. A more rigid gauge design is sought with stronger connections between optics. Other methods for reducing the effect of the blast are being considered for future experiments including the use of a skimmer plate to shield the absorption gauge from the majority of the blast. The system shows great potential for making absorption measurements in detonation environments. If the collection problems can be solved, the system can be used to capture high-speed H_2O absorption spectra and produce measurements of temperature and mol fraction H_2O.

Chapter 5:
Summary and Future Work

Summary

The ability to create novel energetic materials with properties tailored for specific applications, such as agent defeat, is sought; however, the chemical kinetics and decomposition pathways of explosive materials are not entirely known. In order to better understand such pathways, high-speed measurements of properties during detonation and post-detonation combustion events are needed. Optical diagnostics including emission and absorption spectroscopy are attractive tools for making such measurements due to their potential for minimally invasive, high-speed measurements. In order to implement emission and absorption spectroscopy in explosive environments, several experimental challenges must be overcome. As stated in Chapter 1, the objective of this work is twofold:

1. Develop and apply a fast near-infrared spectrometer for measurement of spectral emission features and temperatures of atomic and molecular species

with microsecond time resolution in an arena type high explosives experiment.

2. Investigate the feasibility of using the newly developed near-infrared spectrometer for measuring water absorption in the NIR region to determine temperatures and concentrations of water using a fiber coupled broad light source.

The following sections summarize the achievements made in this work.

NIR Emission Spectroscopy

High-speed ultra-violet and visible emission spectroscopy has been employed in past arena-type explosive experiments to examine atomic and molecular species present in the detonation and post-detonation combustion processes (Carney, Miller et al. 2006). Such measurements have been expanded to the near-infrared region with the development of the fast near-infrared spectrometer detailed in this work. The characteristics of the spectrometer have been evaluated and relevant features and specifications are presented in table 5.1.

The NIR spectrometer was used to observe emission from PETN based explosive formulations. Atomic features were identified in the highly structured emission present immediately following detonation and such features were found to last less than ~40 μs. The temporal resolution of the spectrometer is high enough to observe the highly structured emission from breakout for the first time in the NIR; however, the resolution is not high enough to obtain quantitative data such as the relative lifetimes of the species. Baseline spectra of pure PETN were recorded from 750-1500 nm that have potential to be

used for detonation discrimination. When aluminum or silver were present in the explosive formulations, broad Planckian emission was observed following the decay of the structured emission lasting for hundreds of microseconds. Spectral pyrometry temperatures were determined from the spectra showing initial (0-60 μs) temperatures of 3000-45000 K cooling rapidly to nearly steady temperatures of 1200-1800 K at later times (60-400 μs). The NIR spectrometer has demonstrated temporally and spectrally resolved measurements in arena-type explosive experiments and extends the range for high-speed spectroscopic tools into the NIR.

Feature	Specifications
• High temporal resolution	• Up to 21μs
• Spectral resolution (depending on grating and fiber used)	• 0.093nm-25nm
• Spectral range (depending on grating and fiber used)	• 45nm-250nm
• Large dynamic range	• 2000:1 dynamic range at highest sensitivity • Captures high intensity breakout • Captures low intensity broad emission
• Versatile	• Emission experiments • Absorption studies
• Easily implemented	• Fiber coupled • PC based DAQ • Up to 10,000 spectra per shot (RAM limited) • Minimally invasive
• Scalable	• Blast chamber studies • Field tests • Shock tube experiments

Table 5.1. Relevant features and specifications of newly developed NIR spectrometer.

NIR H_2O Absorption Method Feasibility

Using the newly developed NIR spectrometer and a broad NIR light source, the feasibility of applying the method developed by Kranendonk *et al.* to obtain temporally resolved temperature and mol fraction H_2O from absorption spectra in detonation environments was investigated in this work (Kranendonk, Caswell et al. 2007). In initial experiments using 1" PETN charges at the NSWC-IH, signal was repeatedly lost after the blast wave reached the absorption gauge. Studies to determine the characteristics of the system and its applicability to explosives experiments were carried out at Marquette University.

The path-length necessary to determine temperatures from measured absorption spectra was determined from simulations of temporally resolved temperature and pressure measurements following a 1" PETN detonation and simulated water absorption spectrum. The necessary path-length for 10% peak absorption at temperatures up to 1000 K was determined to be 8 cm. An investigation on the fiber size that can be used in the system and the resulting resolution was also carried out. It was found that a 50 μm fiber provides adequate resolution; however significant mode noise prevents its use in detonation environments. Thus, a 9 μm single-mode must be used with this system providing a resolution of 0.093 nm and spectral range of ~45 nm. The collection of light into a single mode fiber is difficult and very sensitive to even small relative movement of optical components. Methods for reducing the relative movement of optics through more rigid fixtures and skimmer plates are sought. Finally, water absorption spectra were measured using a small furnace at Marquette University. These measurements

demonstrated the capabilities of the system and temperatures were successfully determined from the measured spectra.

Future Work

The NIR spectrometer presented in this work provides a new diagnostic tool for examining explosive events. Future NIR emission spectroscopy could provide more accurate results with modifications to the experimental techniques. It has also been determined in Chapter 4, that NIR H_2O absorption measurements are feasible if the collection challenges are overcome. A brief summary of suggestions for future work is presented here.

NIR Emission Spectroscopy

The NIR spectrometer developed in this work extends the range to which high-speed, spectrally resolved measurements can be made in detonation environments. The techniques presented in Chapter 3 to study PETN based explosions can be applied to other explosive formulations to investigate atomic and molecular features present and baseline the emission spectra of common explosives in the NIR. Such work can be useful in the remote identification of explosive formulations and can also provide insight of the molecules present in the decomposition of explosive formulations. Future experiments examining large-scale field tests with the NIR spectrometer are planned for identification of spectral features of different formulations.

In chapter 3, spectral pyrometry measurements were made of Al and Ag doped PETN formulations. It was noted that signal levels were low and particle emission only

lasted for a few hundred microseconds. With a higher concentration of Al or Ag particles in the explosive formulation, the emission intensity increases and lasts for a longer period of time. Future tests involving higher particle loads can provide better signal to noise ratio for use in determining spectral pyrometry temperatures and produce measurements for a longer time. Aluminum and silver were present in the formulations to manipulate the properties of the explosives; however, neither of these species had two strongly emitting lines observable in the range of the spectrometer. To obtain quantitative measurements from atomic lines in emission spectra other strongly emitting species such as barium nitrate could be doped into the explosive formulation. Using a two-line method, high-speed temperature measurements could be produced from this system.

NIR H_2O Absorption Spectroscopy

While collection challenges in initial experiments eliminated signals, the application of NIR H_2O absorption spectroscopy to arena type explosive experiments using the system developed in this work remains possible. To reduce the vibrations and mechanical translation occurring in the absorption gauge a more rigid fixture has been designed. This fixture utilizes stronger more rigid cross beams and better protects the optical components. Also, more robust and easier to lock optic positioners are to be used to further reduce collection losses. Another technique that will be implemented in future experiments is the use of a skimmer plate to protect the optical fixture from the incoming shockwave.

Such experiments will be carried out at the Naval Surface Warfare Center in Indian Head Maryland. The experiments will be conducted to determine the limits of the

new gauge for making absorption measurements. To maximize the chance of retaining signal after the blast-wave hits experiments will start with half-inch charges of pure PETN will be hung at 12 inches from the gauge with a path length of 1 inch. If the signal is retained during the experiment, the path length will be widened to improve the amount of absorption that is detected. Temperatures will be determined from the measured spectra and are expected to follow a similar trend as shown in the simulations with a high peak temperature followed by some oscillation and a slow cool-down process.

If signal is lost during the initial experiments, a skimmer plate will be used to protect the gauge from the blast-wave. Also, experiments using a larger catch fiber are planned. Mode noise in such experiments will prevent reliable temperature measurements with the current system. Such measurements are still useful to investigate the use of other absorption systems that do not require single mode fibers for arena-type explosive experiments. If the ability to collect light with larger fibers is demonstrated, a system utilizing an FDML laser has potential to provide NIR H_2O absorption spectroscopy measurements. If light collection is not possible in arena-type explosives experiments, the possibility of measuring H_2O absorption during a deflagration reaction PETN will be explored. During a deflagration event, temperatures and pressures are lower than a detonation event and no strong-blast wave occurs. Without this blast wave it is expected that light collection will be possible and temperatures and mole fraction water can be measured. Although these temperatures and concentrations may not directly correlate to detonation events, they can provide insight into the mechanisms that occur during reactions with PETN.

Appendix A:
H_2O Spectral Database Creation

Introduction: The BT2 database is a computed list of H_2O infrared transition frequencies and intensities. H_2O is one of the most abundant molecules in the universe and is present in many astrophysical environments. An accurate water line list is essential for interpreting spectra from applicable sources. The spectrum of water extends over a wide wavelength range from millimeter to ultra-violet, and is caused by quantized chances in the rotation-vibration energy of the atomic nuclei moving in the electronic potential well. The BT2 list is the most complete water line list in existence comprising over 500 million transitions and is also the most accurate (Barber, Tennyson et al. 2006). Comparison of observed intensities with those of the BT2 line list can yield water concentration and temperature data.

Using the BT2 Database: The BT2 database and associated fortran program are available in a compressed form at http://www.tampa.phys.ucl.ac.uk/ftp/astrodata/water/BT2. The site contains several compressed files necessary to use the BT2 database.

1. The necessary files are:
    a. **levels.dat.bz2** -list of energy levels
        (once unzipped rename **fort.80**)
    b. **xxxxx-xxxxx-BT2.txt.bz2** –list of transitions sorted by frequency
        (select the appropriate set of data for the frequency range of interest, once unzipped rename **fort.13**)
    c. **spectra-BT2.f90** –fortran program used to output data of interest i.e. transitions, intensities, etc.
    d. **spec.job** –a sample input file that can be altered for desired conditions
    e. **readme-spectra** –detailed information on inputs and outputs
    f. **ReadMe –**if further clarification is necessary

2. There are 12 necessary subroutines for **spectra-BT2.f90** from http://netlib2.cs.utk.edu/. The following are direct links to all of the necessary subroutines:

    a. http://netlib2.cs.utk.edu/cgi-bin/netlibfiles.pl?filename=slatec/src/dpsort.f.
        1. **dpsort.f**
        2. **fdump.f**
        3. **i1mach.f**
        4. **j4save.f**
        5. **xercnt.f**
        6. **xerhlt.f**
        7. **xermsg.f**
        8. **xerprn.f**
        9. **xersve.f**
        10. **xgetua.f**

    b. http://netlib2.cs.utk.edu/slatec/src/dpperm.f
        1. **dpperm.f**

    c. http://netlib2.cs.utk.edu/slatec/src/ipperm.f
        1. **ipperm.f**

3. All 13 fortran programs are **complied** in same directory using appropriate compiler.

4. The program **spectra-BT2.f90** is ready to be run.

5. The **spec.job** file contains the inputs. A sample **spec.job** is displayed below with important inputs highlighted. A detailed list of inputs is contained in **readme-spectra.**

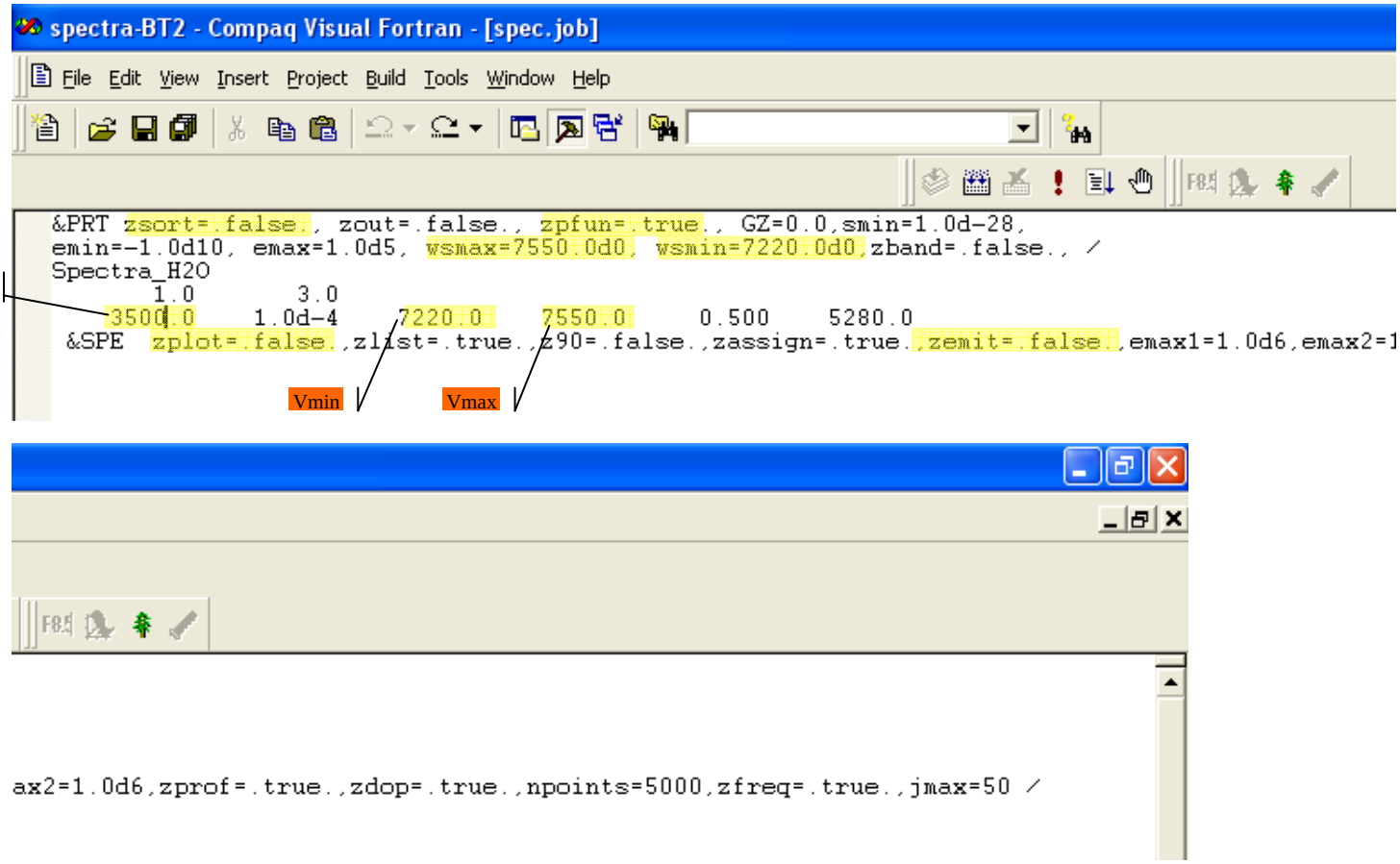

a. **Zsort** – if =true, then program sorts data and writes it to fort.15 file. Necessary the first time the program is run for a specific frequency range. After appropriate fort.15 file is created, can be set to =false to save computational time.
b. **Zpfun** – if = true, the program calculates the partition function, Q(T), at the required temperature. Is necessary for intensity calculations.
c. **Wsmax –** maximum transition frequency required.
d. **Wsmin –** minimum transition frequency required.
e. **T** –temperature
f. **Vmin** –same as Wsmin
g. **Vmax** –same as Wsmax
h. **Zplot –** if =true outputs a 2 column intensity vs wavenumber file for plotting. (not necessary as it does not assume voigt lineshapes).
i. **Zemit –** if=false program produces data for absorption spectrum.

6. **Outputs –** the important output of the program is the **fort.36** file containing details of all the transitions meeting the chosen parameters. The format of the **fort.36** file may alter depending upon the **spec.job** settings. In its fullest form, the **fort.36** data are arranged in the order detailed below.

1) A code 1-4 relating to symmetry blocks (See Table 1, Barber et al.) 3 & 4 are Ortho states and are triply degenerate. 1 & 2 are Para states and are undegenerate. This code is for state A.

2-8) `Look-up' reference in `BT2 Levels File' relating to a specific J & symmetry block; v1,v2,v3,J,Ka,Kc, for state A.

9) As 1), but here relating to state B. It should be noted that only Ortho-Ortho and Para-Para transitions are permitted.

10-16) As 2-8), but here relating to state B.

17) Absolute `Look-up' of state A in `BT2 Levels File'

18) As xvii, but for state B

19) Energy of the lower of the two states (A & B) in cm-1

20) Fequency of the transition in cm-1

21) Intensity of the line intensity in units of cm/molecule.

22) The Einstein A coefficient

Using Selected Line List: The line list created by the **Spectra-BT2.f90** program can be used to create simulated absorption spectra that can be compared to experimental absorption spectra to determine different parameters. The BT2 database provides a list of line frequencies (column 20 of **fort.36**) and intensities (column 21 of **fort.36**). From Beer's law, absorbance can be related to line intensity as follows (Hanson 2006):

$$\alpha = I * n * x_i * L * \phi_\nu(\nu)$$

Where

- α = absorbance
- I = line intensity [cm/molecule] (from **fort.36)**
- n = number density [molecules/cm^3]
- x_i = mol fraction species i
- L = path length [cm]
- ϕ_ν = lineshape function [cm]

***n* - Number Density Assuming Ideal Gas:**

$$n = \frac{P * N_A}{T * R}$$

Where

- n = number density [molecules/cm^3]
- P = pressure [atm]
- T = temperature [K]
- N_A = Avagadro's number [6.02214E23 molecules/mol]
- R = universal gas constant [82.05746 (cm^3-atm)/(K-mol)]

***x_i* – mol fraction of species i:** can be determined from chemical equilibrium for simulated spectra then solved for when comparing experimental data with simulated.

***L* – Path Length:** can be chosen based on experimental setup.

ϕ_ν - Lineshape Function: The lineshape function can be evaluated using a voigt profile which combines Gaussian (Doppler) and Lorentzian (collisional) distributions. Both profiles are defined by their FWHM $\Delta\nu$.

$$\phi_\nu(\nu) = \frac{2}{\Delta\nu_D}\sqrt{\frac{\ln(2)}{\pi}} * V(a,w)$$

Where

$V(a,w)$ = Voigt Function at (a,w)
$\Delta\nu_D$ = FWHM [cm^{-1}] for Doppler broadening

Voigt "a" parameter

$$a = \sqrt{\ln(2)}\,\frac{\Delta\nu_C}{\Delta\nu_D}$$

Non-dimensional line position "w"

$$w = \frac{2\sqrt{\ln(2)} * (\nu - \nu_o)}{\Delta\nu_D}$$

Where

$\Delta\nu_C$ = FWHM [cm^{-1}] for collisional broadening
ν = position in frequency space [cm^{-1}]
ν_o = linecenter position in frequency space [cm^{-1}]

$\Delta\nu_D$ FWHM for Doppler broadening

$$\Delta\nu_D = \nu_o\sqrt{\frac{8 * k * T * \ln(2)}{m * c^2}}$$

Where

ν_o = linecenter position in frequency space [cm^{-1}]
k = Boltzmann's constant [1.3807E-23 (kg-m^2)/(s^2-K)]
T = temperature [K]
m = mass per molecule [kg]
c = speed of light [2.9979E8 m/s]

$\Delta\nu_C$ FWHM for collisional broadening with air:

$$\Delta\nu_C = 2 * P * \left[x_i * \gamma_{self} * \left(\frac{T_o}{T} \right)^n + (1 - x_i) * \gamma_{air} * \left(\frac{T_o}{T} \right)^n \right]$$

Where

P	=	pressure [atm]
x_i	=	mol fraction species i
γ_{self}	=	self-collisional broadening coefficient [cm^{-1}-atm^{-1}]
γ_{air}	=	air-collisional broadening coefficient [cm^{-1}-atm^{-1}]
T	=	temperature [K]
T_o	=	reference temperature [K]
n	=	temperature exponent

The BT2 database does not include broadening coefficients, thus an approximation developed by Kranendonk is used in this case. The following equation was developed from 6000 measured spectra spanning 5 to 35 atm (Kranendonk, Caswell et al. 2007):

$$\Delta\nu_C = 0.019 * P + 0.652$$

Where

$\Delta\nu_C$	=	FWHM [cm^{-1}] for collisional broadening
P	=	pressure [atm]

Voigt Function – the voigt function V(a,w) must be evaluated. There are several algorithims in existence that will quickly and accurate approximate the Voigt function. The algorithim used in this example is one developed by Wells and is included in the appendix (Wells 1999).

Creating absorption spectra – Absorption spectra can be created from the preceding equations and the outputs from the BT2 database. A simple Matlab or other programming language code can easily be implemented to produce the desired spectra.

Using Database – A code has been developed to compare simulated spectra across a range of temperatures and pressures with experimental spectra to determine the temperature and pressure of the experimental spectra.

Absorption spectra creating m-file: AbsVTc.m

```
function AbsVTc(T,P,res)
tic
%T = 2000    %2000        %[K]
%P = 15    %13.6        %[atm]
%res = .04 %res = resolution [cm^-1/point]
vl = 7220;
vu = 7550;

L = 1;                      %L = path length [cm]
Xi = .2126;             %Xi = mol fraction water from EES chem equi.
n = P/T*6.022141E23/82.0574587;   %n = molar density [molecules/cm^3] Ideal gas

vC = 0.019*P+0.652;         %Collisional FWHM
N = (vu-vl)/res+1;                      % N =# of points

xx2 = linspace(vl,vu,N);  %7240 7520
Kv=zeros(size(xx2));
%%%%%%%%%%%%%%%%%%% inputs from BT2 will be 2 columns x0s and Is

iname = sprintf('T_H2O_7220_7550/%3.0fK_H2O_7220_7550.txt',T);
BT2=load(iname);
[c,r]=size(BT2);
x0s=BT2(:,20);
Is=BT2(:,21);
%%%%%%%%%%%%%%%%%%
thr = 1E-8; %%threshold
for j= 1:c
    x0j = x0s(j);
    Ij = Is(j);
    vDj = x0j*sqrt(8*1.3807E-23*T*log(2)/(2.9915E-26*(299792458)^2));   %Doppler FWHM
    aj = sqrt(log(2))*vC/vDj;     %Voigt a parameter
    xx2t = abs(xx2-x0j);
    [f,g] = min(xx2t);
    alk = 1;
    for k = g:N
         if alk < thr, break,end
            w2k = 2*sqrt(log(2))*(xx2(k)-x0j)/vDj;
            phik = 2/vDj*sqrt(log(2)/pi)*Voigt(w2k,aj);
            alk = Ij*n*Xi*L*phik;
            Kv(k) = Kv(k)+ Ij*n*Xi*L*phik;
    end

    alk = 1;
    for k = g-1:-1:1
         if alk < thr, break,end
            w2k = 2*sqrt(log(2))*(xx2(k)-x0j)/vDj;
            phik = 2/vDj*sqrt(log(2)/pi)*Voigt(w2k,aj);
            alk = Ij*n*Xi*L*phik;
            Kv(k) = Kv(k)+ Ij*n*Xi*L*phik;
    end
end

xx2Kv = [xx2',Kv'];
oname =
sprintf('T_P_res_H2O_7220_7550/%04.0fK_%04.1fatm_%3.3fres_H2O_7220_7550',T,P,res);
save(oname,'xx2Kv','-ASCII');
toc

%T_P_res_H2O_7220_7550/%04.0fK_%04.1f_atm_%3.2f_res_H2O_7220_7550
```

Voigt function m-file: Voigt.m

```
function [W] = Voigt(X,Y)
%VOIGT Normalized Voigt profile
%
% [W]=Voigt(X,Y)
%
% Uses Humlicek's algorithm for calculating the Voigt profile
%
% X = position/frequency
% Y= Voigt ``a" parameter (ratio of Lorentz to Doppler widths)
% W = Voigt value
% area = sqrt(pi)
% width (FWHM) = (Y+sqrt(Y*Y+4*ln(2))) (approximation)
% linecenter is at X=0
% amplitude = Voigt(0,Y)
%
% To use with curve-fitting or for simulating absorption spectra,
% use this function the following way:
%
% Lineshape = amp* Voigt((2*sqrt(log(2))/WG)*(x-x0),a)
% amp = 2*(sqrt(ln(2))*S*P*xj/(sqrt(pi)*WG)
% log(2) = ln(2)
% WG = Doppler FWHM

% x = frequency position at which to calculate the Voigt function
% x0 = linecenter
% a = Voigt ``a" parameter
%
% For calculating the amplitude, S is the integrated linestrength
% [cm^(-2)/atm], P is the pressure [atm], and xj is the
% molefraction of species of interest

T = complex(Y,-X);
S = abs(X)+Y;
if S >= 15 %Region I
    W= T*0.5641896/(0.5+T*T);
else
    if S >= 5.5 %Region II
        U= T*T;
        W= T*(1.410474+U*0.5641896)/(0.75+U*(3+U));
    else
        if Y >= (0.195*abs(X)-0.176) %Region III
            Wnum= (16.4955+T*(20.20933+T*(11.96482+T*...
                (3.778987+T*0.5642236))));
            Wden= (16.4955+T*(38.82363+T*(39.27121+T*...
                (21.69274+T*(6.699398+T)))));
            W=Wnum/Wden;
         else %Region IV
            U= T*T;
            Wnum=T*(36183.31-U*(3321.9905-U*(1540.787-U*...
            ( 219.0313-U*(35.76683-U*(1.320522-U*0.56419))))));
            Wden =(32066.6-U*(24322.84-U*(9022.228-U*(2186.181...
            -U*(364.2191-U*(61.57037-U*(1.841439-U)))))));
            W=Wnum/Wden;
            W= complex(exp(real(U))*cos(imag(U)),0)-W;
        end
    end
end
W = real(W);
```

Appendix B: Temperature and Mol Fraction Measurements from H_2O Absorption Spectrum

Matlab Code Txdet.m

```
clear
tic
%load measured data
mTr=load('C:/Documents and Settings/4he4piecuchs/Desktop/NIRSpec/09.02.12/C.txt');
mvvnm=load('C:/Documents and Settings/4he4piecuchs/Desktop/NIRSpec/09.02.12/vv.txt');
mxx=1e7./mvvnm;
mvl=min(mxx);  mvh=max(mxx);

P=1;   %for P=1to10 res=.02     P=11to25 res=.03        P=26to35 res=.04
resh=.02;

%Transmission to Absorption I/Io
l=10;
mKv=-log(mTr)/l;
%smoothing factors
smVg=2;
smVin=0.5;
smVsim=sqrt(smVin^2+smVg^2);

%interpolate, smooth, differentiate measured spectrum
hxx=xxcrtr(mvl,mvh,resh);
mKvh=interp1(mxx,mKv,hxx,'pchip');
[msmKvh]=gpsmooth(smVg,mKvh,resh);
mpp=pchip(hxx,msmKvh);
[breaks,coefs,l,k,d] = unmkpp(mpp);
dmpp = mkpp(breaks,repmat(k-1:-1:1,d*l,1).*coefs(:,1:k-1),d);
dmsmKvh=ppval(dmpp,hxx);

T=(250:50:3500);
tsz=length(T);
if P<=10
   res=.02;
elseif P<=25
   res=.03;
else
   res=.04;
```

```
end

%initialize values
sl=zeros(size(T)); mse=sl;
ismKvh=zeros(length(msmKvh),tsz); dismKvh=zeros(length(dmsmKvh),tsz);

%interpolate, smooth, differntiate simulated spectrum and compare
for i=1:tsz
   [iKv]=Kvextr(T(i),P,res);
   ixx=xxcrtr(7220,7550,res);

   iKvh=interp1(ixx,iKv,hxx,'pchip');
   [ismKvh(:,i)]=gpsmooth(smVsim,iKvh,resh);
   ipp=pchip(hxx,ismKvh(:,i));
   [breaks,coefs,l,k,d] = unmkpp(ipp);
   dpp = mkpp(breaks,repmat(k-1:-1:1,d*l,1).*coefs(:,1:k-1),d);
   dismKvh(:,i)=ppval(dpp,hxx);

   [sli,sdi,msei]=lscov(dismKvh(:,i),dmsmKvh);
   sl(i)=sli;
   mse(i)=msei;
end

[im,jm]=min(mse);
Tml=T(jm)

%interpolate Temperature
Th=250:10:3500;
mseh=interp1(T,mse,Th,'spline');
[imh,jmh]=min(mseh);
Thml=Th(jmh)

%mol fraction
sll=interp1(T,sl,Th,'linear');
sllf=sll(jmh);
xh20=.2126*sllf

%plot mse
figure
plot(T,mse,'o',Th,mseh)
grid on

toc
```

Appendix C:
Absorption Gauge Design Drawings

This appendix includes drawings for the design of the new absorption gauge to be used in future H_2O absorption experiments as described in Chapter 4. Two separate gauges were constructed to use different optical positioners. Both gauges used the same design for the pitch side that included a fiber collimator with a focal length of 8mm and numerical aperture of 0.55 is used on the pitch side to minimize the cool water absorption between the fiber and lens and provide a stable secure method for collimating the pitch fiber (Thorlabs F240FC-C). The drawings for the pitch side are shown in Figures C.1 and C.2. The design of the two different catch pieces is similar but each is designed for a specific opto-mechanical positioner. On the catch side, a ½" diameter 15.0 mm focal length lens is used to focus the light (Thorlabs LA1540-C) onto the single-mode fiber that is held by a locking three-axis positioner. The first catch piece is designed to hold a Newport LP-05A-XYZ and is shown in Figures C.3 and C.4. The second catch piece is designed to hold a Newport FPR1-C1A three-axis positioner that incorporates a fiber chuck and is shown in Figures C.5 and C.6.

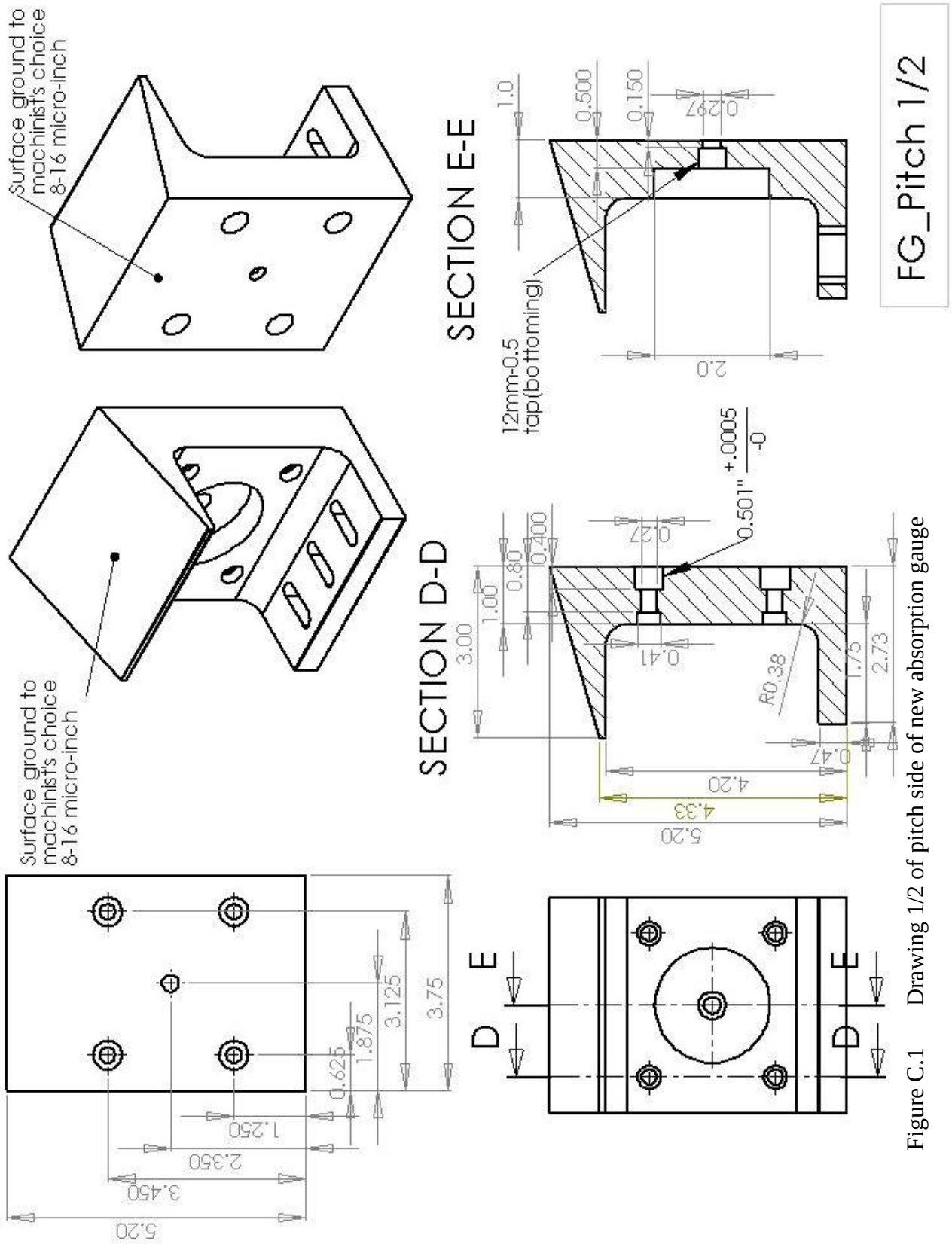

Figure C.1 Drawing 1/2 of pitch side of new absorption gauge

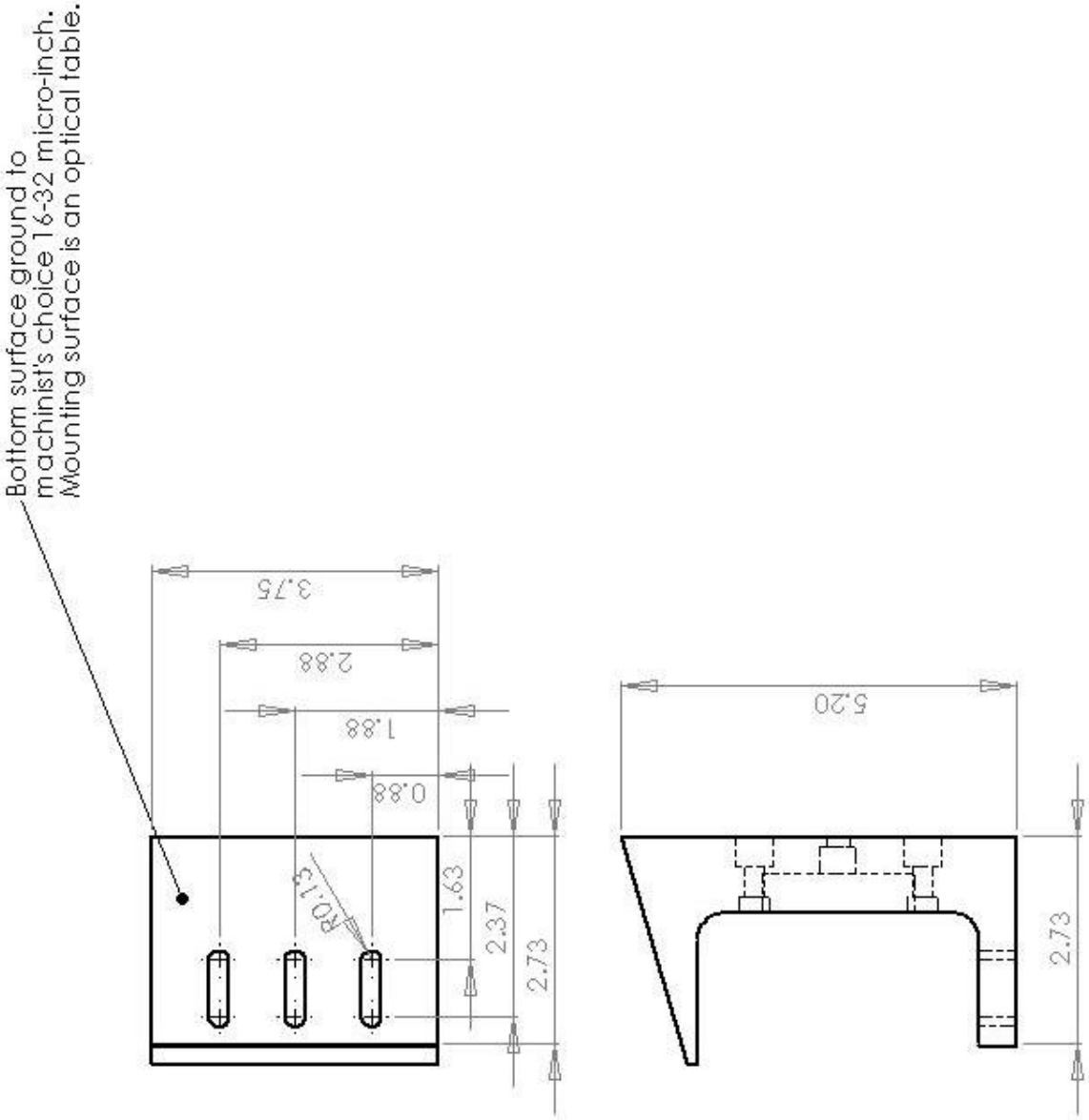

FG_Pitch 2/2

Figure C.2 Drawing 2/2 of pitch side of new absorption gauge

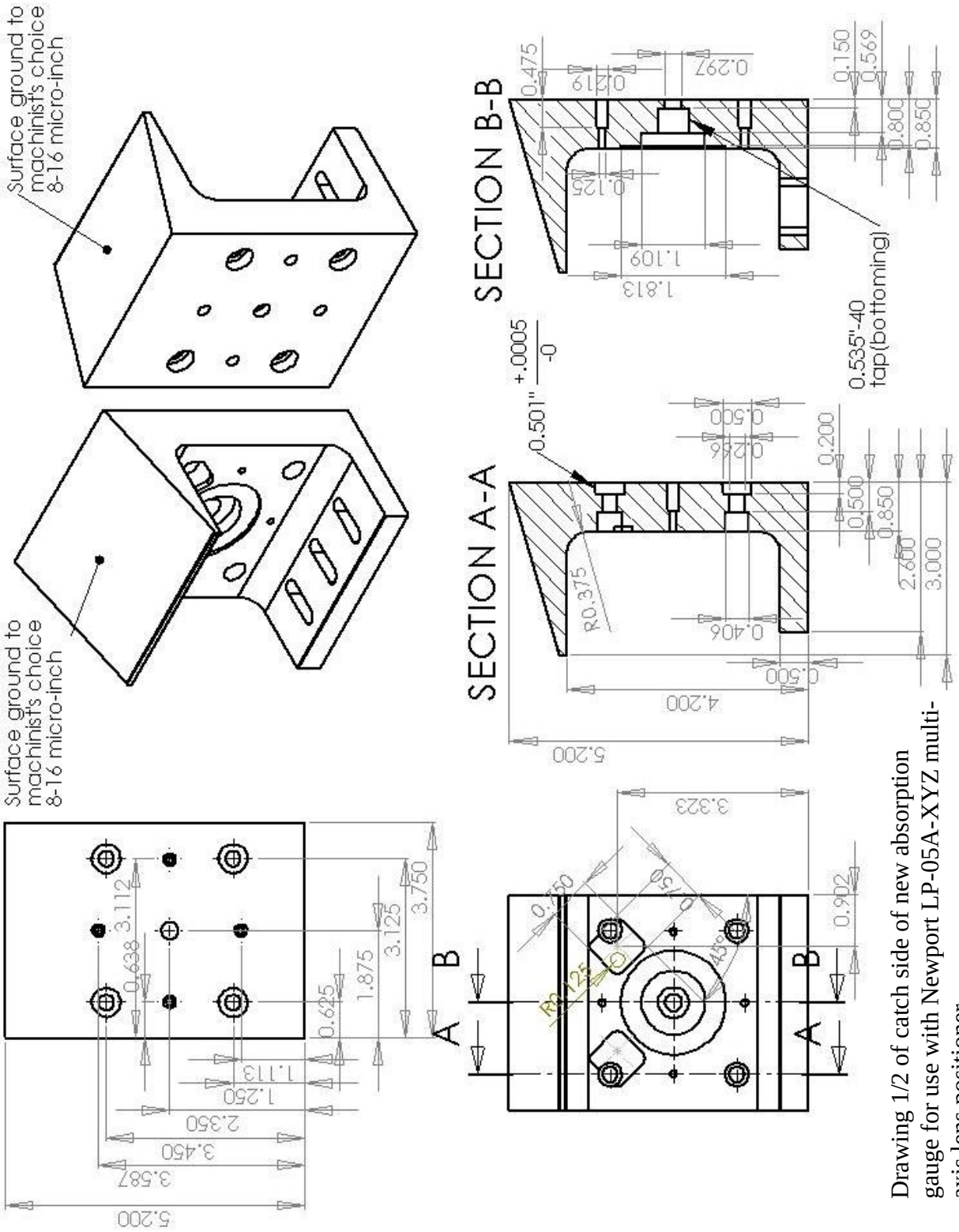

Figure C.3 Drawing 1/2 of catch side of new absorption gauge for use with Newport LP-05A-XYZ multi-axis lens positioner

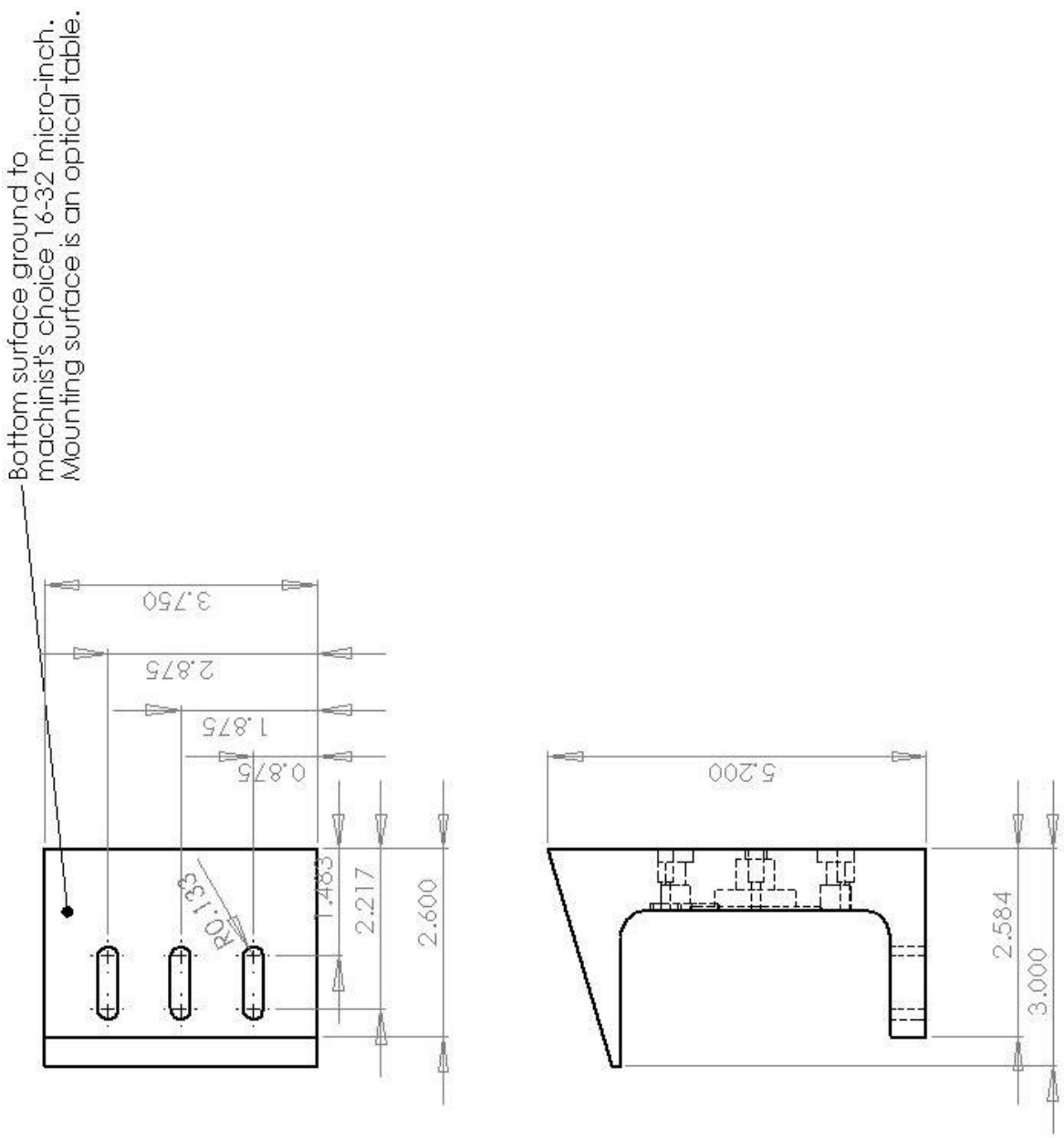

Figure C.4 Drawing 2/2 of catch side of new absorption gauge for use with Newport LP-05A-XYZ multi-axis lens positioner

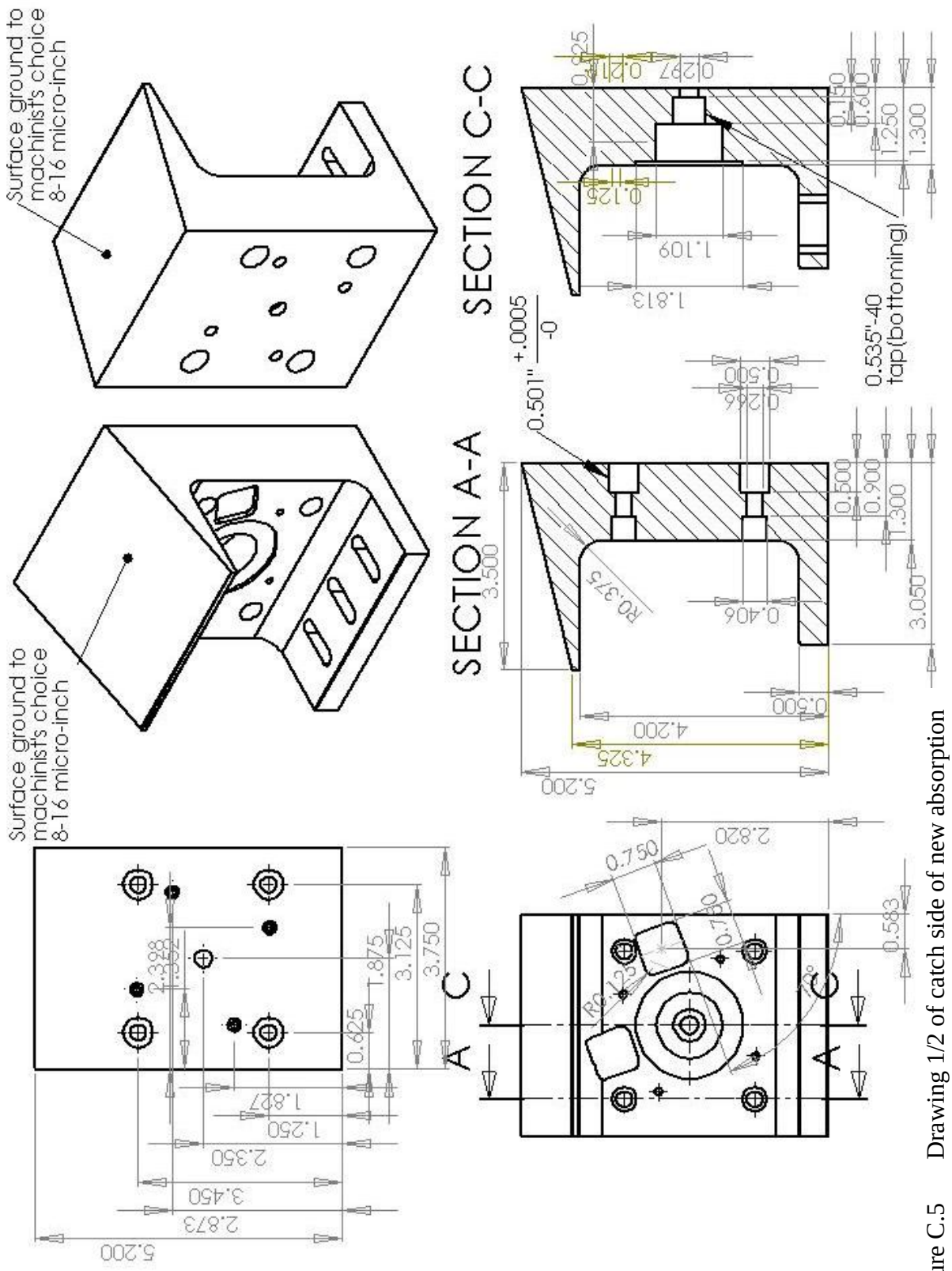

Figure C.5 Drawing 1/2 of catch side of new absorption gauge for use with Newport FPR1-C1A-XYZ multi-axis lens positioner

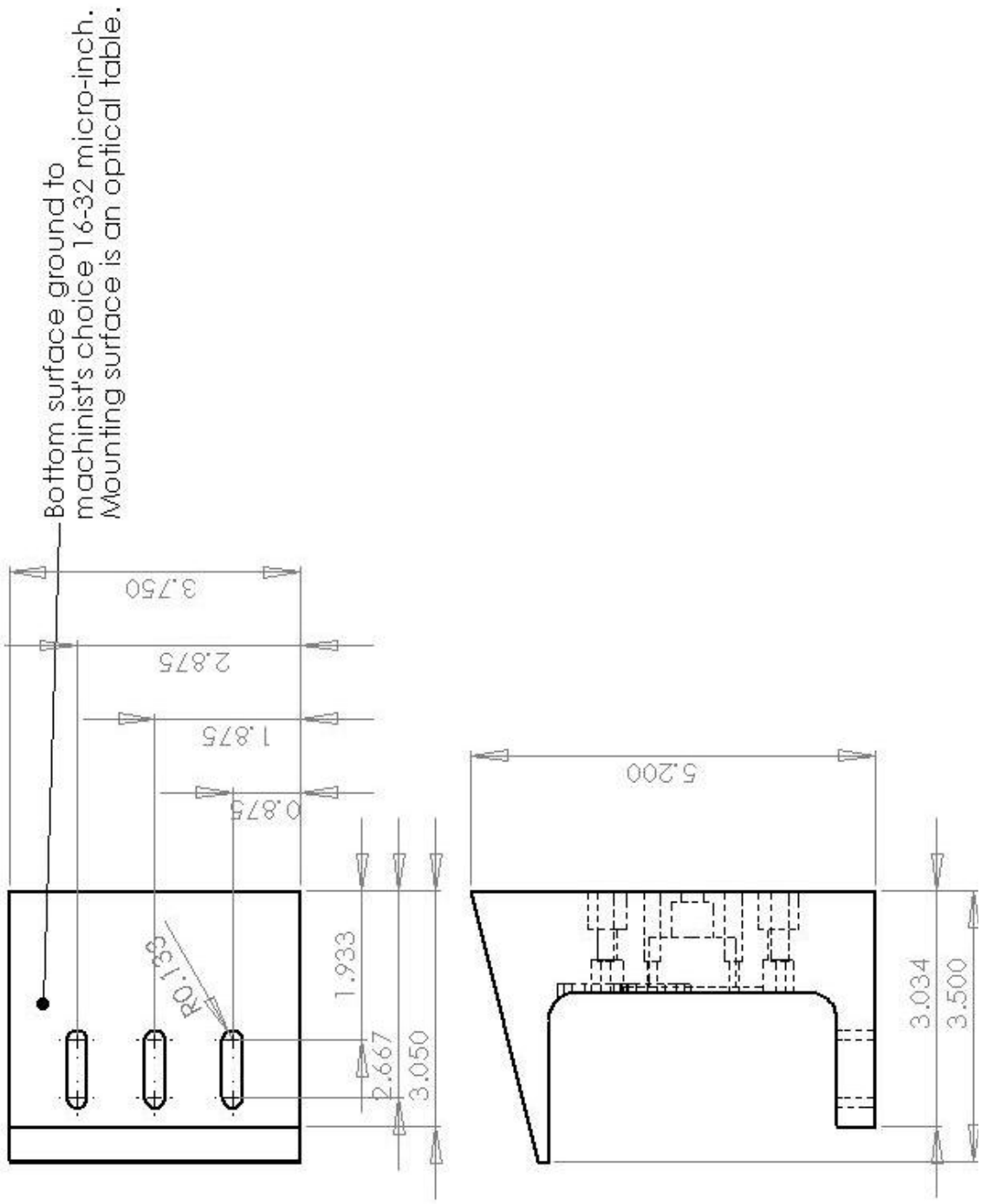

Figure C.6 Drawing 2/2 of catch side of new absorption gauge for use with Newport FPR1-C1A-XYZ multi-axis lens positioner

Arroyo, M. P. and R. K. Hanson (1993). "Absorption measurements of water-vapor concentration, temperature, and line-shape parameters using a tunable InGaAsP diode laser." Appl. Opt. **32**(30): 6104.

Arroyo, M. P., S. Langlois, et al. (1994). "Diode-laser absorption technique for simultaneous measurements of multiple gasdynamic parameters in high-speed flows containing water vapor." Applied Optics **33(15)**: 3296-3307.

Barber, R. J., J. Tennyson, et al. (2006). "A high-accuracy computed water line list." Monthly Notices of the Royal Astronomical Society **368**(3): 1087-94.

Bazyn, T., N. Glumac, et al. (2007). "Reflected shock ignition and combustion of aluminum and nanocomposite thermite powders." Combustion Science and Technology **179**: 457-476.

Bazyn, T., H. Krier, et al. (2006). "Combustion of nanoaluminum at elevated pressure and temperature behind reflected shock waves." Combustion and Flame **145(4)**: 703-713.

Carney, J. R., J. S. Miller, et al. (2006). "Time-resolved optical measurements of the post-detonation combustion of aluminized explosives." Review of Scientific Instruments **77**(6): 063103.

Carney, J. R., J. S. Miller, et al. (2006). "Time-resolved optical measurements of the post-detonation combustion of aluminized explosives." Rev. Sci. Instr. **77**(6): 063103.

Carney, J. R., J. Wilkinson, et al. (2007). "Time-resolved optical measurements of detonation and combustion products." AIP Conference Proceedings **955**(1): 1225-8.

Cezairliyan, A. and F. Righini (1996). "Issues in high-speed pyrometry." Metrologia **33(4)**: 299-306.

Cooper, P. W. (1996). "Explosives Engineering."

Gibson, F. C., M. L. Bowser, et al. (1958). "Use of an Electro-Optical Method to Determine Detonation Temperatures in High Explosives." Journal of Applied Physics **29**(4): 628.

Glumac, N., H. Krier, et al. (2005). "Temperature measurements of aluminum particles burning in carbon dioxide." Combustion Science and Technology **177(3)**(485-511).

Goroshin, S., D. L. Frost, et al. (2006). "Optical Pyrometry of Fireballs of Metalized Explosives." Propellants, Explosives, Pyrotechnics **31**(3): 169-181.

Gross, K. C., A. M. Dills, et al. (2003). "Phenomenology of Exploding Ordnance Using Spectrally and Temporally Resolved Infrared Emissions." Proceedings of SPIE - The International Society for Optical Engineering **5075**: 217-227.

Gross, K. C., G. P. Perran, et al. (2005). "Modeling infrared spectral intensity data from bomb detonations." Proceedings of SPIE - The International Society for Optical Engineering. Targets and Backgrounds XI: Characterization and Representation. **5811**(100-111).

Gross, K. C., J. Wayman, et al. (2007). "Phenomenological fireball model for remote identification of high-explosives." Proceedings of SPIE - The International Society for Optical Engineering. Automatic Target Recognition XVII **65662007**: 656613.

Hagen, C. L. and S. T. Sanders (2007). "Investigation of multi-species (H2O2 and H2O) sensing and thermometry in an HCCI engine by wavelength-agile absorption spectroscopy." Measurement Science & Technology **18**(7): 1992-8.

Hanson, R. K. (2006). Introduction to Spectroscopy and Laser Diagnostics for Gases, Stanford University.

Horn, P. D. and Y. M. Gupta (1986). "Wavelength shift of the ruby luminescence R lines under shock compression." Applied Physics Letters **49**(14): 856-858.

Kranendonk, L. A., X. An, et al. (2007). "High speed engine gas thermometry by Fourier-domain mode-locked laser absorption spectroscopy." Optics Express **15**(23 Nov 12): 15115-15128.

Kranendonk, L. A., A. W. Caswell, et al. (2009). "Temperature measurements in a gas-turbine-combustor sector rig using swept-wavelength absorption spectroscopy." Journal of Propulsion and Power **25(4)**: 859-863.

Kranendonk, L. A., A. W. Caswell, et al. (2007). "Robust method for calculating temperature, pressure, and absorber mole fraction from broadband spectra." Applied Optics **46**(19): 4117-24.

Kranendonk, L. A., R. Huber, et al. (2007). "Wavelength-agile H2O absorption spectrometer for thermometry of general combustion gases." Proceedings of the Combustion Institute Proceedings of the Combustion Institute - Thirty-First International Symposium on Combustion **31 I**: 783-790.

Levi, M. (2004). Study on the Effects of Nuclear Earth-Penetrator Weapon and Other Weapons. T. N. A. o. Sciences, The Brookings Institution.

Lewis, W. K. and C. G. Rumchik (2009). "Measurement of apparent temperature in post-detonation fireballs using atomic emission spectroscopy." Journal of Applied Physics **105**(5): 056104.

Lightstone, J. M., J. R. Carney, et al. (2007). "Time-resolved spectroscopic measurements of aluminum oxidation in a laser ablation event." AIP Conference Proceedings **955**(1): 1255-8.

Magunov, A. (2009). "Spectral pyrometry (Review)." Instruments and Experimental Techniques **52**(4): 451.

McCauley, T. S., A. Israel, et al. (1997). "Spatially resolved in situ diagnostics for plasma-enhanced chemical vapor deposition film growth." Review of Scientific Instruments **68**(4): 1860.

Miller, J. S. and G. I. Pangilinan (2004). Measurements of Aluminum Combustion in Energetic Formulations, AIP.

Morones, J. R., J. L. Elechiguerra, et al. (2005). "The bactericidal effect of silver nanoparticles." Nanotechnology(10): 2346.

Muller, B. and U. Renz (2001). "Development of a fast fiber-optic two-color pyrometer for the temperature measurement of surfaces with varying emissivities." Review of Scientific Instruments **72**(8): 3366-3374.

Ogura, T., K. Okada, et al. (2003). "Pyrometry study on fireballs generated upon the explosion of TNT." Energetic Materials: Reactions of Propellants, Explosives, and Pyrotechnics, 34th Int. Annual Conference of ICT(18).

Orson, J. A., W. F. Bagby, et al. (2003). "Infrared signatures from bomb detonations." Infrared Physics & Technology **44**(2): 101.

Ouyang, X. and P. L. Varghese (1990). "Selection of spectral lines for combustion diagnostics." Appl. Opt. **29**(33): 4884.

Pangilinan, G. I. and Y. M. Gupta (1997). "Use of time-resolved Raman scattering to determine temperatures in shocked carbon tetrachloride." Journal of Applied Physics **81**(10): 6662-6669.

Partouche-Sebban, D., D. B. Holtkamp, et al. (2005). "Alternative calibration techniques for high-speed pyrometers in shock experiments." Review of Scientific Instruments **76**(1): 013106.

Petersen, E., J. Arvanetes, et al. (2007). "Monitoring Strand Burner Combustion Products Using Emission Spectroscopy." 43rd AIAA/ASME/SAE/ASEE Joint Propulsion Conference **8**: 7461-7471.

Petersen, E., J. Arvanetes, et al. (2007). "Monitoring strand burner combustion products using emission spectroscopy." Collection of Technical Papers - 43rd AIAA/ASME/SAE/ASEE Joint Propulsion Conference **8**: 7461-7471.

Peuker, J., P. Lynch, et al. (2009). "Optical depth measurements of fireballs from aluminized high explosives." Optics and Lasers in Engineering **47**: 1009-1015.

Rentz, E. (2003). "Viral Pathogens and Severe Acute Respiratory Syndrome: Oligodynamic Ag⁺ for Direct Immune Intervention." Journal of Nutritional & Environmental Medicine **13**(2): 109 - 118.

Russell, A. D. (1990). "Bacterial spores and chemical sporicidal agents." Clin. Microbiol. Rev. **3**(2): 99-119.

Sambhy, V., M. M. MacBride, et al. (2006). "Silver Bromide Nanoparticle/Polymer Composites: Dual Action Tunable Antimicrobial Materials." Journal of the American Chemical Society **128**(30): 9798.

Sanders, S. T., D. W. Mattison, et al. (2002). "Sensors for high-pressure, harsh combustion environments using wavelength-agile diode lasers." Proceedings of the Combustion Institute **29(2)**: 2661-2666.

Schmidt, J. R., A. W. Caswell, et al. (2006). "Optical system for tomographic measurements in rocket plumes." Collection of Technical Papers - 44th AIAA Aerospace Sciences Meeting. **7**: 5057-5061.

Shafer, A. B., L. R. Megill, et al. (1964). "Optimization of the Czerny-Turner Spectrometer." J. Opt. Soc. Am. **54**(7): 879.

Vidler, M. and J. Tennyson (2000). "Accurate partition function and thermodynamic data for water." Journal of Chemical Physics **113(21)**: 9766-9771.

Wells, R. (1999). "Rapid Approximation to the Voigt/Faddeeva Function and its Derivatives." Journal of Quantitative Spectroscopy and Radiative Transfer **62**(1): 29-48.

Wilkinson, J., J. M. Lightstone, et al. (2007). "Emission spectroscopy of aluminum in post-detonation combustion." AIP Conference Proceedings **955**(1): 1271-4.

Yiannis, A. L., E. Kelvin Rafael, et al. (1992). "Development of multicolor pyrometers to monitor the transient response of burning carbonaceous particles." Review of Scientific Instruments **63**(7): 3608-3622.